NASA TECHNICAL NOTE

NASA TN D-3964

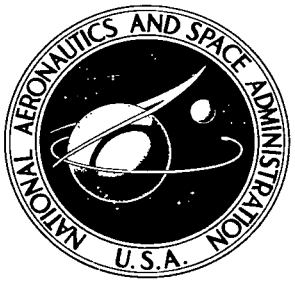

AERODYNAMIC STABILITY CHARACTERISTICS OF THE APOLLO LAUNCH ESCAPE VEHICLE

by William C. Moseley, Jr., and James G. Hondros

Manned Spacecraft Center
Houston, Texas

NATIONAL AERONAUTICS AND SPACE ADMINISTRATION • WASHINGTON, D. C. • JUNE 1967

AERODYNAMIC STABILITY CHARACTERISTICS OF THE APOLLO LAUNCH ESCAPE VEHICLE

By William C. Moseley, Jr., and James G. Hondros

Manned Spacecraft Center
Houston, Texas

NATIONAL AERONAUTICS AND SPACE ADMINISTRATION

For sale by the Clearinghouse for Federal Scientific and Technical Information
Springfield, Virginia 22151 – CFSTI price $3.00

ABSTRACT

A program of wind-tunnel tests was conducted to determine the static and dynamic stability of the Apollo launch escape vehicle. Static stability studies included the effects of escape rocket firing. Results of static tests showed that the vehicle was stable in the normal angle-of-attack operating range and that rocket thrusting generally decreased the longitudinal stability at all Mach numbers tested. Dynamic test data indicated that the vehicle had positive damping over the normal angle-of-attack operating range except for a very small angle range ($\pm 2°$) near the trim angle of attack at subsonic speeds.

CONTENTS

TABLES

FIGURES

AERODYNAMIC STABILITY CHARACTERISTICS OF THE APOLLO LAUNCH ESCAPE VEHICLE

By William C. Moseley, Jr., and James G. Hondros
Manned Spacecraft Center

SUMMARY

Wind-tunnel tests were made at several facilities to determine the static and the dynamic stability characteristics of the Apollo launch escape vehicle at Mach numbers from 0.25 to 6.0. Static stability tests included the effects of launch escape rocket thrusting. Dynamic stability derivatives were determined using both forced- and free-oscillation test techniques.

Results of the tests indicate the Apollo launch escape vehicle is statically stable, both power on and power off, over the normal angle-of-attack operating range near the trim angle of attack. The effect of rocket thrusting is to reduce the stability, particularly at the highest values of thrust coefficient investigated. Also, the Apollo launch escape vehicle generally has positive damping over the normal angle-of-attack operating range except for a very small angle range ($\pm 2°$) near the trim angle of attack at subsonic speeds.

INTRODUCTION

The Apollo Spacecraft Program, with the eventual goal of a manned lunar landing, was initiated by the National Aeronautics and Space Administration (NASA) as part of the continuing program of space exploration following Project Mercury and the Gemini Program. Initial study contracts, NASA Space Task Group studies, and other non-funded studies established the design requirements for the Apollo configuration, using the separable module concept. Some of the initial wind-tunnel studies used subsequently to support and verify this selection can be found in references 1 to 4.

As part of the design and development program initiated in support of the Apollo Spacecraft Program, the Apollo wind-tunnel program was established. (See table I for a list of test facilities and capabilities.) The total program, discussed in more detail in reference 5, was planned to yield design data on static and dynamic stability, aerodynamic heating, and aerodynamic loads; and the program was planned to evaluate thoroughly such specific problems as interactions between separating bodies during normal or abort operations, jet-plume interactions or effects, and launch vehicle compatibility. The stability characteristics of the Apollo command module (CM) are presented in reference 6. The program had to provide the experimental data necessary for efficient

spacecraft design, as well as data for studies of all phases of the flight programs. One primary area of concern was the prelaunch or atmospheric portion of the flight where any failure would likely result in a launch vehicle explosion. In the event of any malfunction requiring a premature termination of the flight, the Apollo launch escape vehicle (LEV) was designed to remove the CM and its occupants a safe distance from the launch vehicle. The LEV comprises the CM plus the launch escape system, which consists primarily of the escape tower, the escape rocket, the jettison rocket, the pitch control motor, and the canard surfaces. As stated previously, the system is designed for use during the prelaunch and/or atmospheric portion of the flight and is jettisoned when no longer needed, since other propulsion systems provide a means of escape in the latter stages of flight. In order to design and fully evaluate the LEV, investigations were made to determine the aerodynamic characteristics of the vehicle.

The purpose of this paper is to present the aerodynamic characteristics of the Apollo LEV as determined by wind-tunnel tests. Thrusting static stability data have been determined at Mach numbers from 0.5 to 6.0 over an angle-of-attack range from -5° to 60°. Nonthrusting static stability data were obtained over the same angle-of-attack range at Mach numbers from 0.25 to 6.0. Dynamic stability studies were made at Mach numbers from 0.5 to 6.0, using forced-oscillation, limited free-oscillation, and free-to-tumble test techniques to determine the damping-in-pitch derivative.

SYMBOLS

The force and moment coefficients presented in this paper are referenced about the body system of axes as shown in figure 1.

A_e nozzle exit area

A_t nozzle throat area

C_A axial-force coefficient, $\frac{\text{axial force}}{q_\infty S}$

$C_{A,\alpha=0^\circ}$ axial-force coefficient at $\alpha = 0^\circ$

$C_{m,a}$ pitching-moment coefficient computed about theoretical apex, $\frac{\text{pitching moment}}{q_\infty S d}$

$C_{m,c.g.}$ pitching-moment coefficient computed about a nominal center of gravity, $(x/d = -0.104, \quad z/d = 0)$

C_{m_α} slope of the pitching-moment coefficient measured at $\alpha = 0^\circ$

$C_{m_q} + C_{m_{\dot{\alpha}}}$	damping-in-pitch parameter, $\frac{\partial C_m}{\partial\left(\frac{qd}{2V}\right)} + \frac{\partial C_m}{\partial\left(\frac{\dot{\alpha}d}{2V}\right)}$
$\overline{C_{m_q}} + \overline{C_{m_{\dot{\alpha}}}}$	average damping-in-pitch coefficient over one full oscillation
C_N	normal-force coefficient, $\frac{\text{normal force}}{q_\infty S}$
C_{N_α}	slope of the normal-force coefficient measured at $\alpha = 0°$
C_T	thrust coefficient referred to longitudinal axis, $\frac{\text{thrust}}{q_\infty S} \times \cos 35°$
d	maximum body diameter, (154 in. full scale)
I	moment of inertia
k	reduced frequency parameter, $\frac{\omega d}{2V}$
M	free-stream Mach number
$\mathring{M}$	mass flow rate, $\frac{\text{thrust}}{V_j}$
P	pressure
q	pitching velocity
q_∞	free-stream dynamic pressure
R	Reynolds number based on maximum model diameter
S	maximum cross-sectional area perpendicular to X body axis
V	free-stream velocity
X, Y, Z	body reference axes
$\frac{x}{d}$	longitudinal location of center of gravity measured from theoretical apex
$\frac{z}{d}$	vertical location of center of gravity measured from centerline
α	angle of attack of model centerline

$\dot{\alpha}$	time rate of change of angle of attack
α_{trim}	trim angle of attack
γ	ratio of specific heats
ρ	mass density of air
ω	frequency of oscillation

Subscripts:

c	chamber
fs	full scale
j	jet
m	model
T	total coefficients, includes aerodynamic and thrusting forces
∞	free-stream conditions

The aerodynamic coefficients presented for the thrusting tests, unless otherwise noted, include the interference or aerodynamic effects of the rocket exhaust, but with the thrusting components removed.

MODELS AND TEST TECHNIQUES

Test models varying in size from 0.045- to 0.105-scale were used in conducting these tests. The geometric similarity of the model to the full-scale vehicle was maintained except for the thrusting models. In the cold-jet thrusting model, a high-pressure air line was routed through the center of the tower to the escape motor and the hot-jet model had tower legs which were slightly larger than scale in order to accommodate the propellant lines. A sketch of the Apollo LEV is presented in figure 2, and photographs of test models mounted in test facilities and model components are included in figure 3.

The basic models of the CM did not simulate the protuberances and cavities such as antennas, umbilical fairing, air vent, windows, and tower leg wells which were included on the models used in later tests. Tests of the CM with these surface modifications are reported in more detail in reference 6.

Selective model-mounting techniques made testing possible through the complete angle-of-attack range from 0° to 360°. Available balances were not readily adaptable to the large angle ranges tested and in many cases were not ideally suited for spacecraft

testing; consequently, they were selected for gross overall loading. Models were designed for use in more than one facility to allow for the efficient and economical testing over the full range of Mach numbers and Reynolds numbers. A list of the models used and ranges over which they were tested is included (table II).

Static Stability Tests

Power off. - Early tests were made with 0.045- and 0.105-scale models of the Apollo LEV to define the power-off static stability characteristics. Data are included which were used to extend the available data to M = 6.0 for a configuration that is slightly different from the basic flight configuration. The alternate configuration is identical to the basic flight configuration except for the tubular bracing in the most forward section of the escape tower.

Power on, hot jet. - Tests, using a hydrogen peroxide gas generator and high-pressure cold air, were made to obtain the effects of rocket thrusting on the stability characteristics of the LEV. A detailed description of the H_2O_2 system is given in reference 7; therefore, only certain pertinent details will be discussed here. For simulating thrust (hot jet), liquid H_2O_2 was brought through the sting-support system into the model by two stainless steel propellant lines. Within the CM, the lines were formed into concentric right- and left-hand helices around the strain-gage force balance. From the helical coils, the H_2O_2 was fed into a torus-shaped plenum chamber, and then through the four tower legs into the gas generator within the escape motor casing (fig. 4). The escape motor contained a radial flow decomposition chamber, which utilized a catalyst pack as shown in figures 3 and 5. Silver screen, coated with samarium oxide, was cut into discs that were compressed around a perforated distribution pipe between thin spacer discs. The pack was enclosed in a 30-percent open perforated stainless-steel cylinder. This motor was designed to decompose 90-percent hydrogen peroxide at a maximum rate of 15 lb/sec.

Products of decomposition (super-heated steam and free oxygen) flowed along the pack to the rear of the motor and out the four nozzles shown in detail in figure 5. The nozzles had divergence half-angles of 17.5°. The two nozzles in the yaw plane and the upper nozzle in the pitch plane had equal throat areas and equal exit-area ratios of 10; the lower nozzle in the pitch plane had a larger throat area and a smaller exit-area ratio of 7.62. The asymmetric thrust of the nozzles in the pitch plane provided an offset thrust vector (2° 45').

A brief résumé of the data cycle is presented for clarity. When the escape rocket jets were not being simulated, the model balance system recorded the aerodynamic characteristics of the Apollo LEV. With the rockets thrusting, the balance system recorded the rocket thrust forces and moments as well as the aerodynamic forces and moments for the vehicle. These data are designated as total force and moment coefficients. Static rocket thrust calibrations were made with a shroud around the model to provide the thrust components. By removing the applicable components of the jet thrust, the aerodynamic coefficients are obtained. These coefficients represent the aerodynamic characteristics of the Apollo LEV in the presence of the free stream as altered by the rocket exhaust plumes.

Power on, cold jet. - Unheated compressed air was also used to simulate jet thrusting (cold jet). The air system of the model, as shown in figure 6, extended from the sting, through the CM, to the escape motor. Since this air system was physically isolated from the balance, the CM, and the tower, the aerodynamic coefficients measured represent those characteristics of the Apollo LEV in the presence of the free stream altered by the rocket exhaust. The air, from a 4000-psi supply, was brought to the model support structure and then ducted through two pipes, located on either side of the balance, to a manifold in the CM. A single pipe, concentric with the model centerline, extended from the manifold, through the tower, to the nozzle adapter which contained the simulated LEV. In order to achieve an acceptable simulation, these nozzles were not constructed to scale except for the exit area, the exit location, and their centerline inclination to the model centerline. This simulation will be discussed later.

Dynamic Stability Tests

Provision was made, in the wind-tunnel program, for extensive evaluation of the dynamic stability characteristics of the Apollo LEV. Dynamic stability data were acquired through the use of the following test techniques:

(1) Forced oscillation

(2) Limited free oscillation

(3) Free to tumble

A detailed discussion of the techniques and apparatus used for measuring dynamic stability parameters for a rigidly-forced oscillation system is found in reference 8, and a method for reducing these aerodynamic characteristics to coefficient form is described in reference 9. Limited free-oscillation test techniques, apparatus, and data reduction methods are discussed in reference 10.

The free-to-tumble technique is a method which allows statically balanced models, mounted on a transverse rod through the center of gravity, to tumble freely through an angle-of-attack range of 360°. A photograph of a typical model installation for this technique is shown in figure 3. Some problems were encountered in designing a method of mounting the model on a system where minimal friction and interference were required. A gas-bearing support, similar to one used successfully in limited free-oscillation tests, failed because of galling under high-loading conditions. A method of mounting, using precision ball bearings, was developed and proved satisfactory. It was determined that friction or tare damping generally contributed a fractional part (less than $C_{m_q} + C_{m_{\dot{\alpha}}} = \pm 0.5$) of the aerodynamic damping of the system. Bench tests were made to determine the friction damping under load, and tare corrections were applied to the data.

FACILITIES

The broad range of expected flight conditions (Mach number, Reynolds number, and angle of attack), and the limitations of any single wind tunnel to simulate all these conditions, dictated the utilization of a number of test facilities. The wind-tunnel-test facilities used to acquire static and dynamic stability data on the Apollo LEV, along with tunnel size and capability, are listed in table I.

TEST CONDITIONS AND ACCURACIES

Test Conditions

Table III lists the test conditions by facility. Complete data were not available, which accounts for the absence of information in portions of this table.

Accuracies

Standard statistical analysis of balance calibration data and data repeatability indicated certain accuracy tolerances of the static force and moment coefficients. This information, where available, has been compiled in table IV.

For the forced-oscillation dynamic testing, structural damping values were obtained at vacuum conditions, before tunnel tests were made, to evaluate the still-air damping contribution. Using known displacements and moments, transducer calibration factors were obtained for the model displacement and input torque. Resulting errors in either parameter were within ± 0.75 and ± 1.0 percent of the maximum values of the range in which each parameter was calibrated. Considering the uncertainties in the system and the fact that the aerodynamic damping-in-pitch parameter is a function of the difference between wind-on and vacuum conditions, the estimated maximum uncertainties in $C_{m_q} + C_{m_{\dot{\alpha}}}$ were ± 0.50 for the Apollo LEV.

In the limited free-oscillation technique of dynamic testing, two sources of error were of primary importance in evaluating the accuracy of the data: the measurements from the angular displacement transducer and the determination of the tare damping of the ball-bearing support system. The estimated maximum uncertainties in $C_{m_q} + C_{m_{\dot{\alpha}}}$ were ± 0.50 for the Apollo LEV.

Dynamic stability data obtained in the free-to-tumble technique cannot be said to have a certain accuracy at a particular angle of attack. The accuracy of these data is determined by the quality of the match between computer simulation and measured wind-tunnel position-time histories. An indication of the matching is shown in figure 7. The measured and computed time-motion histories indicate an excellent match except for a slight variation in the frequency of oscillation. This frequency difference, however, is negligible when converted to full-scale values.

SIMULATION

Static Stability Tests

Close simulation of actual flight conditions is necessary to achieve usable data from wind-tunnel tests. Numerous factors must be considered including (1) model geometry, (2) Reynolds number, and (3) Mach number. If model geometry is similar to the prototype, if Reynolds number of model and prototype are matched, and if Mach number of the tunnel airflow equals flight Mach number, good simulation is assumed.

Thrusting jets exhausting near the CM surface affect vehicle flight characteristics in two ways: (1) blockage of the free-stream flow by the jet plumes and (2) impingement of the jet on the surface of the CM. The first affects the aerodynamic characteristics and stability of the vehicle by altering the free-stream flow around the CM. The second increases surface pressures and temperatures which in turn affect the stability of the vehicle. Close simulation of jet thrusting requires a similarity of parameters which affect the jet penetrating into the free-stream flow and the jet mixing with the free stream. Some of the factors which must be considered include Reynolds number, Mach number, velocity, temperature, density ratio, mass flow, ratio of specific heats, and scaled jet thrust.

Hot-jet simulation. - The hot-jet model had scaled rocket nozzle throat areas A_t and exit areas A_e and the same expansion ratio A_e/A_t as the full-scale rocket nozzles. The equation for the thrust coefficient is

$$C_T = \left(\frac{\text{thrust}}{q_\infty S}\right)_{fs} = \left(\frac{\text{thrust}}{q_\infty S}\right)_m \tag{1}$$

where q_∞ in $\left(\frac{\text{thrust}}{q_\infty S}\right)_{fs}$ refers to Saturn I, 100-nautical-mile-orbit boost trajectory, and q_∞ in $\left(\frac{\text{thrust}}{q_\infty S}\right)_m$ refers to tunnel conditions. Since both the external and internal geometric similarity were maintained and the ratio of specific heats γ for the H_2O_2 exhaust gas (where $\gamma = 1.265$) was close to that of solid propellant rocket exhaust (where $\gamma = 1.23$), the data presented in terms of thrust coefficient should give good approximations of the jet effects on the stability of the Apollo LEV. The thrust simulation parameter for the matched stream conditions and jet-pressure ratios gave values for $\gamma_j M_j^2$ of 15.3 and 14.0 for the model and full-scale values, respectively. Further details of the hot-jet technique using H_2O_2 gas generators can be found in references 7, 11, and 12. For the present study, wherein the downstream portion of exhausting jets can influence the aerodynamic characteristics of the vehicle, the simulation parameters affecting the jet penetration into the free-stream flow and the jet mixing with the free-stream flow must be considered (refs. 13 and 14). The duplication of the jet

boundary shape is, therefore, desirable. If the model has the same nozzle divergence angle as the full-scale vehicle, the exit static pressure, along with γ_j and M_j, determines the initial plume shape similarity. The jet shaping downstream of the nozzle is also important if the jet effects are to be properly defined. Matching of the mixing boundary shape may be possible with the simulation of gas-constant total-temperature values for the full-scale rocket (ref. 8). Although the decomposition products of H_2O_2 have gas-constant total-temperature values of less than 40 percent of the high-temperature full-scale vehicle, the downstream simulation is still considered acceptable. Compromises in nozzle geometry are necessary to obtain the required simulation of both the initial and the downstream shapes using air. The simulation is discussed below.

Cold-jet simulation. - The cold-jet model used unheated high-pressure air as the fluid for simulation of the launch escape rocket exhaust products. Since the two fluids (gases) are considerably different in physical characteristics, a brief discussion of the analyses which supports the simulation technique is presented. As stated previously, the simulation parameters which were determined to be the most important are jet momentum and jet plume shape. Initially, let us assume that the nozzle efficiencies of the full-scale vehicle and the model are equal. The ideal momentum ratio is defined as the ideal thrust coefficient C_T where

$$C_T = \left(\frac{\mathring{M}_j V_j}{q_\infty S}\right)_{fs} = \left(\frac{\mathring{M}_j V_j}{q_\infty S}\right)_m \tag{2}$$

where $\mathring{M}$ is the mass flow rate. This can be expanded to

$$2\left(\frac{\gamma_j M_j^2 P_j A_j}{\gamma_\infty M_\infty^2 P_\infty S}\right)_{fs} = 2\left(\frac{\gamma_j M_j^2 P_j A_j}{\gamma_\infty M_\infty^2 P_\infty S}\right)_m \tag{3}$$

Since $M_{\infty,m}$ and $\gamma_{\infty,m}$ are set equal to $M_{\infty,fs}$ and $\gamma_{\infty,fs}$ in the tunnel and P equals P_j for an isentropically expanded jet, this equation reduces to

$$\left(\frac{\gamma_j M_j^2 A_j}{S}\right)_{fs} = \left(\frac{\gamma_j M_j^2 A_j}{S}\right)_m \tag{4}$$

and since

$$M_{j, fs} = f\left(\frac{P_{c, fs}}{P_{\infty, fs}} \text{ and } \gamma_{j, fs}\right) \tag{5}$$

$$A_{j, fs} = f\left(\frac{P_{c, fs}}{P_{\infty, fs}}, \gamma_{j, fs}, \text{ and } A_{t, fs}\right) \tag{6}$$

$$M_{j, m} = f\left(\frac{P_{c, m}}{P_{\infty, m}} \text{ and } \gamma_{j, m}\right) \tag{7}$$

and

$$A_{j, m} = f\left(\frac{P_{c, m}}{P_{\infty, m}}, \gamma_{j, m}, \text{ and } A_{t, m}\right) \tag{8}$$

$$\frac{P_{c, m}}{P_{\infty, m}} = f\left(\frac{P_{c, fs}}{P_{\infty, fs}}, \gamma_{j, fs} A_{t, fs} \gamma_{j, m} A_{t, m}, \text{ and the scale factor}\right) \tag{9}$$

for jet momentum simulation. The value of $A_{t, m}$ was selected to maintain $\frac{P_{c, m}}{P_{\infty, m}}$ within the capabilities of the test facility. The primary parameter considered for plume shape simulation was the flow direction of the boundary streamline as it leaves the nozzle exit. Comparisons of computed plume shapes, both full scale and model, made by means of a modified method of characteristics computer program, indicate that the matching is acceptable. Because of the space restriction in the model rocket base area, it was not possible to design a plenum chamber upstream of the model rocket nozzles to stagnate the air. Since it was necessary to turn the airflow approximately 145° at high velocities with accompanying high pressure losses, it was impossible to measure nozzle stagnation pressures with a conventional wall tap. An airflow rate calibration of a chamber pressure tap on the model centerline was made to provide a means for setting the thrust level.

Dynamic Stability Tests

Close simulation of actual flight conditions is of paramount importance in dynamic stability tests. The scope of this problem is appreciated when the reduced

frequency parameter is considered. This parameter represents a ratio of the characteristic length of the body to the wavelength of a disturbance. Since every point of a body disturbs the flow, the reduced frequency characterizes the mutual influence between the motion at various points on the body. Therefore, matching the reduced frequency parameter insures the similarity of the two systems when investigating unsteady aerodynamics. Dynamic similarity between the full-scale vehicle and the test was correlated by using the reduced frequency parameter k.

$$k = \left(\frac{\omega d}{2V}\right)_m = \left(\frac{\omega d}{2V}\right)_{fs} \tag{10}$$

where ω is the frequency of oscillation, d is the reference length, and V is the velocity.

$$\left(\frac{\omega d}{2V}\right)_m = \left(\frac{\omega d}{2V}\right)_{fs} \tag{11}$$

where

$$\omega = \left(C_{m_\alpha} \frac{q_\infty Sd}{I}\right)^{1/2} \tag{12}$$

and

$$\left[\frac{d}{V}\left(C_{m_\alpha} \frac{q_\infty Sd}{I}\right)^{1/2}\right]_m = \left[\frac{d}{V}\left(C_{m_\alpha} \frac{q_\infty Sd}{I}\right)^{1/2}\right]_{fs} \tag{13}$$

If static operating temperatures are equal, or $T_m = T_{fs}$, then $V_m = V_{fs}$ and the above identity becomes

$$\left(\frac{q_\infty d^5}{I}\right)_m = \left(\frac{q_\infty d^5}{I}\right)_{fs} \tag{14}$$

However, if the velocities are not equal, the identity becomes

$$\left(\frac{\rho_\infty d^5}{I}\right)_m = \left(\frac{\rho_\infty d^5}{I}\right)_{fs} \tag{15}$$

Therefore, the reduced frequency parameter may be managed by varying the dynamic pressure or changing the moment of inertia by ballasting. The approach used depended on the conditions, which were determined by the wind-tunnel test used.

DISCUSSION

Presentation of Results

The results of this report are summarized in the following figures.

(1) Figures 8 and 9 present the static longitudinal stability characteristics of the Apollo LEV.

(2) Figures 10 to 14 present the longitudinal stability characteristics of the LEV in the presence of thrusting.

(a) Figure 10 presents the data from hot-jet simulation tests.

(b) Figure 11 presents the data from hot-jet simulation tests against the angle of attack at Mach numbers 0.5, 0.9, 1.1, and 1.3.

(c) Figure 12 presents the total aerodynamic characteristics of the Apollo LEV at Mach number 0.9 plotted against the angle of attack.

(d) Figures 13 and 14 present the results of the cold-jet method of simulation. Figure 13 presents the aerodynamic coefficient data plotted against the thrust coefficient, and figure 14 presents the aerodynamic coefficient data plotted against the angle of attack at Mach numbers 1.98, 2.99, 3.99, and 5.97.

(3) Figure 15 presents a comparison of data obtained by the hot- and cold-jet methods of simulation at Mach number 0.7.

(4) Figure 16 presents the dynamic stability characteristics determined by a forced-oscillation technique.

(5) Figure 17 presents the dynamic stability characteristics, as determined by the limited free-oscillation technique at three centers of gravity.

(6) Figure 18 presents the dynamic stability characteristics, as determined by the free-to-tumble technique, from Mach numbers 0.5 to 1.98.

(7) Figure 19 presents a comparison of pitching-moment characteristics obtained with sting-mounted and transverse-rod-mounted models.

(8) Figure 20 presents summary data.

Static Stability Characteristics

Static stability characteristics of the Apollo LEV (nonthrusting) have been determined at Mach numbers from 0.25 to 1.35 at the Ames Unitary Plan and 12-Foot Wind Tunnels. Additional data are presented to extend the data to Mach number 6.0; however, the configuration tested had a slightly different tower bracing than the final configuration. Static stability data for the Apollo LEV with simulated LEV rocket thrust have been determined at Mach numbers from 0.5 to 1.30 at the Langley 16-Foot Transonic Tunnel using a H_2O_2 gas generator to simulate the rocket thrust. Data for $M = 0.7$ and $M = 1.48$ to 5.97 were determined at the Arnold Engineering Development Corporation Tunnel A using high pressure air to simulate the rocket thrust. The aerodynamic coefficients, unless otherwise noted, include the aerodynamic or interference effects of the thrusting rocket, but have had the components of the rocket thrust removed or isolated from the balance during testing. Details of the test procedures for the thrusting tests can be found in references 7, 15, and 16.

Static, nonthrusting.- The static stability data (nonthrusting), given in figures 8 and 9 and summarized in figure 20, indicate that the general variation in the pitching-moment coefficient with the angle of attack is only slightly changed with the increase in Mach number up to $M = 1.55$. The pitching-moment curve slope C_{m_α} decreases with Mach number to near $M = 0.90$ and then increases above $M = 0.90$. The favorable increase in the overall stability at Mach numbers above $M = 1.55$ is attributed to a shock interaction that results in an increase in pressure on the lower surface of the CM at moderate angles of attack ($\alpha = 10^\circ$ to 40°). Note the comparison of the pitching-moment curve slopes determined from the nonthrusting and thrusting test installations (fig. 20). There are some differences in the pitching-moment curve slope (power off) as determined from the nonthrusting and thrusting test installations. Note that the pitching-moment coefficient variation with angle of attack is generally nonlinear and any slope parameter presented would be indicative only over a limited angle range near the point of measurement. Data of the pitching-moment coefficient plotted against the angle of attack at $M = 3.0$ (figs. 9(d) and 14(d)) indicate there are only small differences in the data as determined by the two test installations. The slope-parameter data (fig. 20) indicate the difference could be much greater. There are also some differences in model installation, the major one being the increased sting diameter necessary to accommodate the rocket exhaust system. The variation of the normal-force coefficient with the angle of attack (figs. 8, 9, and 20) indicates that C_{N_α} decreases slightly with the Mach number up to $M = 0.80$. There are rather abrupt changes in the normal-force curve slope in the transonic region ($M = 0.9$ to 1.2). Except for a decrease in C_{N_α} near $M = 3.0$, the normal-force curve slope is generally constant through the supersonic speed range ($M = 1.2$ to 6.0). The power-off normal-force curve slope from both nonthrusting and thrusting test installations compares favorably

except for some differences indicated at M = 1.0, 3.0, and 6.0. The power-off axial-force coefficient data (figs. 8, 9, and 20) indicate an increase in $C_{A, \alpha=0^\circ}$ up to M = 1.1 with a slight decrease in $C_{A, \alpha=0^\circ}$ with further increase in the Mach number above M = 1.1. The comparison between the power-off and the nonthrusting and thrusting installations should again be noted.

A comparison of the static stability data for the alternate configuration is also presented in figure 9 for Mach numbers 0.7 to 1.35. These data are in very good agreement with those for the basic configuration for the Mach number and the angle-of-attack range tested.

Static, thrusting. - The exhausting of jet streams near adjacent surfaces can appreciably alter flow patterns, surface pressures and temperatures, and the aerodynamic stability. Detailed studies were made to evaluate the effects of rocket exhaust on the static stability characteristics of the Apollo LEV. Again, two different test techniques were used to determine the jet effects. A comparison of the data obtained by using the two techniques is presented in figure 15 for C_T = 0, 1.34, and 2.40. Only small variations in the pitching-moment and normal-force coefficients (both power off and power on) are indicated by the measured data. The axial-force data compare favorably at C_T = 0, but are higher for the cold-jet data with the jets thrusting. The favorable comparison of the summary data for the hot-jet data at M = 1.3 with the summary data for the cold-jet data at M = 1.48 (fig. 20) should be noted, since the cold-jet model was designed for the supersonic Mach number range (M = 1.48 to 5.97).

A typical representation of the total aerodynamic force and moment coefficients measured at M = 0.9, using the hot-jet simulation method, is presented in figure 12. The total pitching-moment coefficient $C_{m, a, T}$ as shown on figure 12(a) generally becomes more positive with increase in thrust coefficient at both the lower and higher angles of attack while it is slightly more negative in the angle-of-attack range between 25° and 40°. This same trend is indicated for other Mach numbers not presented here, but discussed in reference 7. The normal-force coefficient $C_{N, T}$ increases as the thrust coefficient is increased at angle of attack = 0°, but remains generally constant with increase in angle of attack. Jet-off values show positive axial-force coefficient for all angles of attack tested as shown in figure 12(c). With the jet on, the thrust overcomes the aerodynamic axial force and at the higher values of thrust coefficient results in a forward acceleration of the vehicle.

The variation of force and moment coefficients with thrust coefficient for Mach numbers 0.5 to 1.30 is presented in figure 10 and was obtained using the hot-jet technique. Like data, obtained from tests using the high-pressure cold air system, for Mach numbers 0.7 and 1.48 to 5.97 are given in figure 13. The pitching-moment coefficient varies irregularly with thrust coefficient as a result of the rocket-exhaust free-stream flow-field interaction. At the lower Mach numbers (0.7 to 1.98) and angles of attack (0° to 10°), small irregular changes in pitching-moment coefficient occurred with increase in thrust coefficient. At angles of attack above about 20°, moderate increases in thrust coefficient resulted in higher negative values of pitching moment. Further increases in thrust coefficient generally resulted in a trend toward

more positive values of pitching moment. (See figs. 10(a), 10(d), 10(s), 13(d), and 13(g).) At the supersonic Mach numbers between 2.99 and 5.97, the effect of increasing rocket thrust was a general increase in pitching moment toward more positive values at all angles of attack as shown in figures 13(j) and 13(m).

The normal-force coefficient varied irregularly with Mach number and angle of attack as the thrust coefficient was increased. Generally, the overall trends were small and resulted in a decrease in normal-force coefficient with increase in thrust coefficient, although some exceptions are evident at the higher angles of attack. For example, at subsonic Mach numbers as shown in figures 10(b), 10(e), 10(h), and 13(b), C_N generally decreased at the lower angles of attack with an increase in thrust coefficient. At the higher angles of attack, C_N showed a general increase as the thrust coefficient was increased. Increasing the thrust coefficient generally has little effect on C_N in the transonic and low supersonic Mach number range (up to $M = 1.98$) as shown on figures 10(k), 10(n), 10(q), 13(e), and 13(h). At the higher supersonic Mach numbers, $M = 1.99$ and above, increasing the thrust coefficient resulted in a decrease of the normal-force coefficient at most angles of attack as given in figures 13(k) and 13(n).

The effect of rocket thrust on the axial-force coefficients, presented in figures 10 and 13, is irregular. The data of figure 10 indicate that the effect of increasing thrust coefficient is to increase axial-force coefficient at all angles of attack tested at Mach numbers up to 1.3. Except for $M = 0.7$, the data of figure 13 indicate a generally reversing trend until $M = 1.98$ is reached. At $M = 1.98$ and above, increasing the thrust coefficient results in a decrease in axial-force coefficient at some angles of attack. At the highest Mach numbers tested ($M = 4.99$ and 5.97) there was a decrease in axial-force coefficient with rocket thrust at the initial thrust coefficient tested and an increase in axial-force coefficient at the highest thrust coefficient tested. This increase is the result of jet plume impingement. These data are discussed additionally in references 7, 15, and 16.

The effect of thrust coefficient on the aerodynamic characteristics with variations in angle of attack is presented in figures 11 and 14. The pitching-moment coefficient data vary nonlinearly with the angle of attack at $C_T = 0$. This nonlinearity, as noted in reference 17, results from the wake of the tower rocket disturbing the flow over the upper surface of the CM as the angle of attack is increased. In addition, at Mach numbers above 1.98, the bow shock and the CM surface shock interact to produce higher pressures on the lower surface of the CM resulting in an increase in the power-off stability. The angle-of-attack range of stability with jets off is about 40° for $M = 0.50$ and decreases as Mach number is increased, until at $M = 1.3$, the vehicle is stable only to about 11°. At Mach numbers above $M = 1.3$, the vehicle tends to be stable over an increasing angle-of-attack range, until at Mach number 5.97, the vehicle is stable up to an angle of attack of 20°. The effect of rocket exhaust on the pitching-moment coefficient varies with thrust coefficient and Mach number over the angle-of-attack range tested. These data indicate that the basic, or jet-off, aerodynamics have the predominant effect on the stability of the vehicle. At Mach numbers up to $M = 1.98$, the effect of the rocket thrust is small, although it does alter the pitching-moment coefficient variation with angle of attack by changing the degree of stability and the location of the unstable angle-of-attack range. At $M = 2.99$, the effect of rocket thrust is to

significantly reduce the stability of the vehicle. At Mach numbers above M = 2.99, the effects of jet shielding and impingement reduce the stability of the vehicle to near zero.

At Mach numbers up to M = 1.98, the effect of increasing rocket thrust on the variation of the normal force with angle of attack was generally small except for small irregular changes in slope at some Mach numbers. (See figs. 11 and 14(b).) At M = 2.99, the effect of rocket thrust is to reduce the normal-force curve slope resulting primarily from the jet shielding on the CM and flow separation on the rocket induced by jet expansion. This effect becomes increasingly more significant at Mach numbers above M = 2.99 until at M = 5.97 the normal-force curve slope is near zero.

Data, presented in figures 11 and 14 for jet-off conditions, indicate that the axial-force coefficient increases slightly with the angle of attack up to 10°. At angles of attack greater than 10°, the axial-force coefficient decreases with increases in the angle of attack except at the highest supersonic Mach numbers. At Mach numbers from 0.5 to 1.98, the effect of rocket thrust is to increase the axial-force coefficient. At Mach numbers from 1.98 to 4.99, the effect of rocket thrust is to reduce generally the magnitude of the axial-force coefficient as a result of the jet exhaust shielding the CM. At M = 5.97, the rocket exhaust impinges on the CM surface and results in an increase in the axial-force coefficient.

The axial-force coefficient $C_{A,\alpha=0^\circ}$ and the slope parameters C_{m_α} and C_{N_α} are presented in figure 20. These data show the effect of rocket exhaust on these parameters as a function of Mach number.

Dynamic Stability Characteristics

Dynamic stability characteristics, determined by three different test methods, forced oscillation, limited free oscillation, and free to tumble, are presented in figures 16 to 18, respectively. The $C_{m_q} + C_{m_{\dot{\alpha}}}$ data of figure 16 (ref. 18) at Mach numbers 2.0 to 6.0 are for an offset center-of-gravity location. For purposes of comparison, similar data at Mach numbers 2.0 to 6.0 are presented for a centerline center-of-gravity location. These data were determined utilizing the forced-oscillation test technique and indicate that the vehicle generally has positive damping except for M = 6.0 for the offset center-of-gravity location where a highly irregular variation in the damping parameter near the trim angle of attack is indicated. Additional studies using a forced-oscillation technique are reported in references 19 to 23. The data from these studies are not presented here since the configurations tested differed slightly from the production Apollo LEV.

The variation of the average damping-in-pitch parameter $\overline{C_{m_q}} + \overline{C_{m_{\dot{\alpha}}}}$ as determined from tests using the limited free-oscillation test technique is presented in figure 17 for Mach numbers from 1.5 to 4.0 (ref. 10). Three different center-of-gravity locations were investigated and, for some conditions, data were taken for more than one Reynolds number. The data of figure 17(a) indicate the vehicle generally has positive damping for the oscillation amplitudes shown. The low Reynolds number data at Mach number 3.0 indicate a trend toward negative damping near the trim angle of

attack which would indicate a limit cycle of about 3.5°. The data of figure 17(b) are very similar to those of figure 17(a) with a trend toward generally negative damping indicated with decreases in Reynolds number and oscillation amplitude. For the alternate center of gravity (x/d = -0.316, z/d = 0.0442), the data of figure 17(c) indicate the vehicle has less positive damping than the vehicle with the basic center of gravity (x/d = -0.208, z/d = 0.037). This reduced damping would indicate a limit-cycle oscillation of about 4.5° for M = 3.0. As previously noted, the low Reynolds number data indicate a trend toward negative damping.

To further evaluate the damping-in-pitch characteristics, a free-to-tumble test technique was developed. The results of tests using this technique are given in figure 18. A comparison of static pitching-moment coefficient data obtained using the free-to-tumble, transverse-rod test technique with data obtained using the conventional sting-support technique is given in figure 19. The sting-support data were measured at the Ames Unitary Plan Wind Tunnel for almost identical Mach numbers. The data indicate that there are some differences in the pitching-moment coefficient near the maximum values of pitching-moment and that the pitching-moment curve slope through the trim angle of attack is slightly different. These differences are attributable to model support interference. Position-time histories were computed using both sets of pitching-moment coefficient data. Comparisons indicated the only noticeable difference to be frequency of oscillation which is quite small when converted from model to full-scale frequencies. The pitching-moment coefficient data, measured with the transverse-rod support system, were used in the reduction of the dynamic stability parameter.

The variation of the dynamic stability derivative with the angle of attack (fig. 18(a)) indicates that the vehicle has positive damping for the normal operating angle-of-attack range at the subsonic Mach numbers of 0.50 to 0.80. Note that very small values of negative damping exist at zero angle of attack. The vehicle also shows an area of unstable damping near an angle of attack of 180°. The dashed lines indicate areas of insufficient data to evaluate the damping and are extrapolations of existing data. The data of figures 18(b) and 18(c) indicate that the Apollo LEV has positive damping over most of the angle-of-attack range tested. At M = 1.59, there is a range of negative damping near an angle of attack of 180°. At Mach number 1.98, there is a small range of negative damping near the angles of attack at 170° and 190° for two of the reduced frequencies tested. The moment of inertia values (figs. 18(b) and 18(c)) indicate a variation in reduced frequency. The higher the moment of inertia, the lower the reduced frequency parameter. The damping parameter $C_{m_q} + C_{m_{\dot{\alpha}}}$ usually increases with a decrease in reduced frequency.

CONCLUDING REMARKS

Wind-tunnel tests to determine the stability characteristics of the Apollo LEV were made using several wind-tunnel facilities. Static stability characteristics, both thrusting and nonthrusting, were determined at Mach numbers from 0.25 to 6.0.

Dynamic stability parameters were determined using forced-oscillation, limited free-oscillation, and free-to-tumble test techniques at Mach numbers from 0.5 to 6.0. Analyses of the results indicate:

(1) The Apollo LEV is generally stable, both power on and power off, over the normal operating angle-of-attack range near trim angle of attack.

(2) The effect of thrusting rockets is generally destabilizing, especially at the highest thrust coefficients and Mach numbers tested.

(3) The Apollo LEV generally has positive damping over the normal operating angle-of-attack range except for a very small angle range ($\pm 2^\circ$) near the trim angle of attack at subsonic speeds.

Manned Spacecraft Center
National Aeronautics and Space Administration
Houston, Texas, February 9, 1967
914-50-10-03-72

REFERENCES

1. Morgan, James R.; and Fournier, Roger H.: Static Longitudinal Characteristics of a 0.07-Scale Model of a Proposed Apollo Spacecraft at Mach Numbers of 1.57 to 4.65. NASA TM X-603, 1961.

2. Pearson, Albin O.: Wind-Tunnel Investigation of the Static Longitudinal Aerodynamic Characteristics of Models of Reentry and Atmospheric-Abort Configurations of a Proposed Apollo Spacecraft at Mach Numbers from 0.30 to 1.20. NASA TM X-604, 1961.

3. Pearson, Albin O.: Wind-Tunnel Investigation of the Static Longitudinal Aerodynamic Characteristics of a Modified Model of a Proposed Apollo Atmospheric-Abort Configuration at Mach Numbers from 0.30 to 1.20. NASA TM X-686, 1962.

4. Fournier, Roger H.; and Corlett, William A.: Aerodynamic Characteristics in Pitch of Several Models of the Apollo Abort System from Mach 1.57 to 2.16. NASA TM X-910, 1964.

5. Moseley, William C., Jr.; and Martino, Joseph C.: Apollo Wind Tunnel Program Development of General Configurations. NASA TN D-3748, Dec. 1966.

6. Moseley, William C., Jr.; Moore, Robert H., Jr.; and Hughes, Jack E.: Stability Characteristics of the Apollo Command Module. NASA TN D-3890, 1967.

7. Runckel, Jack F.; Schmeer, James W.; and Pendergraft, Odis C., Jr.: Static Longitudinal Aerodynamic Characteristics of a Powered Model of the Apollo Launch Escape Vehicle from Mach Numbers 0.50 to 1.30. NASA TM X-1215, March 1966.

8. Welsh, C. J.; Hance, Q. P.; and Ward, L. K.: A Forced Oscillation Balance System for the von Karman Facility 40- by 50-Inch Supersonic Tunnel. AEDC-TN-61-63, May 1961.

9. Campbell, John P.; Johnson, Joseph L., Jr.; and Hewes, Donald E.: Low-Speed Study of the Effect of Frequency on the Stability Derivatives of Wings Oscillating in Yaw with Particular Reference to High Angle-of-Attack Conditions. NACA RM L55H05, 1955.

10. Hodapp, A. E., Jr.: Free-Oscillation Dynamic Stability Tests of a 0.05-Scale Apollo Command Module and a 0.059-Scale Apollo Launch Escape Vehicle at Supersonic Speeds. AEDC-TR-63-186, 1963.

11. Runckel, Jack F.; and Swihart, John M.: A Hydrogen Peroxide Hot Jet Simulator for Wind-Tunnel Tests of Turbojet-Exit Models. NASA Memo 1-10-59L, 1959.

12. Davis, N. S., Jr.; and McCormick, James C.: Design of Catalyst Packs for the Decomposition of Hydrogen Peroxide (Preprint) 1246-60 American Rocket Society, July 1960.

13. Huff, Ronald G.; and Abdalla, Kaleel L.: Mixing Characteristics Downstream of Core Region of High Temperature Axisymmetric Jets Exhausting into Transonic and Supersonic Streams. NASA TM X-151, 1960.

14. Pindzola, M.: Jet Simulation in Ground Test Facilities. Agardograph 79, Nov. 1963.

15. Jones, Jerry H.; and Hilliard, E. E.: Jet Effects Tests on the Apollo Launch Escape Vehicle at Mach 1.5 through 6.0. AEDC-TDR-63-240, 1963.

16. Jones, Jerry H.: Jet Effects Tests on the Apollo Launch Escape Vehicle at Mach 1.5 through 4. AEDC-TDR-64-92, 1964.

17. Babcock, D. L.; and Wiltse, P. D.: Motor Vehicle Interfaces in the Apollo Launch Escape System. Paper No. 65-152, Am. Inst. Aeron. Astronaut., Feb. 1965.

18. Ward, L. K.; and Hodapp, A. E., Jr.: Dynamic Stability Tests of a 0.059-Scale Apollo Launch Escape Vehicle Model at Mach Numbers 1.5 through 6, April 1963. AEDC-TDR-65-63, 1965.

19. Boisseau, Peter C.: Low-Speed Static and Oscillatory Stability Characteristics of a Model of the Apollo Launch-Escape Vehicle and Command Module. NASA TM X-894, 1963.

20. Kilgore, Robert A.; and Averett, Benjamin T.: Wind-Tunnel Measurements of Some Dynamic Stability Characteristics of 0.055-Scale Models of Proposed Apollo Command Module and Launch-Escape Configurations at Mach Numbers from 2.40 to 4.65. NASA TM X-769, 1963.

21. Averett, Benjamin T.; and Kilgore, Robert A.: Dynamic-Stability Characteristics of Proposed Apollo Configurations at Mach Numbers from 0.30 to 1.20. NASA TM X-912, 1964.

22. Averett, Benjamin T.; and Wright, Bruce R.: Some Dynamic-Stability Characteristics of Models of Proposed Apollo Configurations at Mach Numbers from 1.60 to 2.75. NASA TM X-971, 1964.

23. Averett, Benjamin T.: Dynamic-Stability Characteristics in Pitch of Models of Proposed Apollo Configurations at Mach Numbers from 0.30 to 4.63. NASA TM X-1127, 1965.

TABLE I.- TEST FACILITIES AND CAPABILITIES

Test facility	Size of test section	Mach number range	Reynolds number range, $\times 10^{-6}$
	Continuous tunnels		
Ames Unitary Plan Wind Tunnel (Ames-UPWT)	8 × 7 ft 9 × 7 ft 11 × 11 ft	2.4 to 3.5 1.5 to 2.6 0.7 to 1.4	0.5 to 5 per ft 1 to 7 per ft 1 to 10 per ft
Ames 12-Foot Pressure Tunnel (Ames 12-ft)	12 ft diameter	0.0 to 0.95	0.5 to 9.0 per ft
Arnold Engineering Development Center, Tunnel A (AEDC-A)	40 × 40 in.	1.5 to 6.0	0.3 to 9 per ft
Langley Research Center 16-ft Transonic Tunnel (LRC 16-ft)	16 ft (octagonal)	0.5 to 1.3	1.2 to 3.7 per ft
Lewis Research Center Supersonic Wind Tunnel (LeRC-SWT)	8 × 6 ft	0.8 to 2.1	4.15 to 8.5 per ft
	Intermittent tunnels		
North American Aviation Trisonic Wind Tunnel (NAA-TWT)	7 × 7 ft	0.2 to 3.5	5 to 14 per ft

TABLE II. - MODELS AND TEST RANGES

Model	Scale	Facility	Mach number range	Reynolds number range, $\times 10^{-6}$	α range, deg	Test type
FS-2	0.105	Ames 12-ft	0.25 and 0.50	5.42 to 10.34	-10 to 40	Static, non-thrusting
		Ames-UPWT	.7 to 3.4	3.4 to 5.2	-3 to 55	Static, non-thrusting
		Ames-UPWT	.5 to 1.35	3.5 to 6.8	-16 to 35	Static, non-thrusting
FS-3	0.045	AEDC-A	4.0 to 6.0	3.5 to 0.40	-10 to 60	Static, non-thrusting
FSJ-1	0.085	LRC 16-ft	0.5 to 1.3	3.1 to 4.2	0 to 61	Static, thrusting, (hot jet)
FSJ-3	0.045	AEDC-A	0.7 to 5.97	0.6 to 2.05	0 to 50	Static, thrusting, (cold jet)
FD-3	0.059	AEDC-A	2.0 to 6.0	4.0 to 6.0	-5 to 15	Dynamic, forced oscillation
FD-5	0.05	AEDC-A	1.5 to 6.0	0.31 to 5.3	18° oscillation amplitude	Dynamic, limited free oscillation
FD-9	0.059	NAA-TWT	0.5, 0.7, and 0.8	3.14 to 4.86	Free to tumble	Dynamic
		LeRC-SWT	1.59 and 1.98	3.56 to 3.88	Free to tumble	Dynamic

TABLE III. - TEST CONDITIONS

Facility	Mach number	$R \times 10^{-6}$ (a)	Stagnation pressure, psia	Dynamic pressure, psf	Stagnation temperature, °F
Ames 12-ft	0.25	5.52			
	.25	10.34			
	.50	5.42			
Ames-UPWT	0.5	6.87		540	
	.7	5.2		540	
	.9	4.32		540	
	1.1	3.85		540	
	1.2	3.57		540	
	1.35	3.57		540	
Ames-UPWT (alternate configuration)	0.7	5.22		540	
	.9	4.34		540	
	1.1	3.85		540	
	1.2	3.70		540	
	1.35	3.60		540	
	1.55	3.49		540	
	2.0	3.43		540	
	2.4	3.65		540	
	3.0	3.90		540	
	3.4	3.60		540	
AEDC-A (alternate configuration)	4.0	3.5	65.0	691	116
	5.0	.7	25.2	115	152
	6.0	.4	29.8	72	148
LRC 16-ft	0.5	3.1	12.4	317	
	.7	3.9	10.6	518	
	.9	4.3	8.7	677	
	1.0	4.4	7.8	777	
	1.1	4.4	7.1	835	
	1.2	4.3	6.1	878	
	1.3	4.2	5.3	907	

[a]Based on model diameter.

TABLE III. - TEST CONDITIONS - Concluded

Facility	Mach number	$R \times 10^{-6}$ (a)	Stagnation pressure, psia	Dynamic pressure, psf	Stagnation temperature, °F
AEDC-A	0.7	2.05	13.80	493	86
	1.48	1.42	8.21	508	89
	1.98	1.42	9.69	505	90
	2.99	1.70	19.56	487	70
	3.99	1.29	25.13	269.5	96
	4.99	.695	22.15	106.4	96
	5.97	.659	31.9	750	86
AEDC-A	2.0	6.0	32.5	1675	101
	3.0	4.0	36.8	908.8	108
	4.0	5.0	74.0	779.5	98
	6.0	4.8	200.0	200	180
	6.0	4.7	195.8	456.2	102
AEDC-A	1.5	3.25		868	
	2.0	.65		165.8	
	2.0	3.56		927.5	
	3.0	5.26		1089.2	
	3.0	.5		102.1	
	4.0	5.07		794.0	
	4.0	.42		65.1	
NAA-TWT	0.5	4.80		640	
	.7	3.98		705	
	.8	4.31		838	
LeRC-SWT	1.59	3.56		1160	
	1.98	3.75		1295	

[a]Based on model diameter.

TABLE IV. - ACCURACY OF TABULATED DATA

Test facility	Type data	Mach number	$\pm C_N$	$\pm C_A$	$\pm C_{m,a}$
Ames 12-ft	Static, nonthrusting	0.25, 0.50	0.0071	0.0061	0.0046
Ames-UPWT (alternate configuration)	Static, nonthrusting	0.7 to 0.9	0.0113	0.0139	0.0105
		1.1 to 3.0	.0114	.0139	.0105
		3.4	.0114	.0176	.0133
LRC 16-ft	Static, thrusting (low thrust coefficients)	0.5	0.0585	0.0661	0.0128
		.7	.0372	.0333	.0064
		.9	.0268	.0234	.0045
		1.0	.0242	.0210	.0040
		1.1	.0227	.0198	.0038
		1.2	.0215	.0185	.0035
		1.3	.0209	.0180	.0034
LRC 16-ft	Static, thrusting (high thrust coefficients)	0.5	0.0485	0.0467	0.0090
		.7	.0263	.0236	.0045
		.9	.0189	.0165	.0032
		1.0	.0171	.0148	.0028
		1.1	.0160	.0139	.0027
		1.2	.0152	.0130	.0025
		1.3	.0148	.0127	.0024
AEDC-A	Static, thrusting	0.7	0.0482	0.0482	0.0181
		1.48	.0077	.0077	.0082
		1.98	.0127	.0109	.0084
		2.99	.0161	.0129	.0091
		3.99	.0164	.0141	.0125
		4.99	.0225	.0225	.0268
		5.97	.0270	.0280	.0374

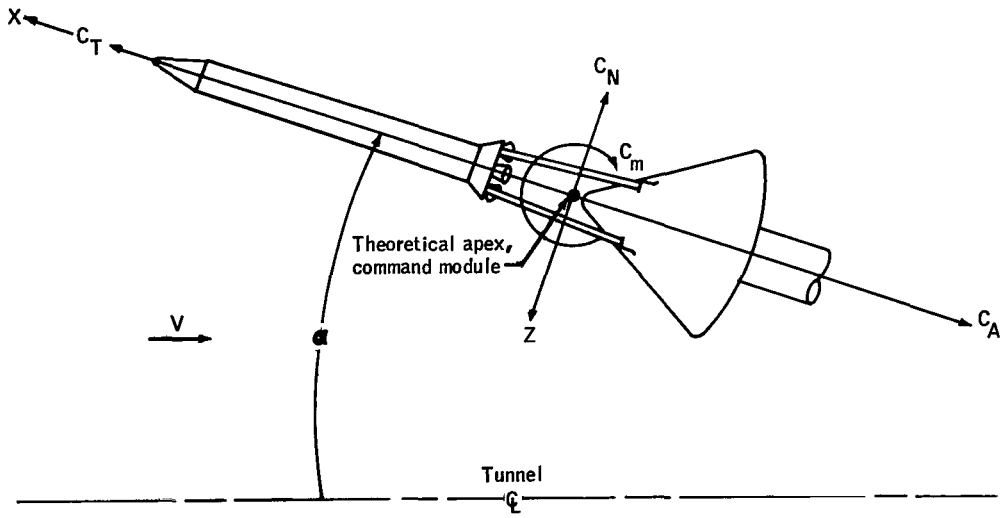

Figure 1. - Body system of axes. Force and moment coefficients on model including rocket thrust component. Arrows indicate positive direction.

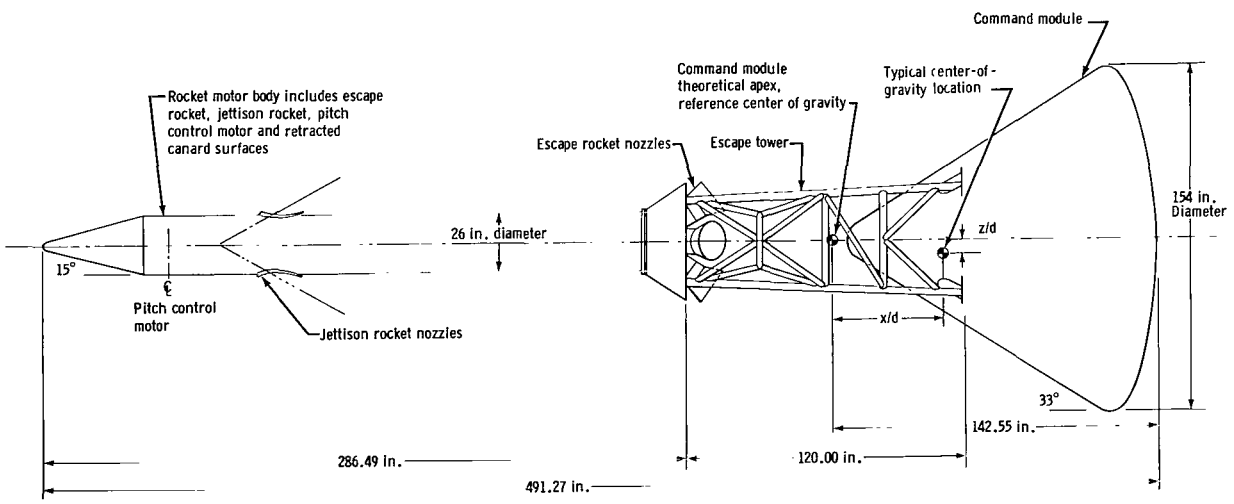

Figure 2. - Sketch of Apollo launch escape vehicle. Dimensions are for full-scale vehicle.

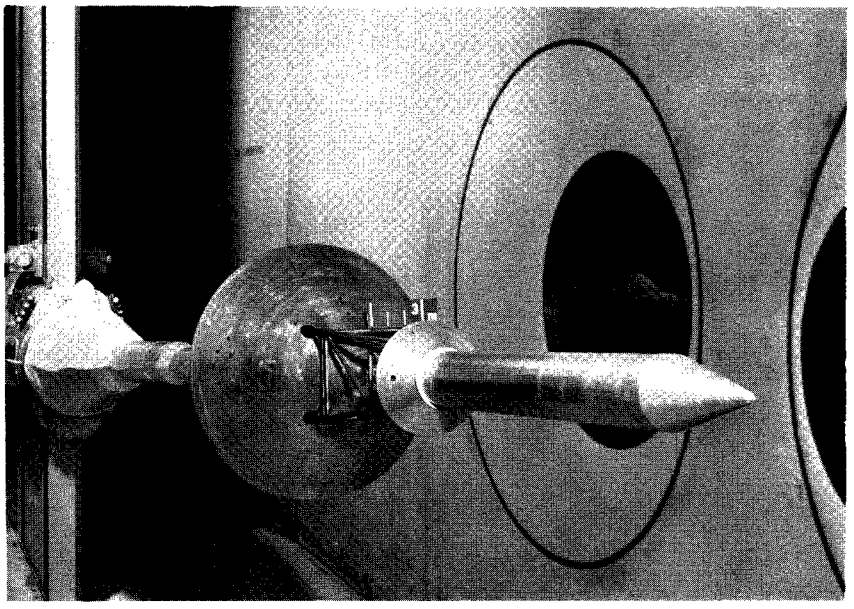

(a) Apollo LEV model installed in the 8- by 7-foot test section of the Ames Unitary Plan Wind Tunnel.

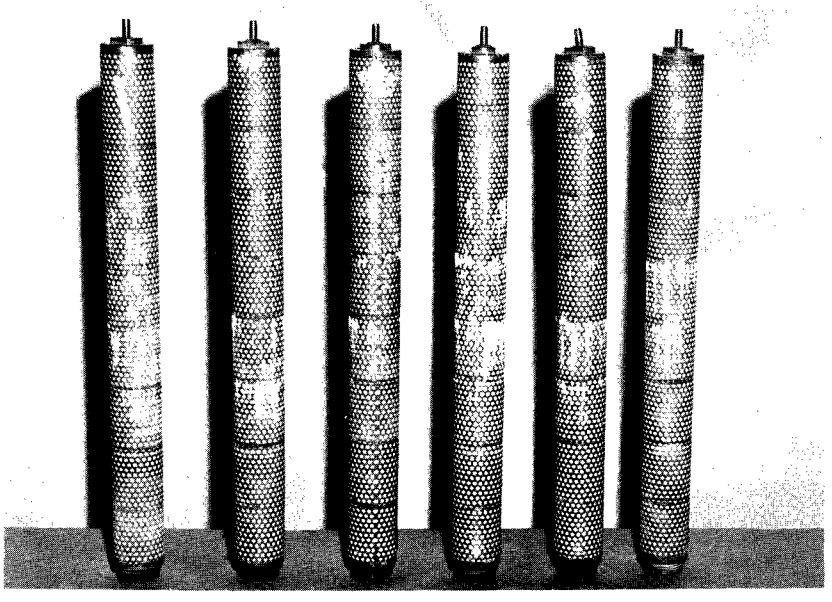

(b) Catalyst packs used in escape motor for hot-jet thrusting simulation.

Figure 3. - Photographs of test models and components.

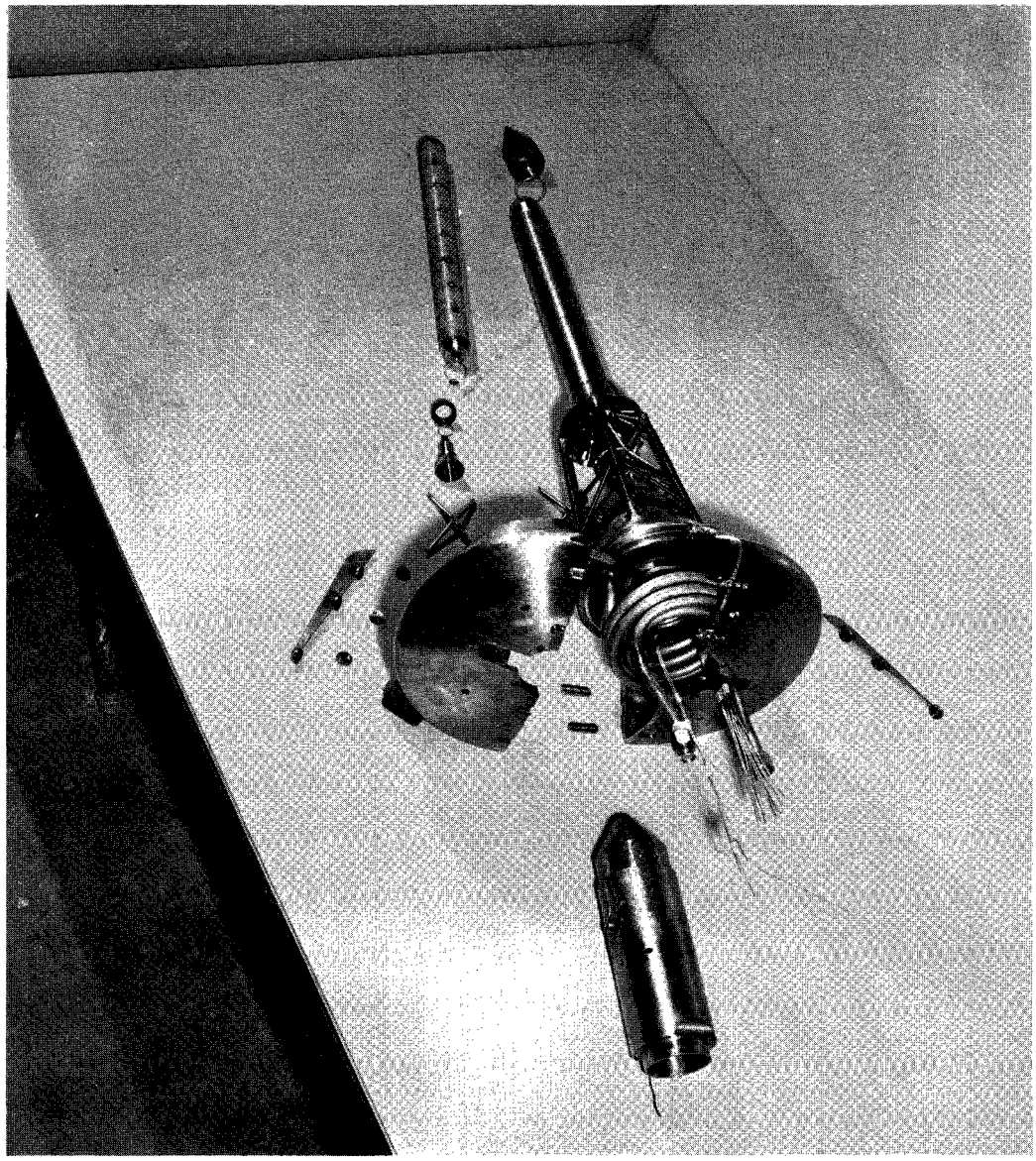

(c) Breakdown of the hot-jet model of the Apollo LEV showing component parts.

Figure 3. - Continued.

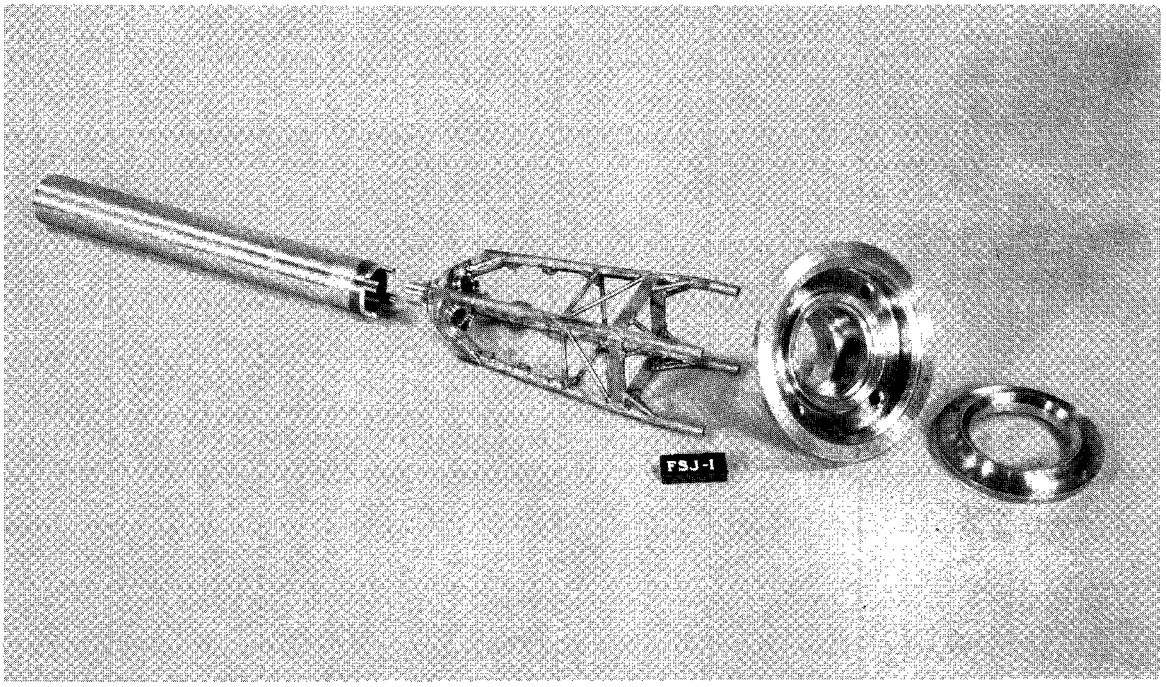

(d) Hot-jet model tower showing hollow legs for conducting H_2O_2 to catalyst pack in escape motor.

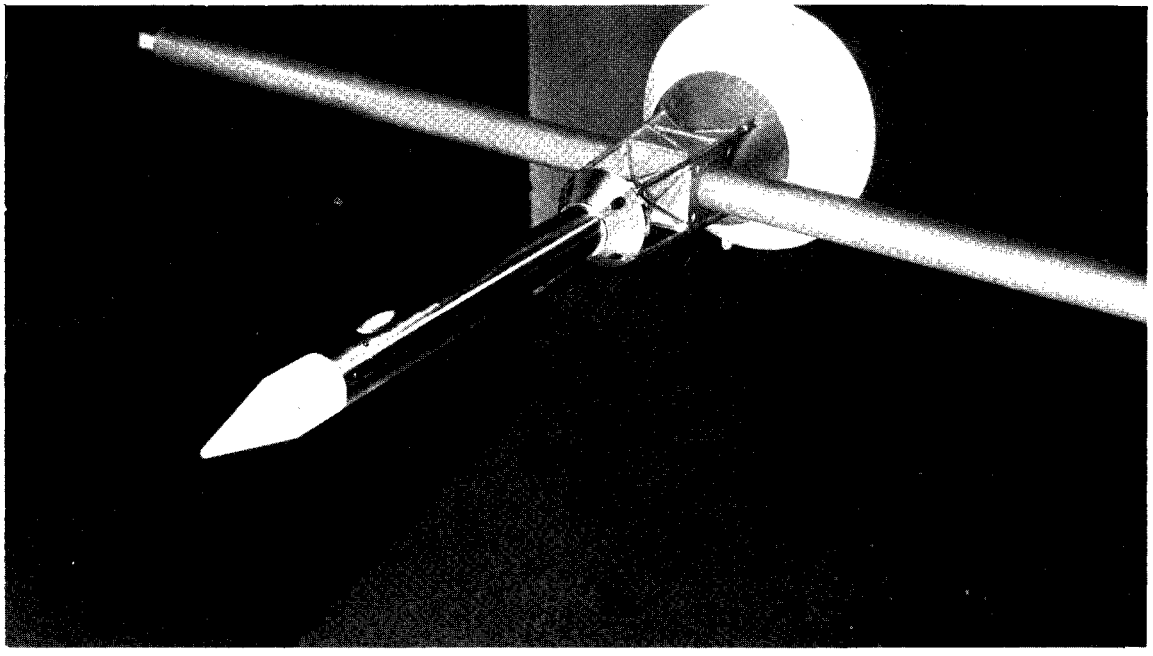

(e) View of the Apollo LEV model mounted on the transverse rod dynamic stability test setup in the NAA Trisonic Wind Tunnel.

Figure 3. - Concluded.

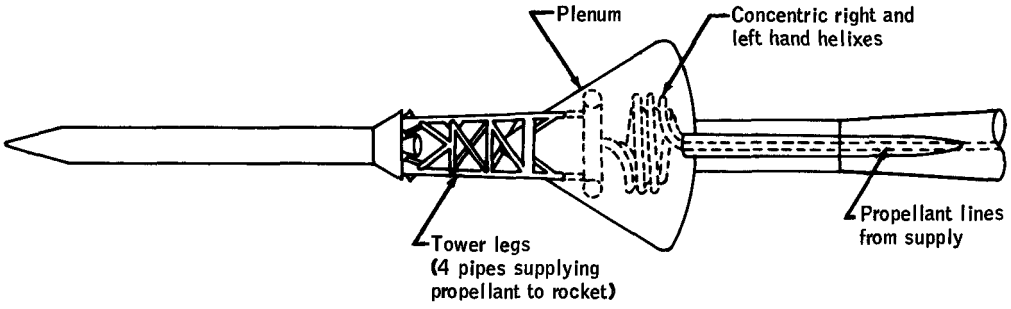

Figure 4. - Model drawing showing propellant lines.

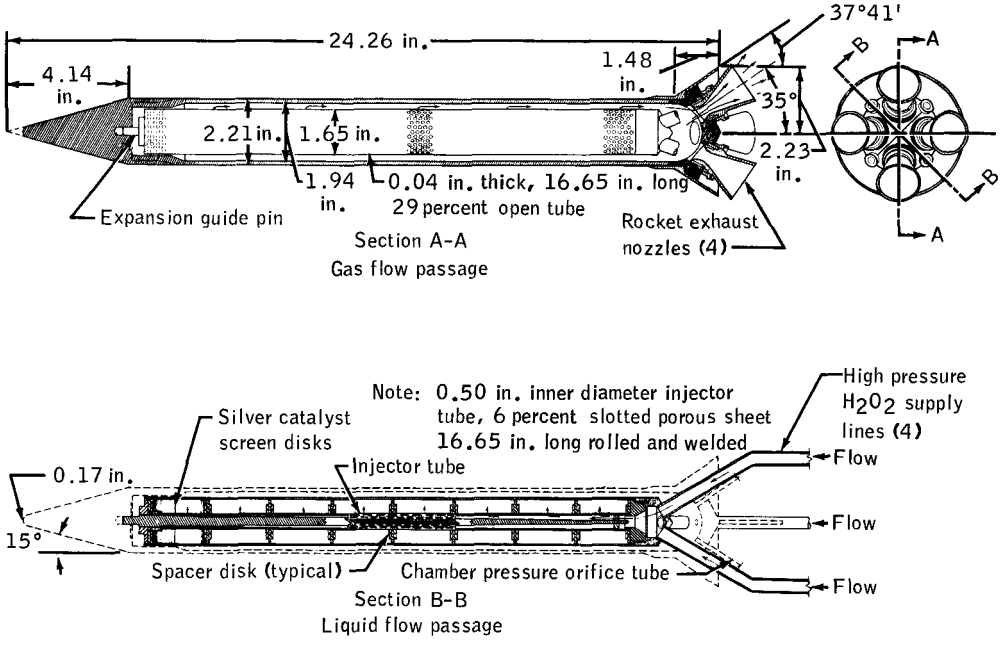

Figure 5. - Sketch of radial flow decomposition chamber.

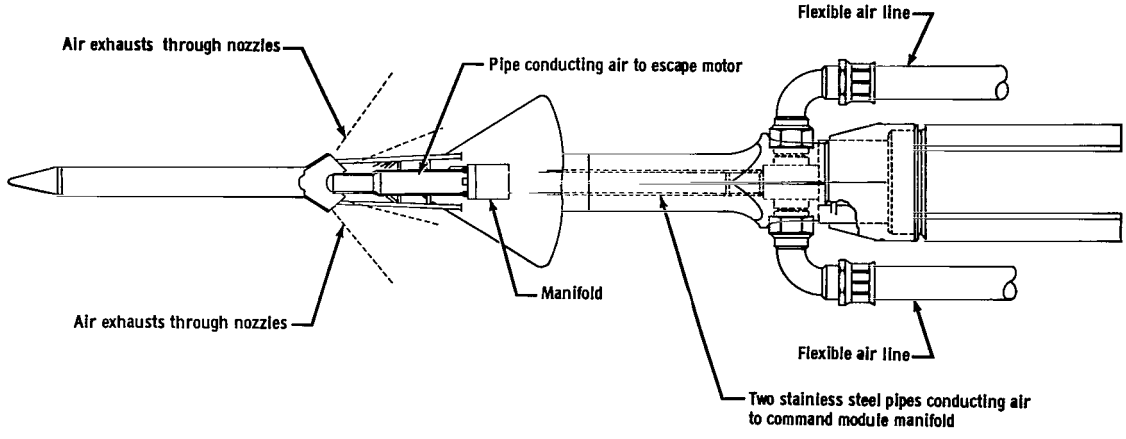

Figure 6. - Sketch showing cold-jet simulation technique. Air system is physically isolated from model.

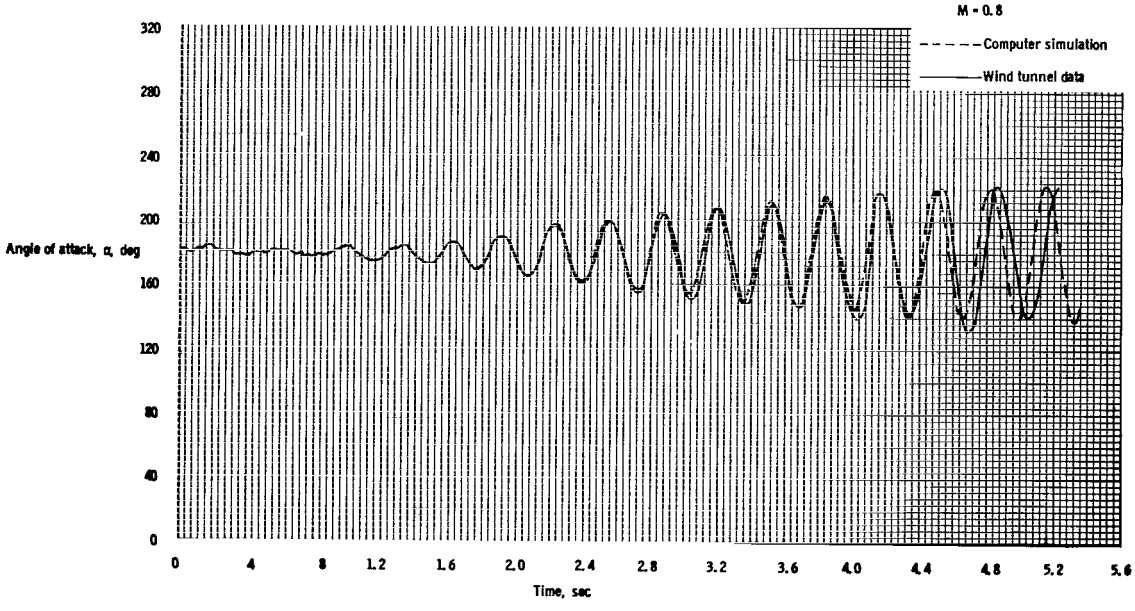

Figure 7. - A comparison of computer simulated and wind-tunnel position-time histories (diverging from heat-shield-forward trim position).

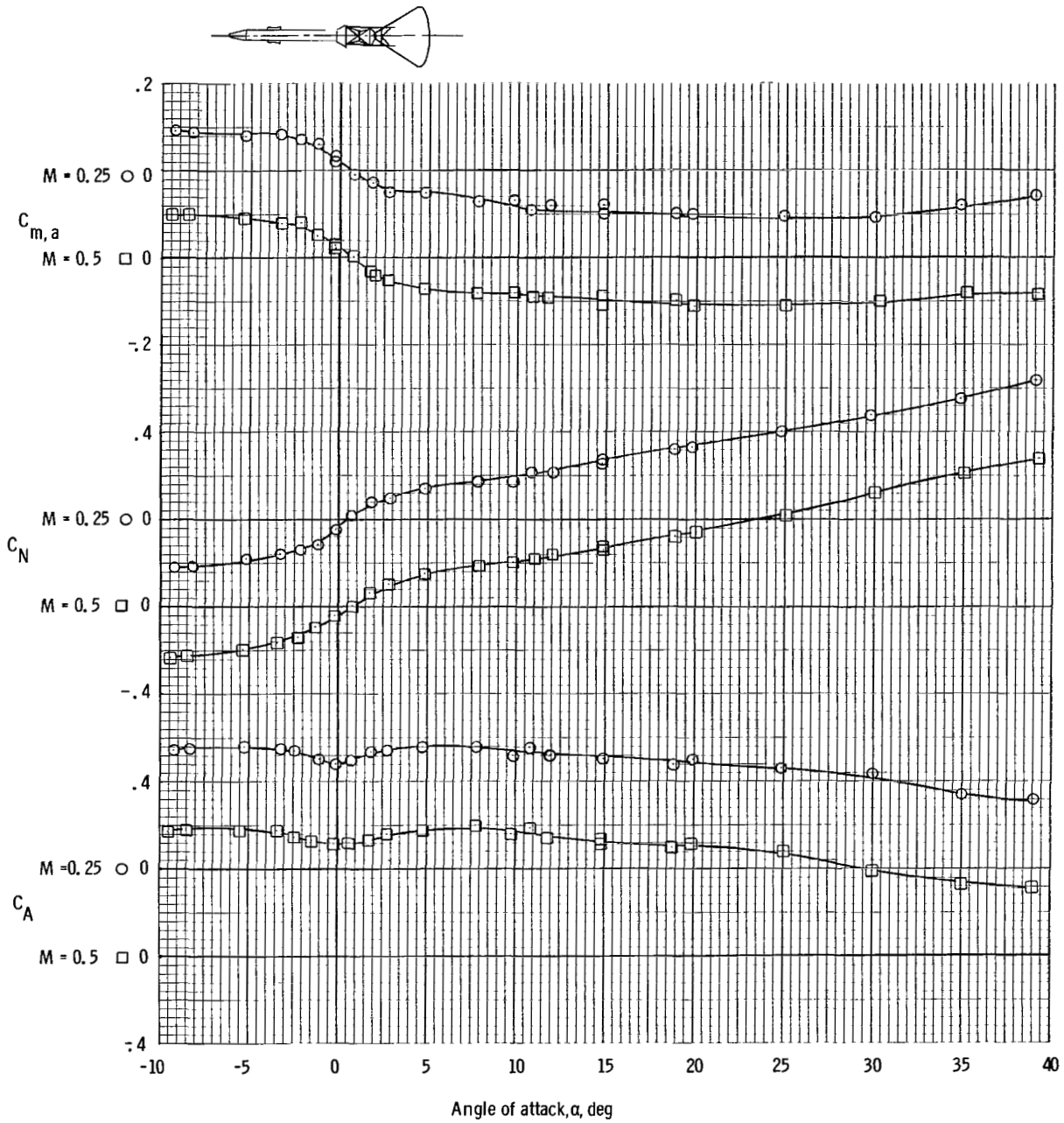

Figure 8. - Static longitudinal stability characteristics for the Apollo launch escape vehicle at Mach numbers 0.25 and 0.5 as determined in the Ames 12-Foot Tunnel.

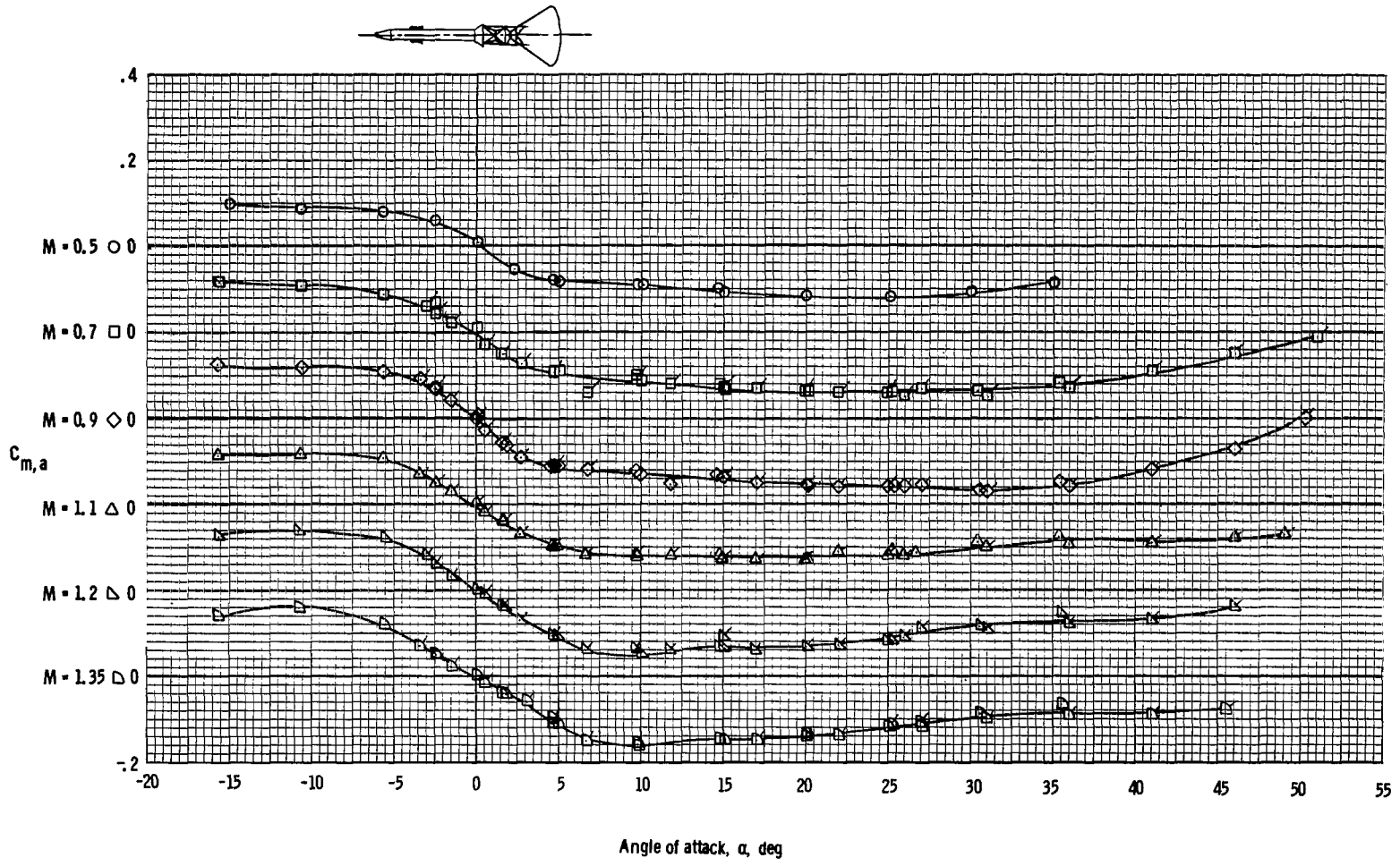

(a) Pitching-moment coefficient.

Figure 9. - Static longitudinal stability characteristics for the Apollo launch escape vehicle at Mach numbers from 0.5 to 6.0 as determined in the Ames UPWT and the AEDC-A Tunnel. (Flagged symbols denote data for an alternate configuration.)

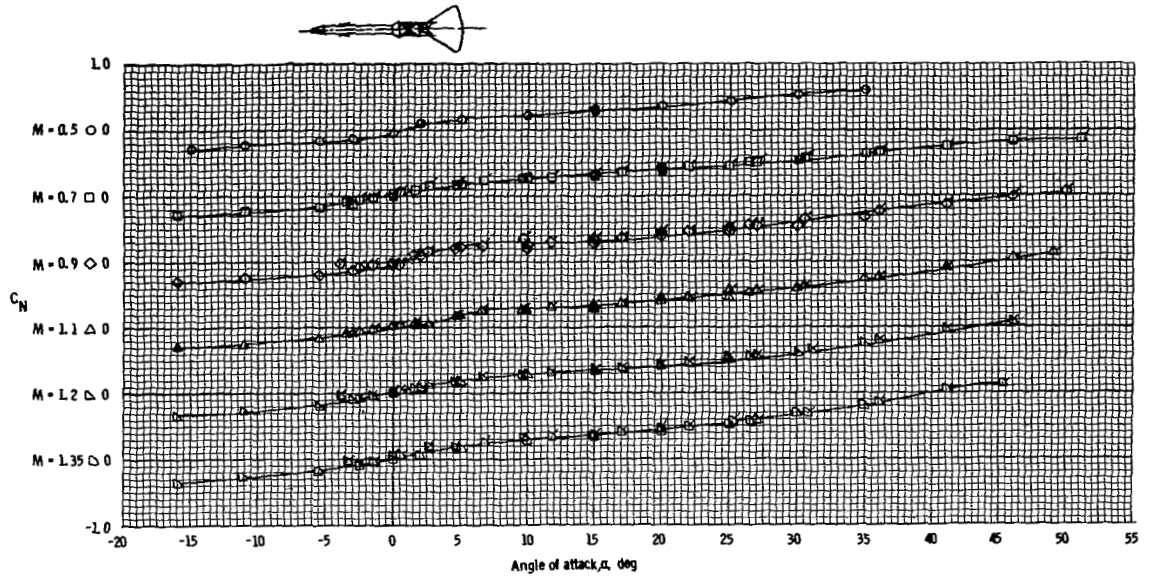

(b) Normal-force coefficient.

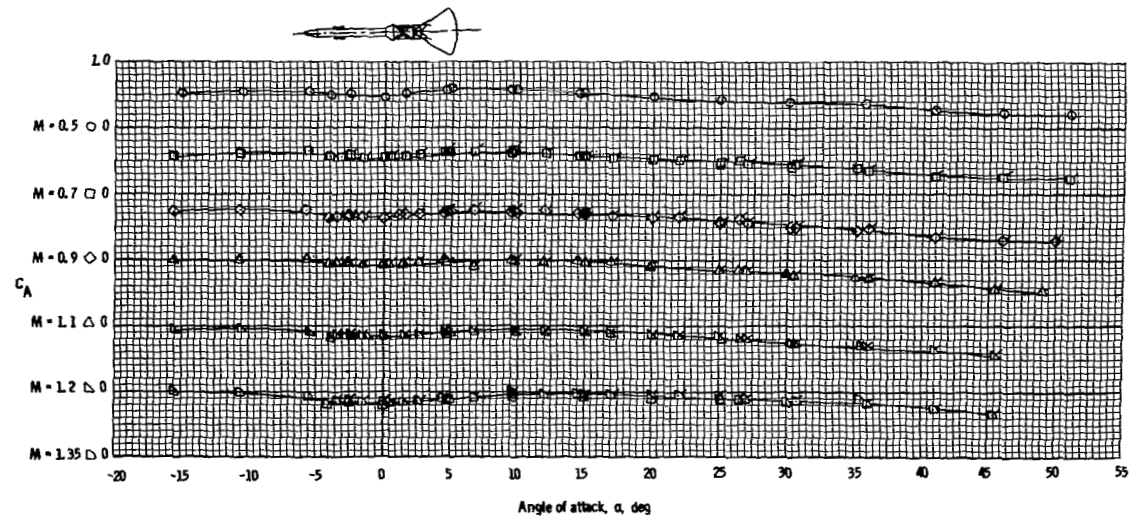

(c) Axial-force coefficient.

Figure 9. - Continued.

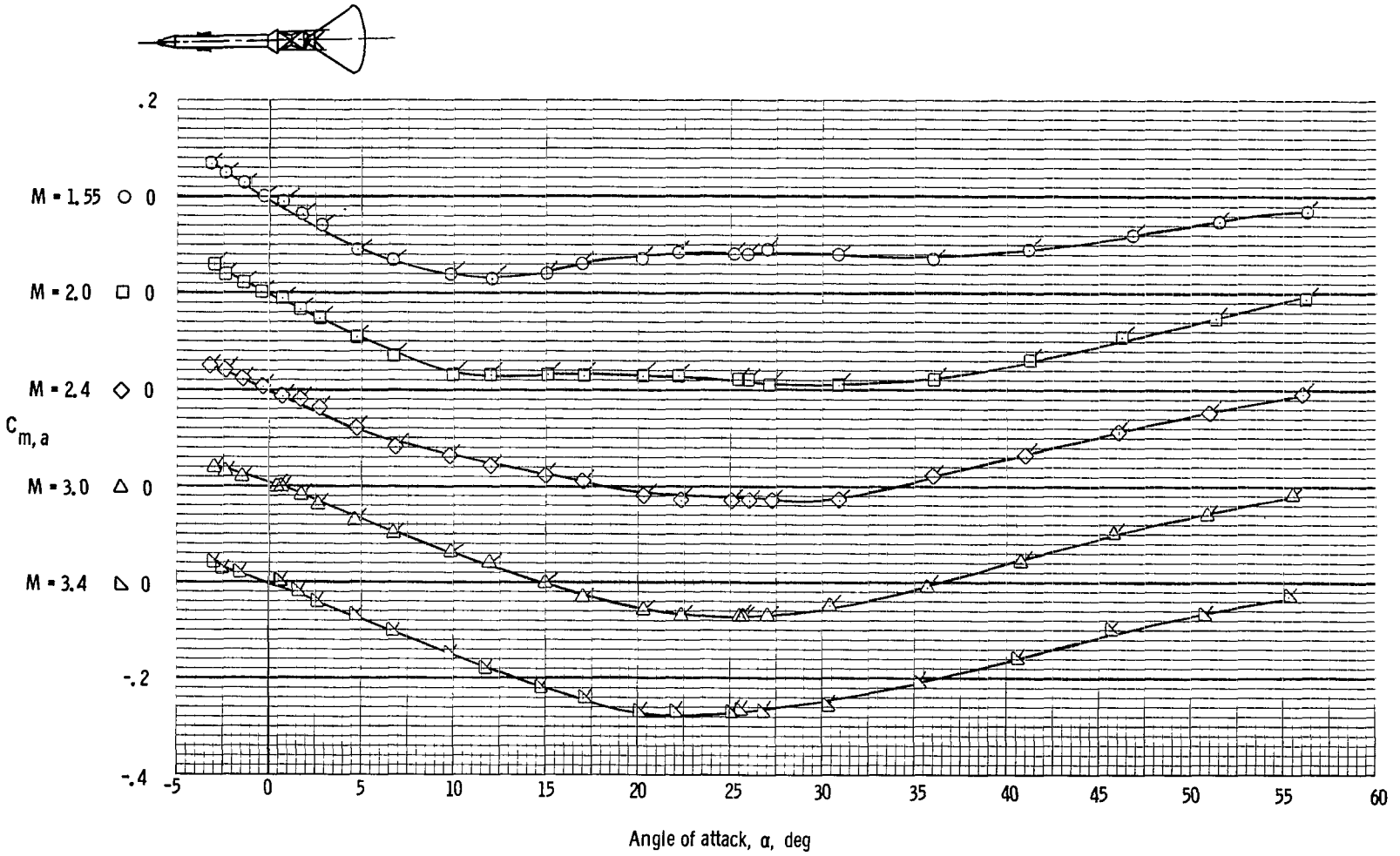

(d) Pitching-moment coefficient.

Figure 9. - Continued.

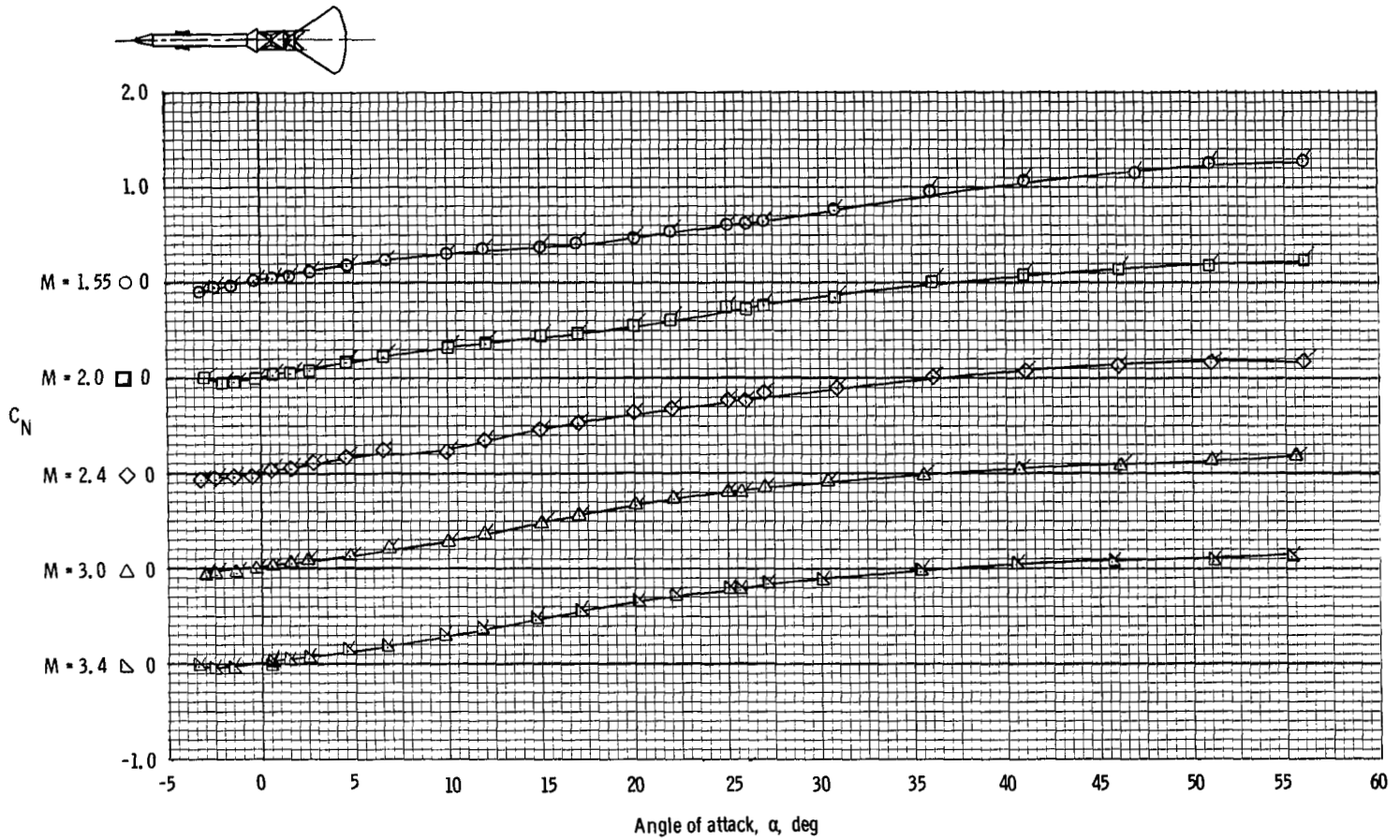

(e) Normal-force coefficient.

Figure 9. - Continued.

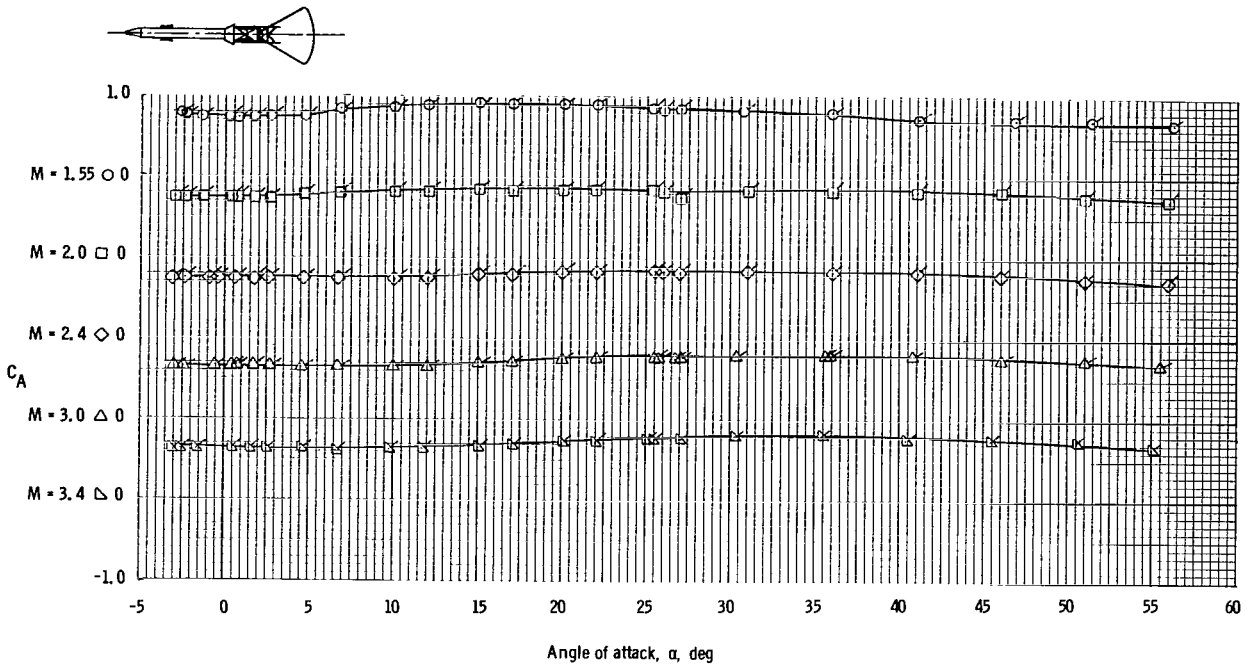

(f) Axial-force coefficient.

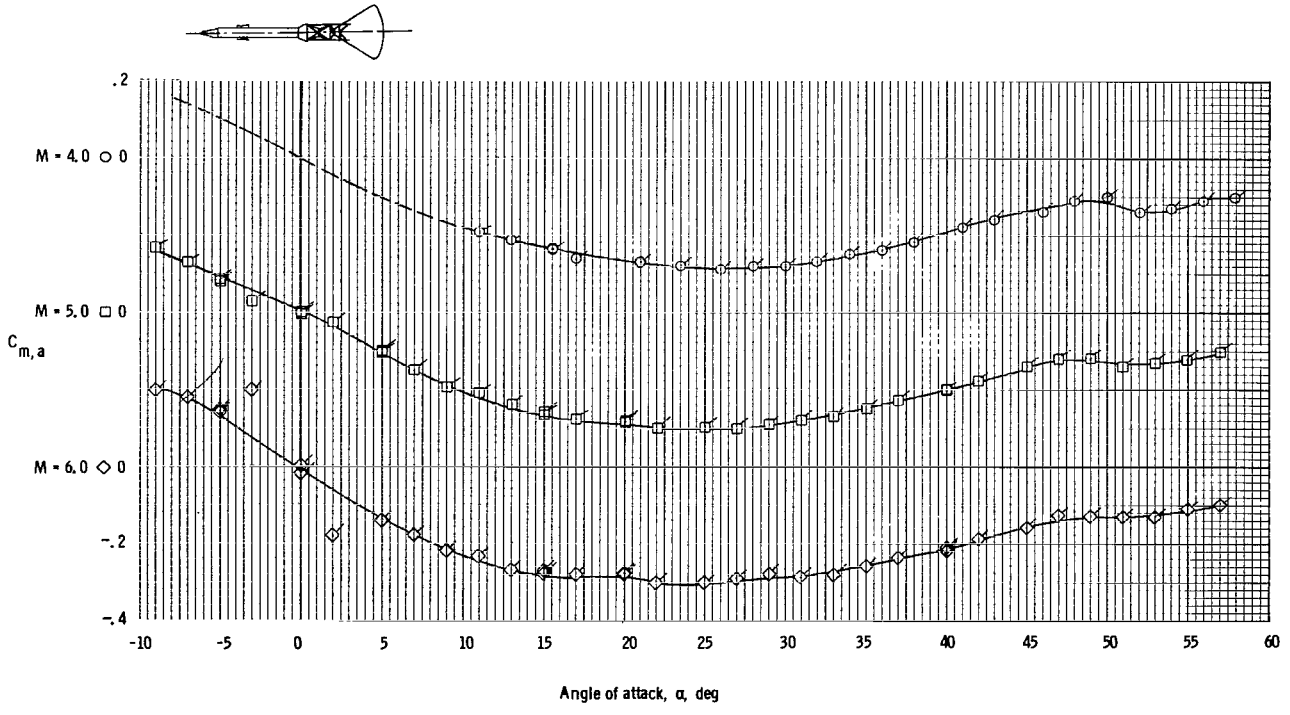

(g) Pitching-moment coefficient.

Figure 9. - Continued.

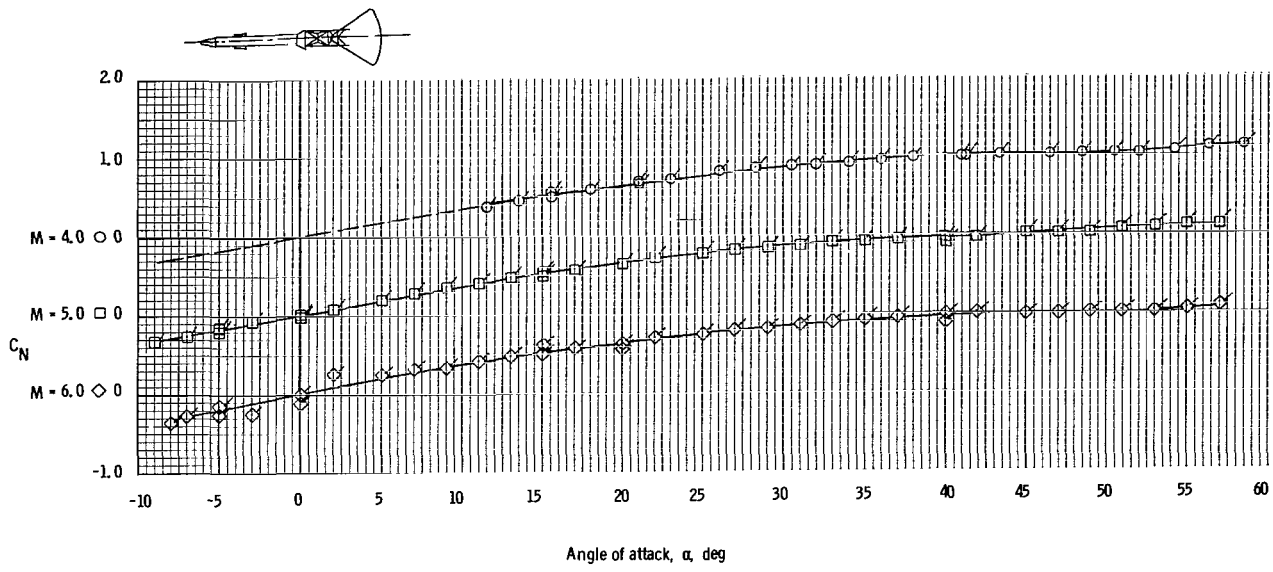

(h) Normal-force coefficient.

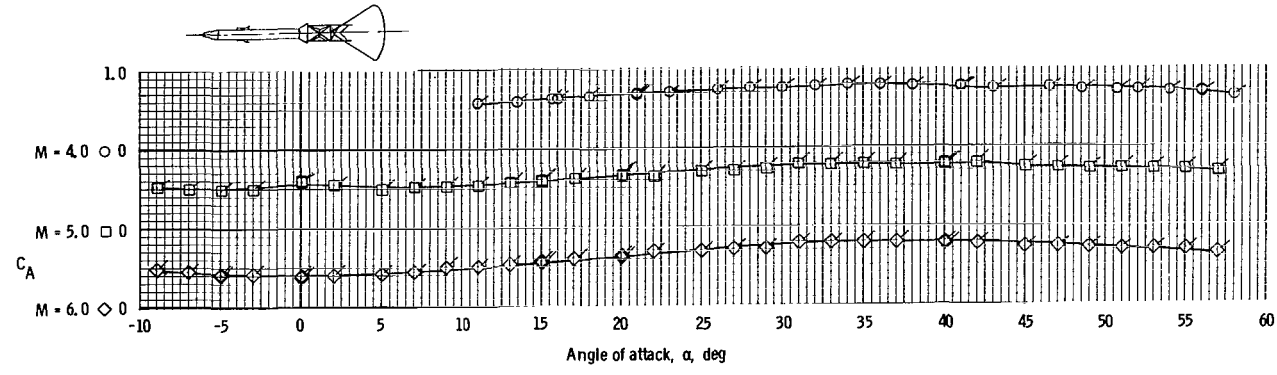

(i) Axial-force coefficient.

Figure 9. - Concluded.

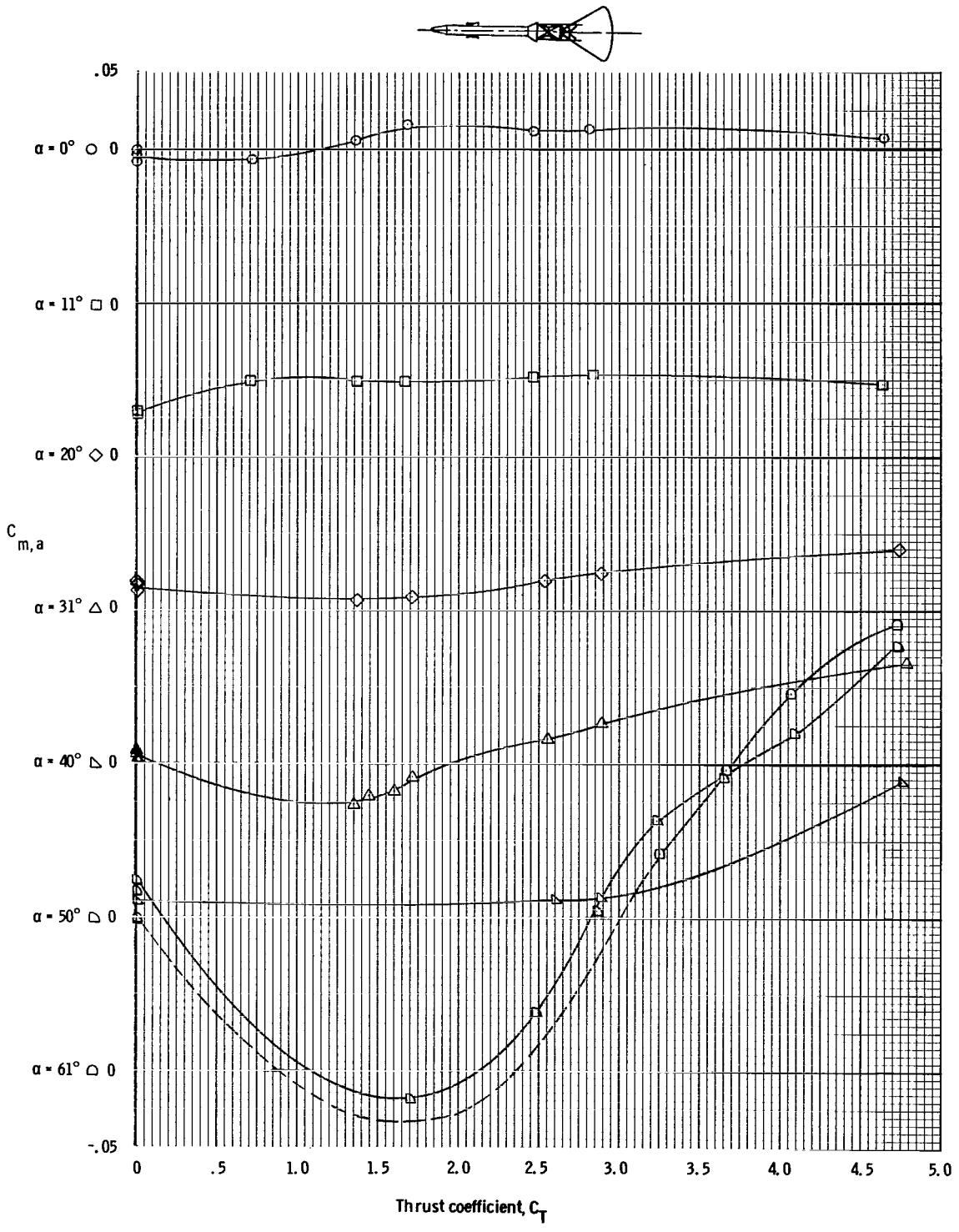

(a) Variation of pitching-moment coefficient with thrust coefficient at M = 0.5.

Figure 10. - Static, thrusting longitudinal stability characteristics for the Apollo launch escape vehicle at Mach numbers 0.5 to 1.3 as determined in the Langley 16-Foot Wind Tunnel.

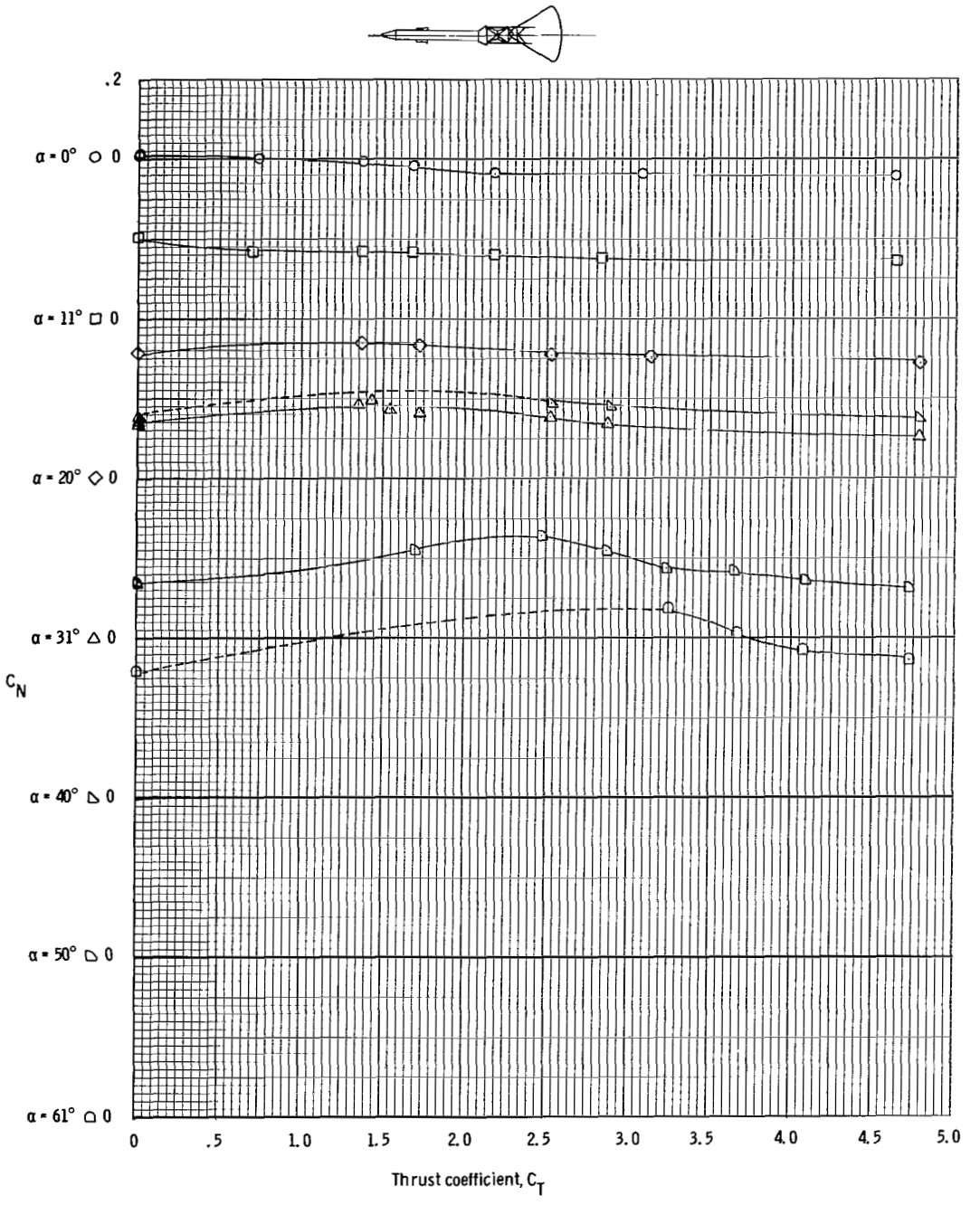

(b) Variation of normal-force coefficient with thrust coefficient at M = 0.5.

Figure 10. - Continued.

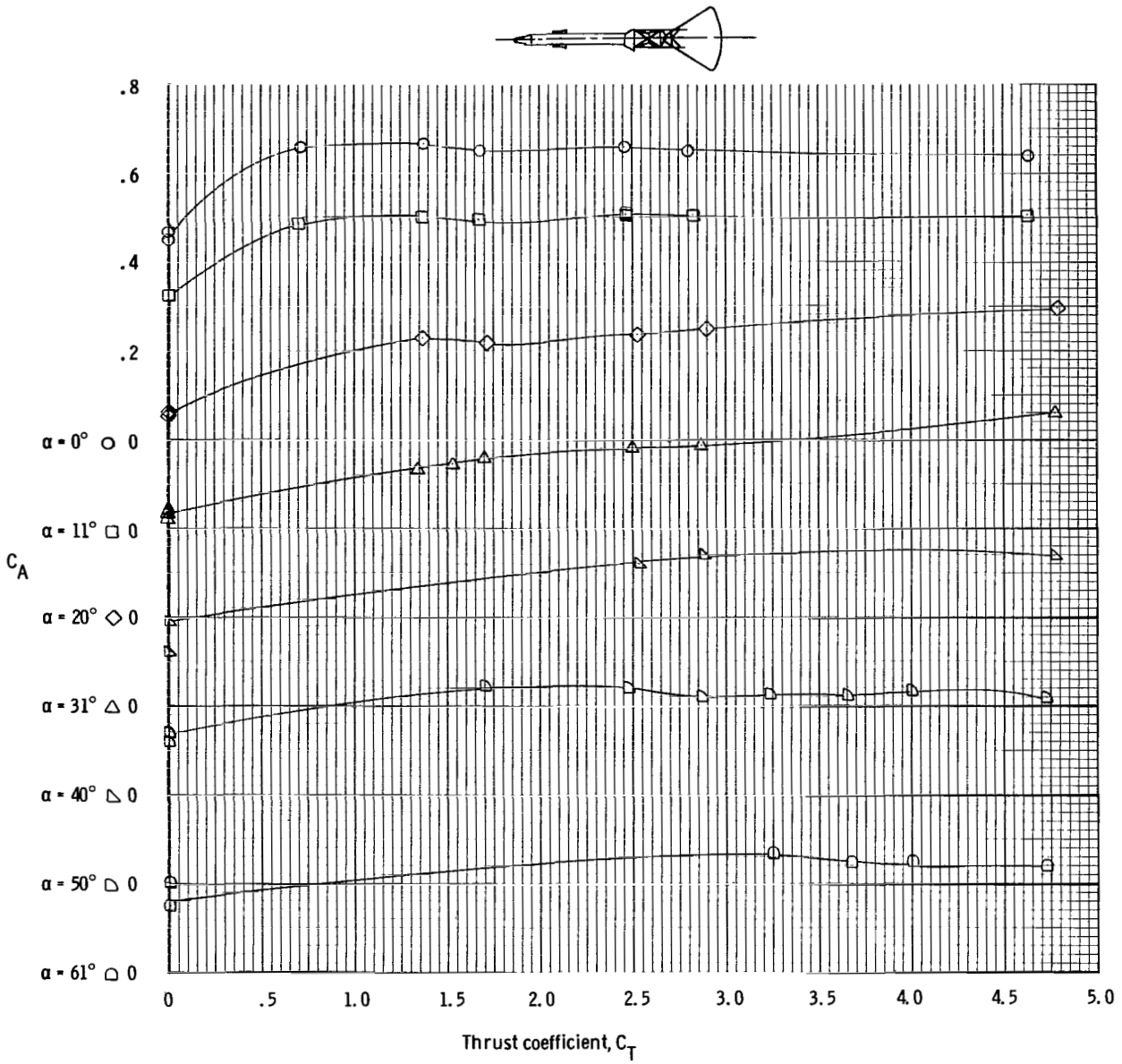

(c) Variation of axial-force coefficient with thrust coefficient at M = 0.5.

Figure 10. - Continued.

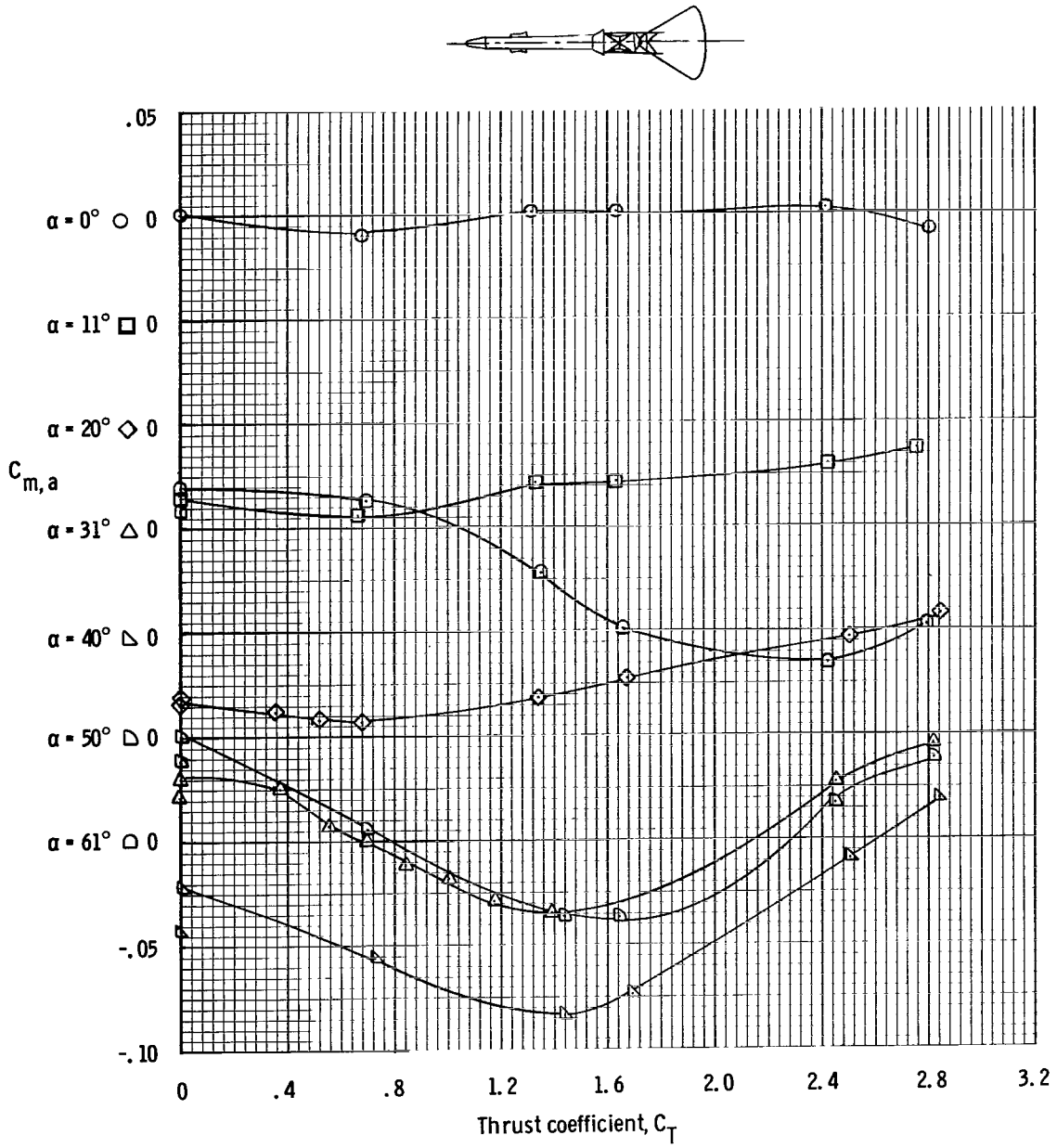

(d) Variation of pitching-moment coefficient with thrust coefficient at M = 0.7.

Figure 10. - Continued.

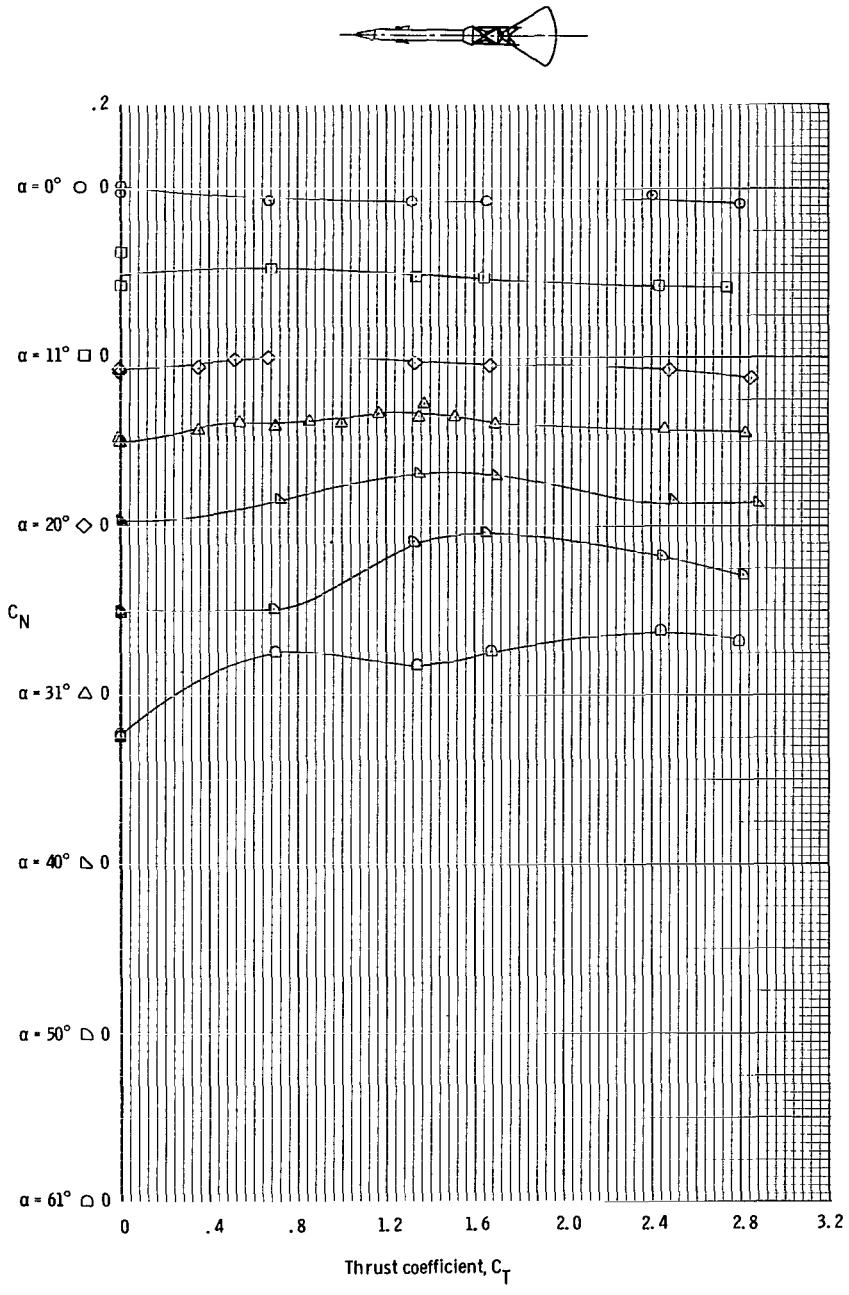

(e) Variation of normal-force coefficient with thrust coefficient at M = 0.7.

Figure 10. - Continued.

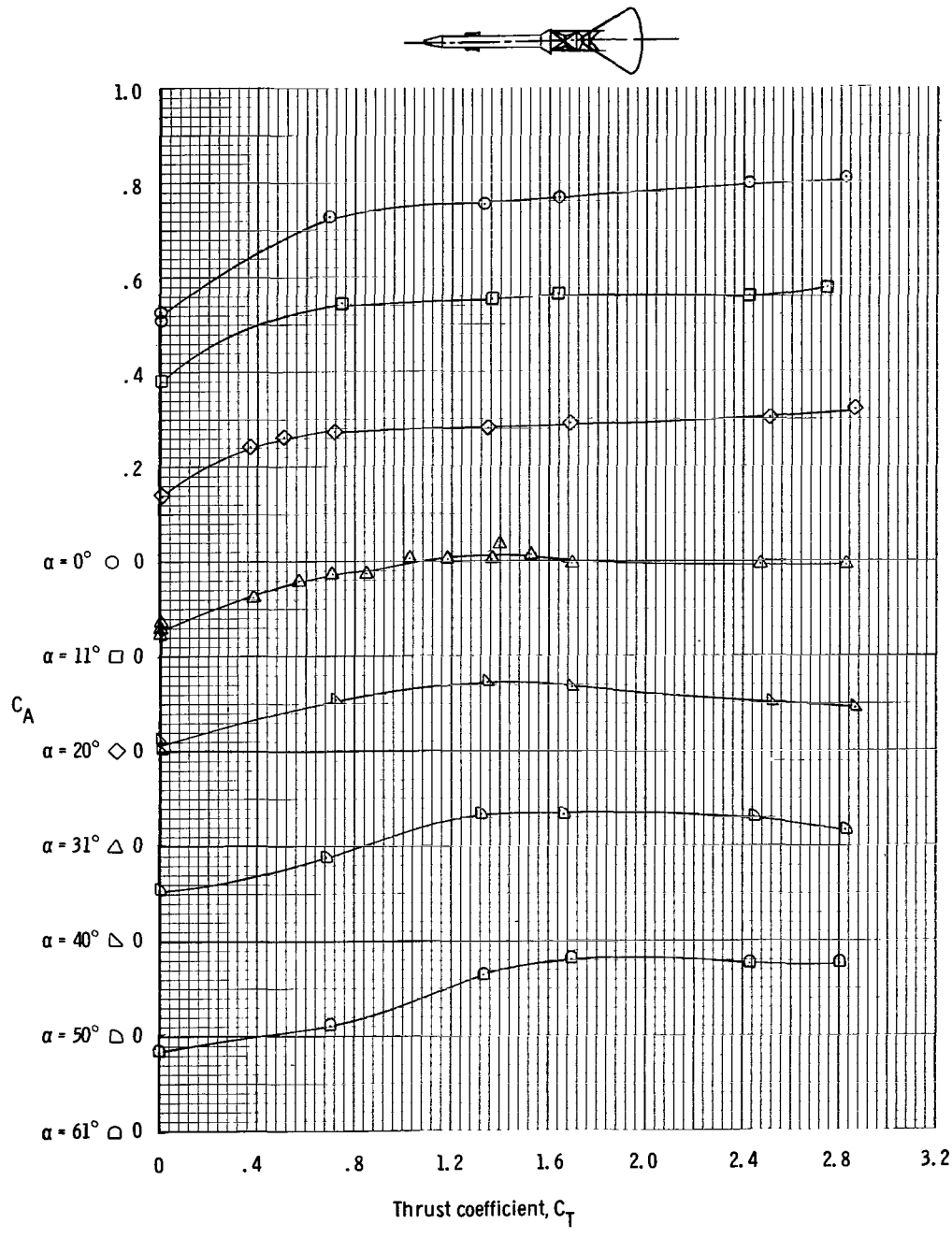

(f) Variation of axial-force coefficient with thrust coefficient at M = 0.7.

Figure 10. - Continued.

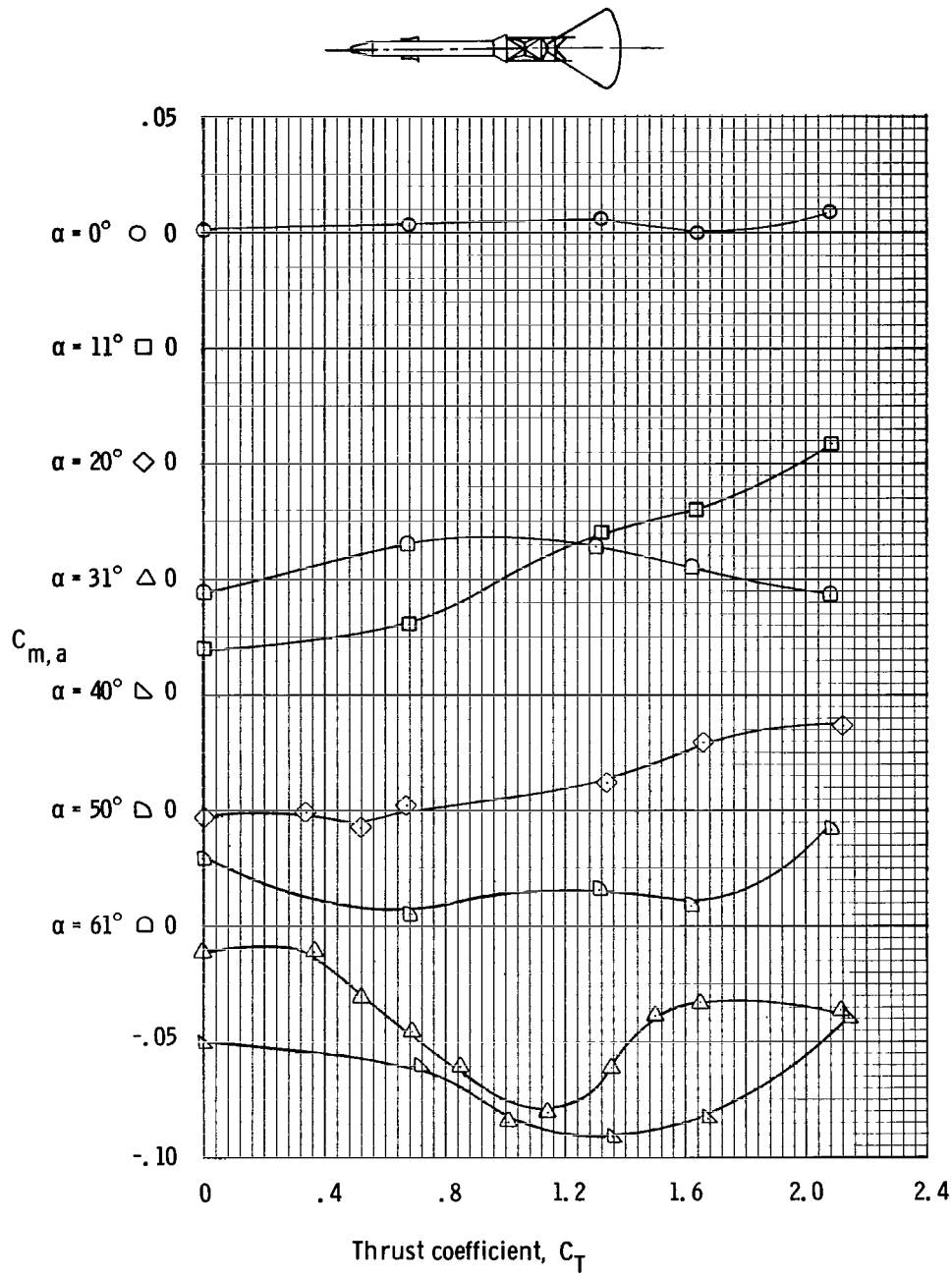

(g) Variation of pitching-moment coefficient with thrust coefficient at M = 0.9.

Figure 10. - Continued.

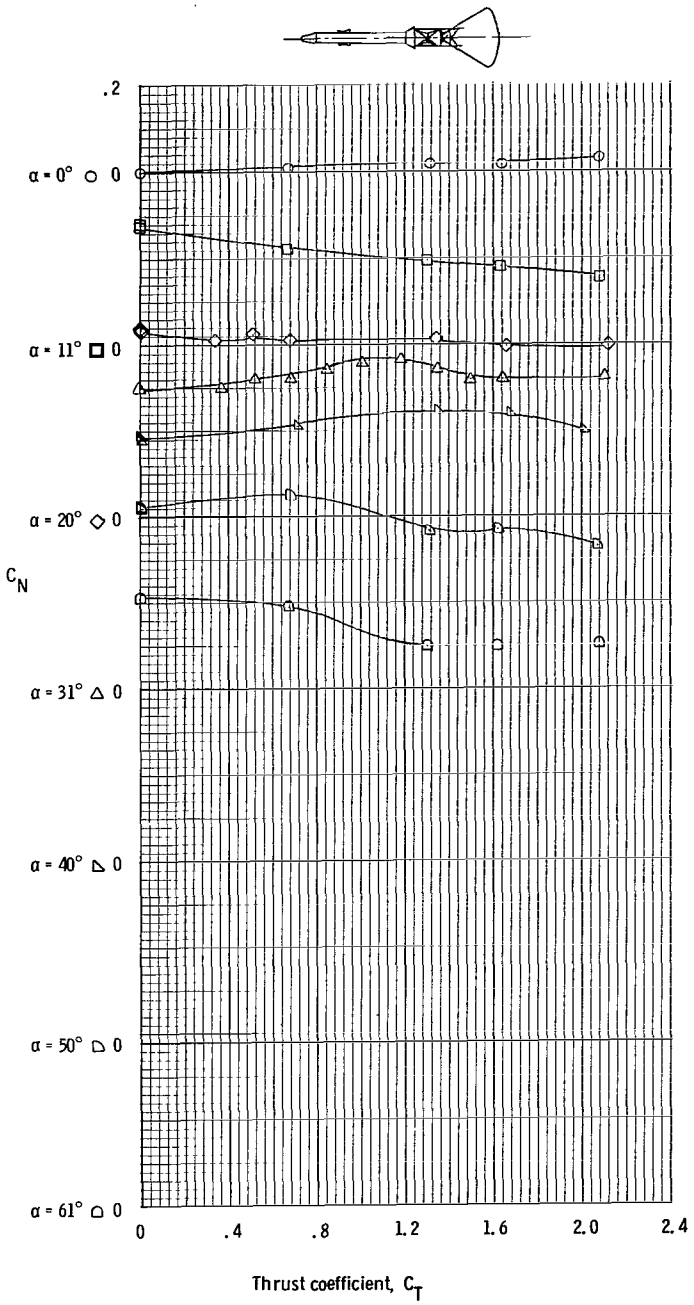

(h) Variation of normal-force coefficient with thrust coefficient at M = 0.9.

Figure 10. - Continued.

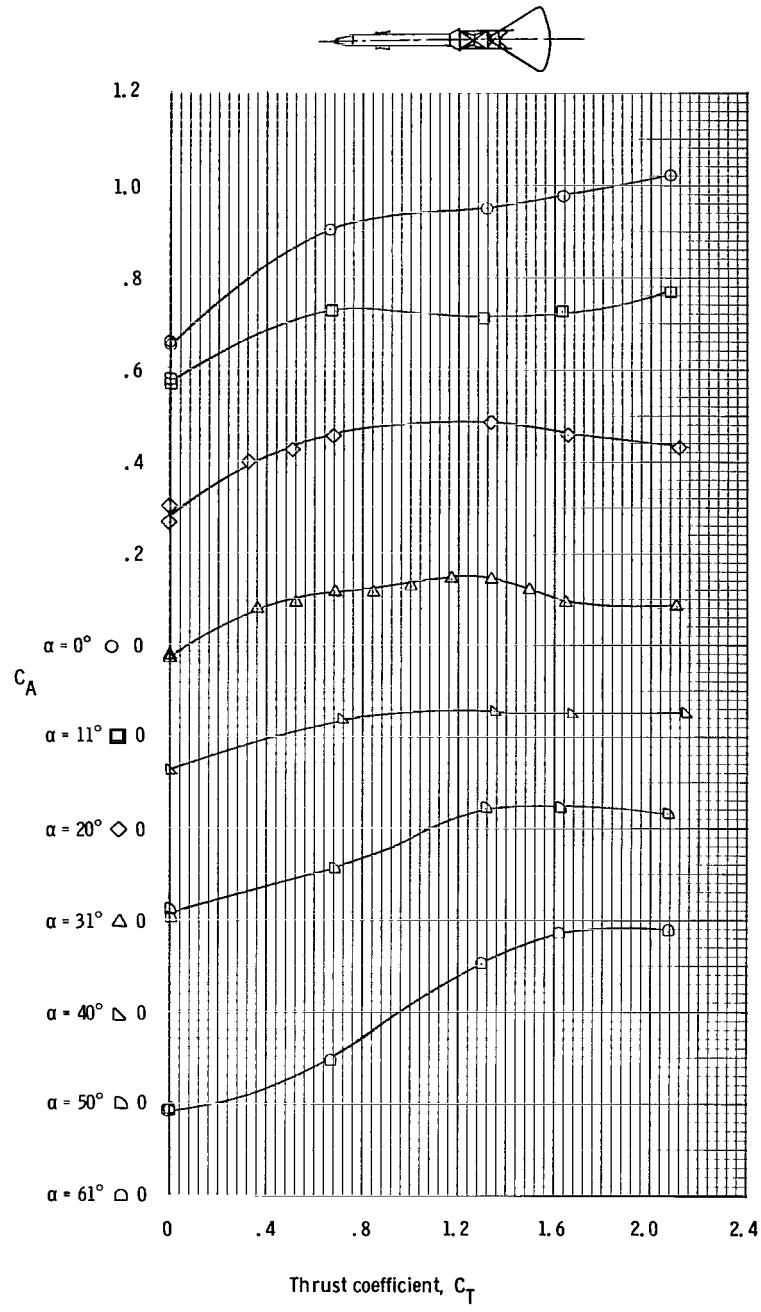

(i) Variation of axial-force coefficient with thrust coefficient at M = 0.9.

Figure 10. - Continued.

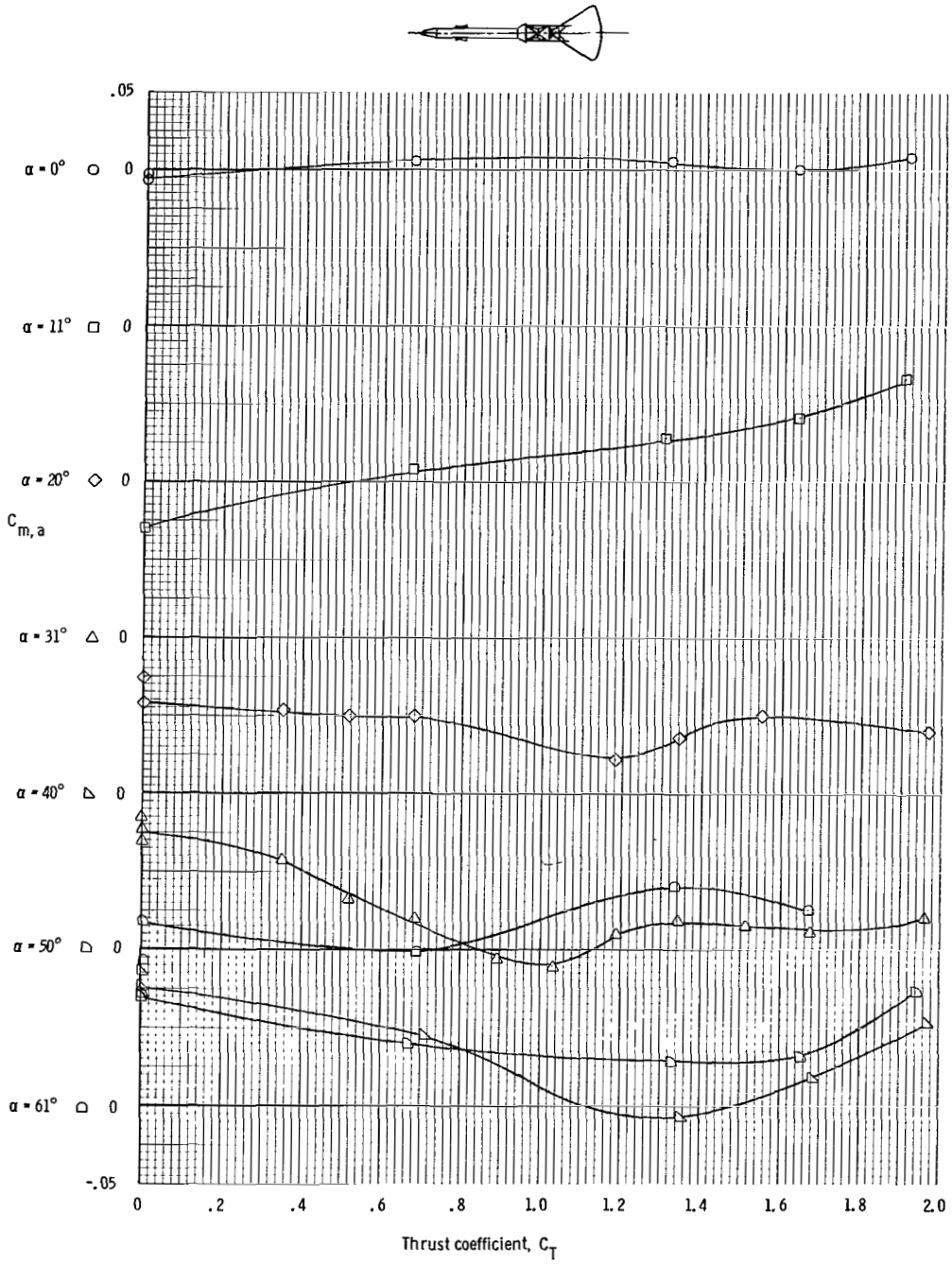

(j) Variation of pitching-moment coefficient with thrust coefficient at M = 1.0.

Figure 10. - Continued.

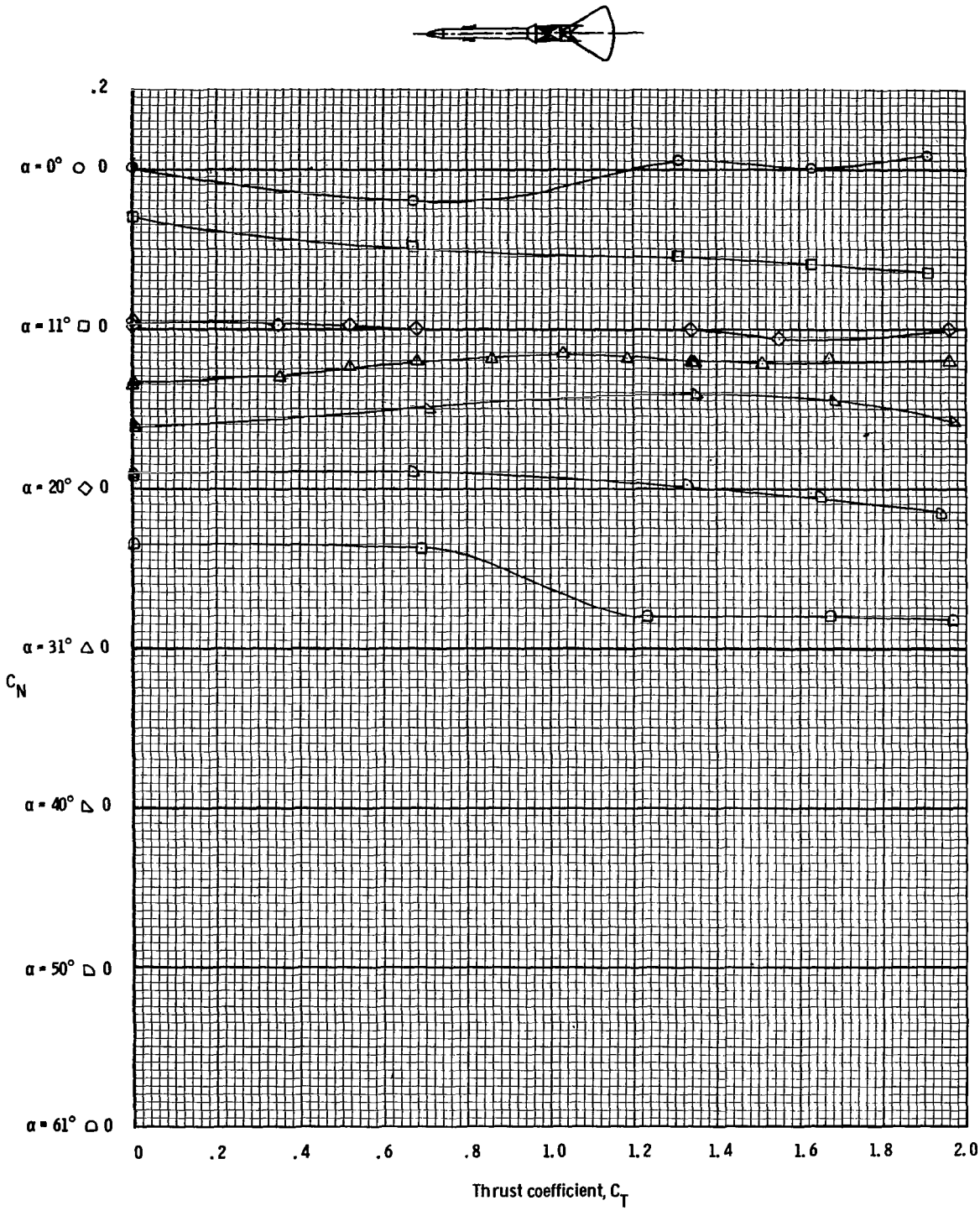

(k) Variation of normal-force coefficient with thrust coefficient at M = 1.0.

Figure 10. - Continued.

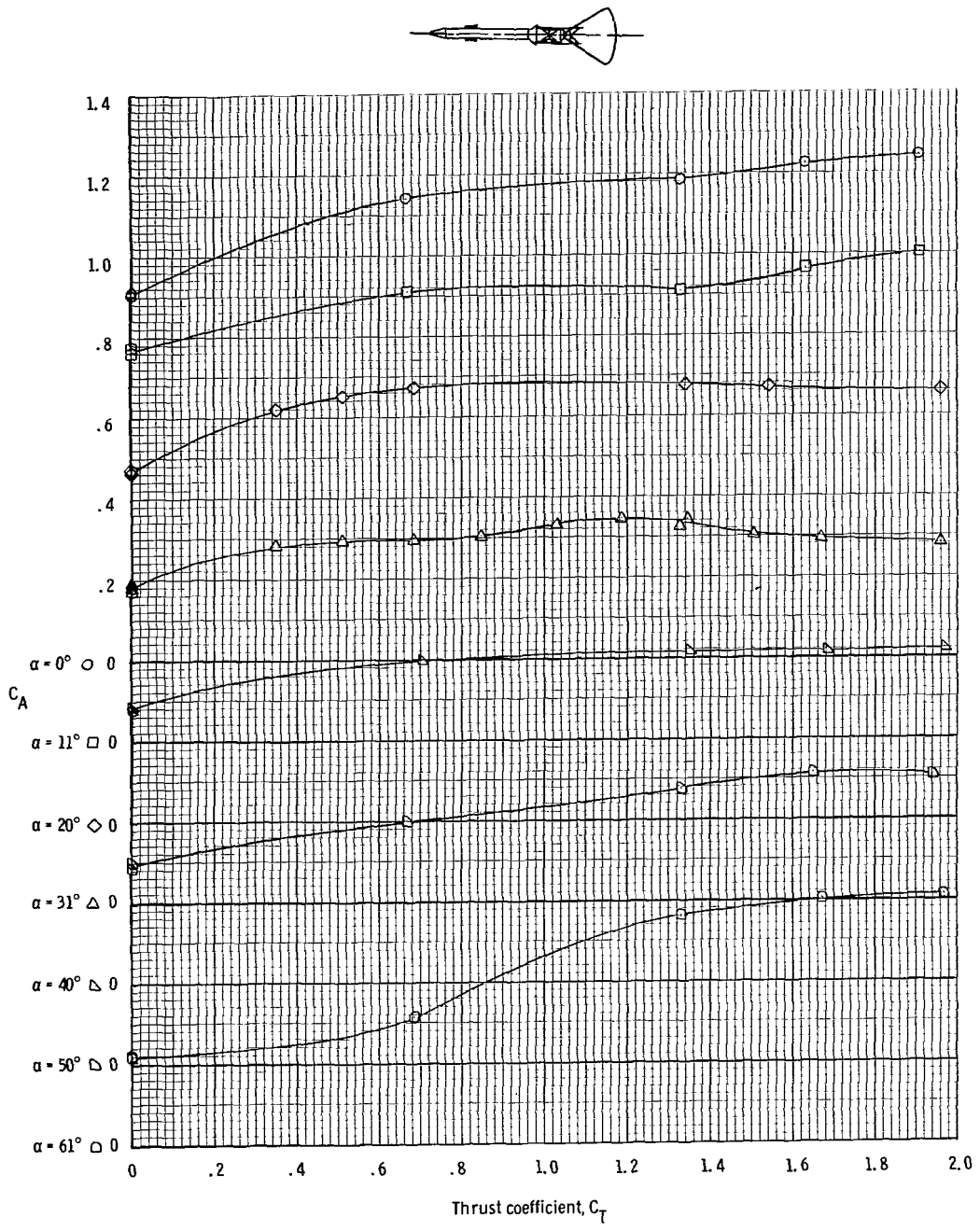

(l) Variation of axial-force coefficient with thrust coefficient at $M = 1.0$.

Figure 10. - Continued.

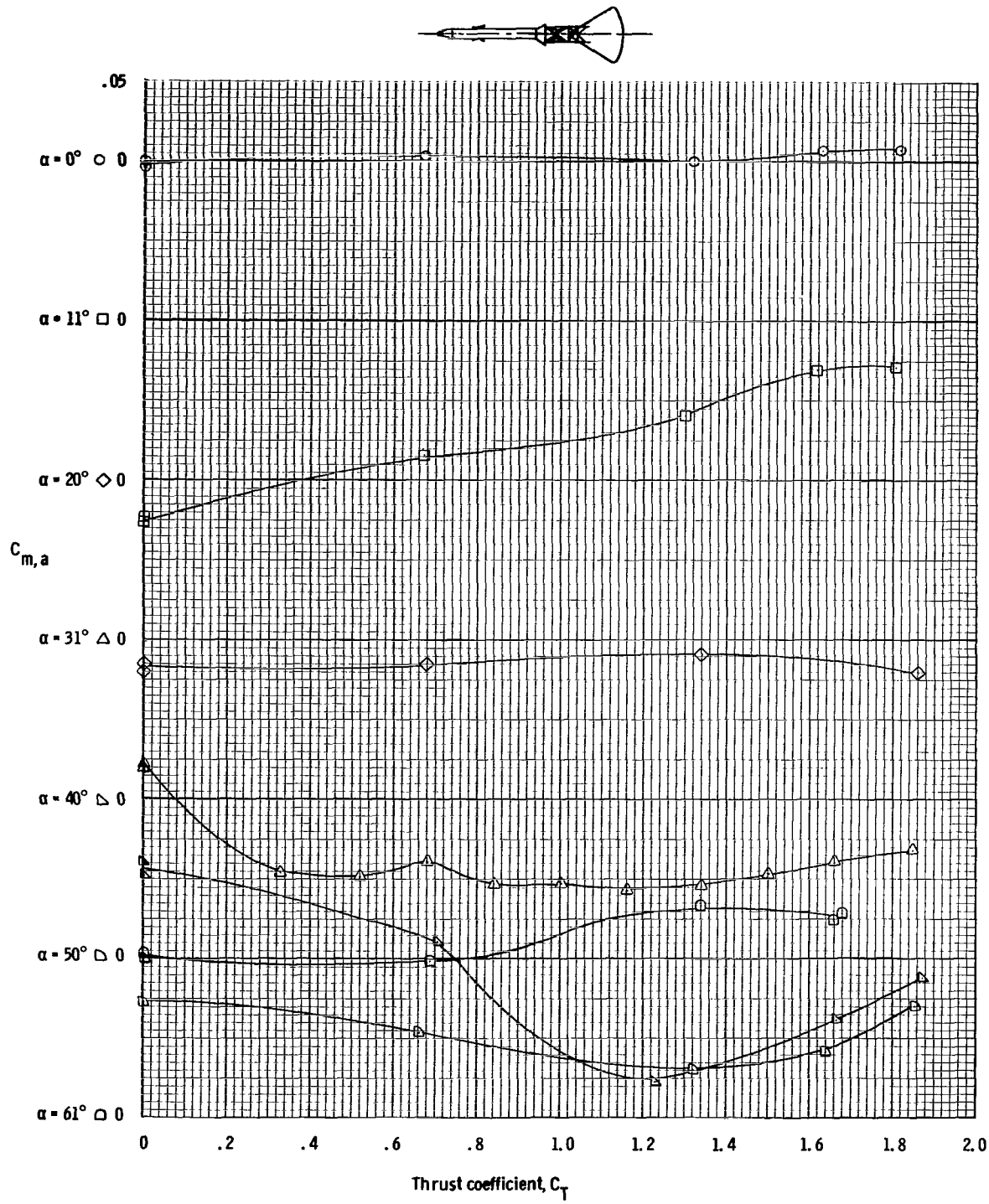

(m) Variation of pitching-moment coefficient with thrust coefficient at M = 1.1.

Figure 10. - Continued.

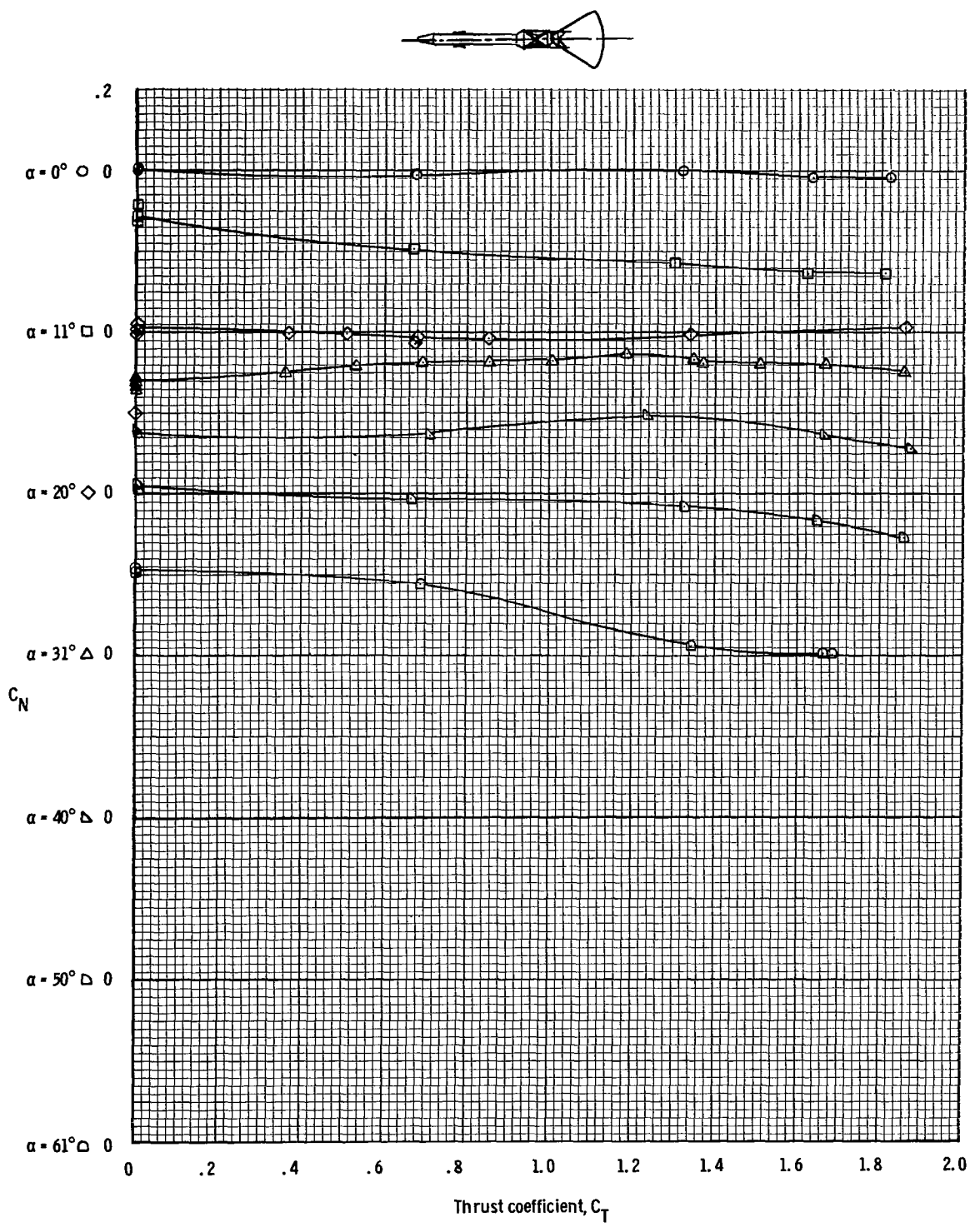

(n) Variation of normal-force coefficient with thrust coefficient at $M = 1.1$.

Figure 10. - Continued.

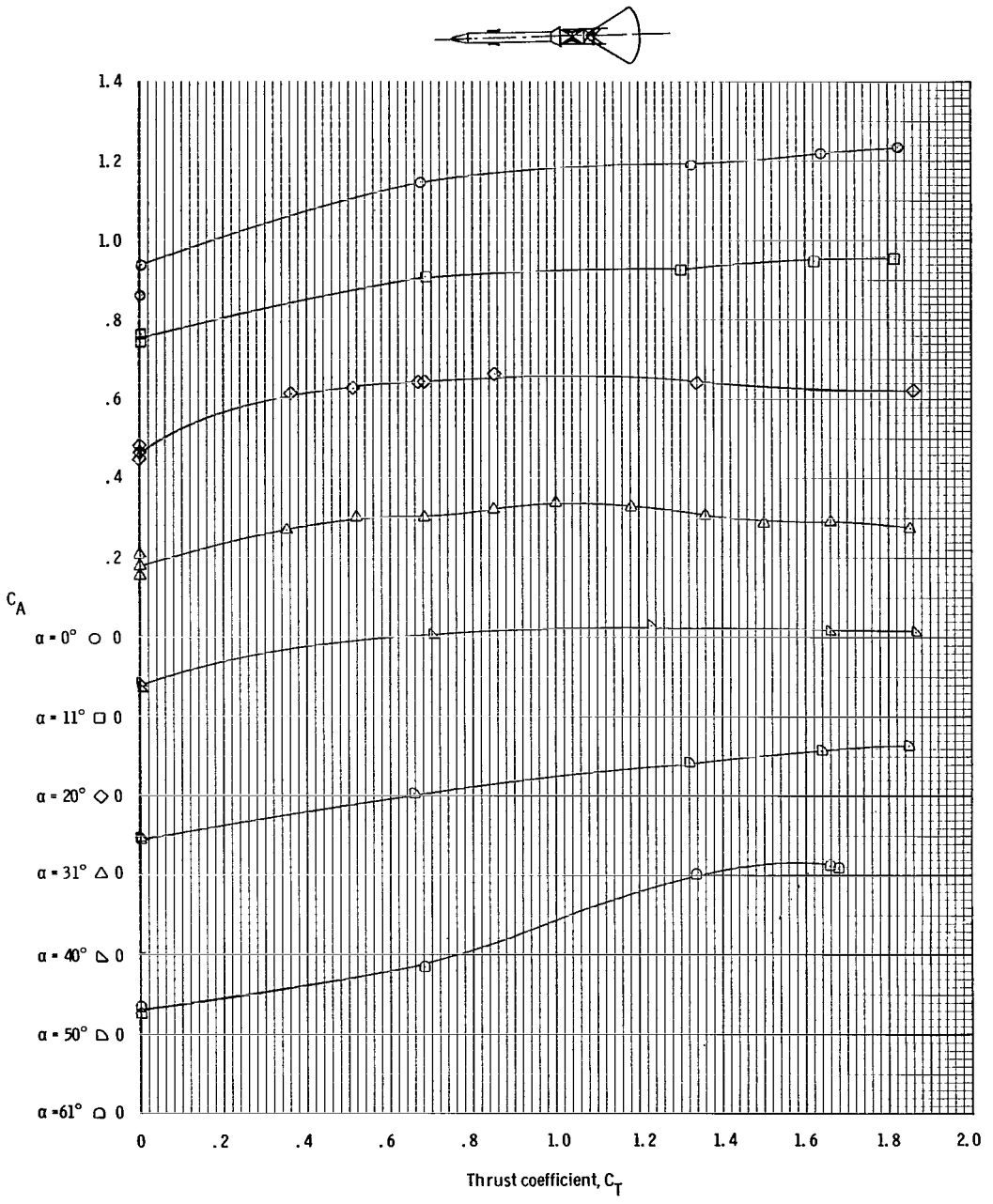

(o) Variation of axial-force coefficient with thrust coefficient at M = 1.1.

Figure 10. - Continued.

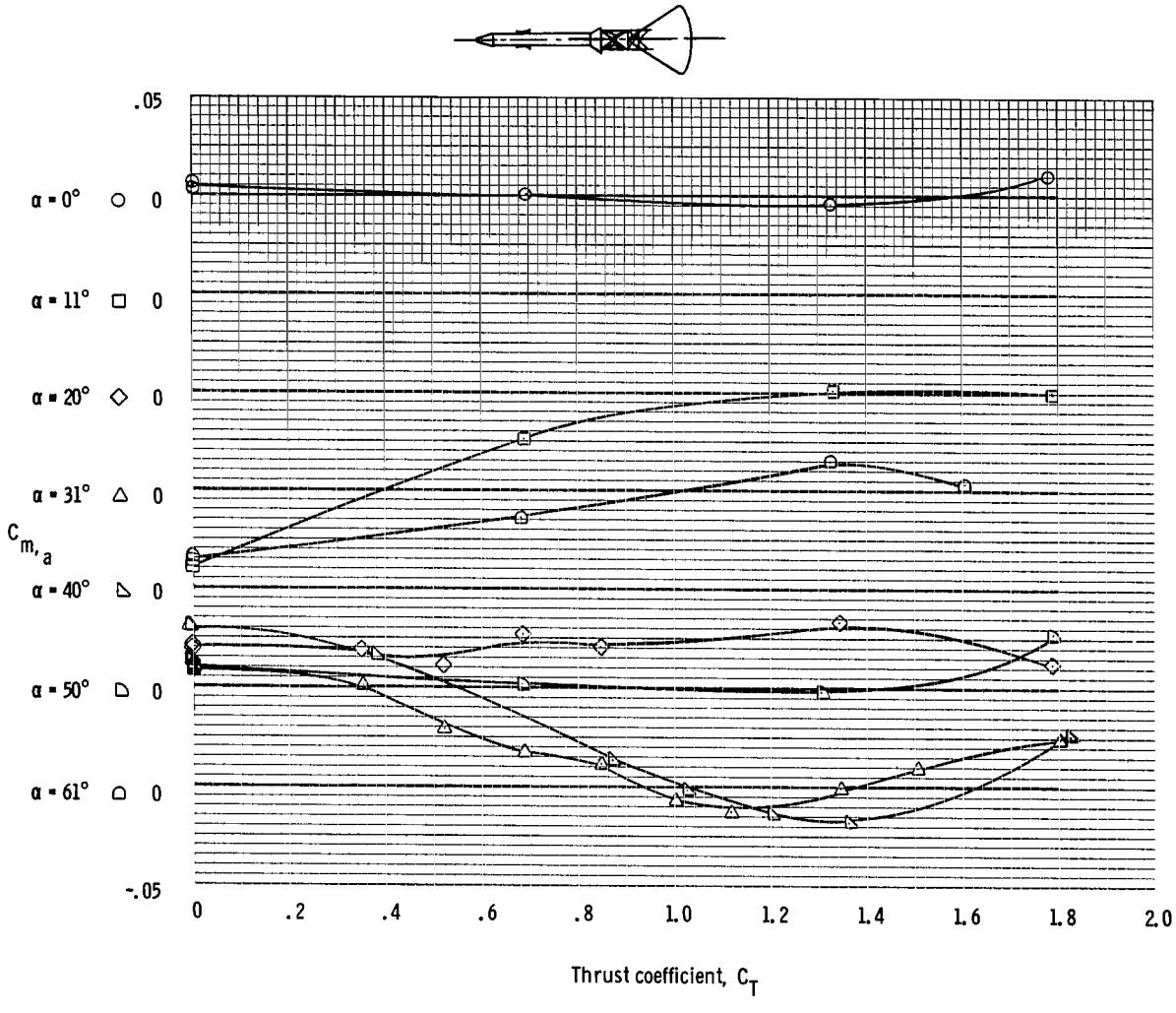

(p) Variation of pitching-moment coefficient with thrust coefficient at $M = 1.2$.

Figure 10. - Continued.

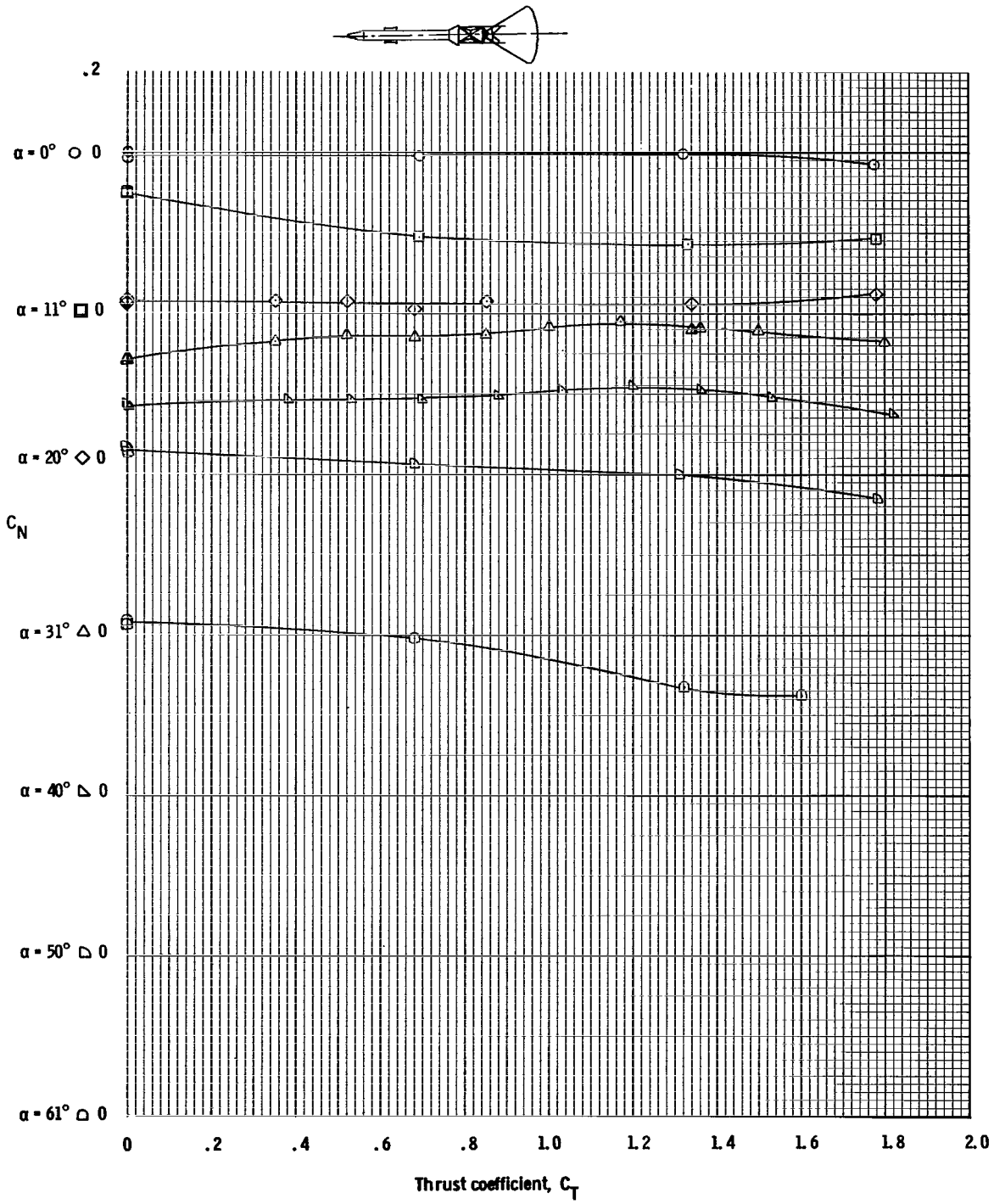

(q) Variation of normal-force coefficient with thrust coefficient at M = 1.2.

Figure 10. - Continued.

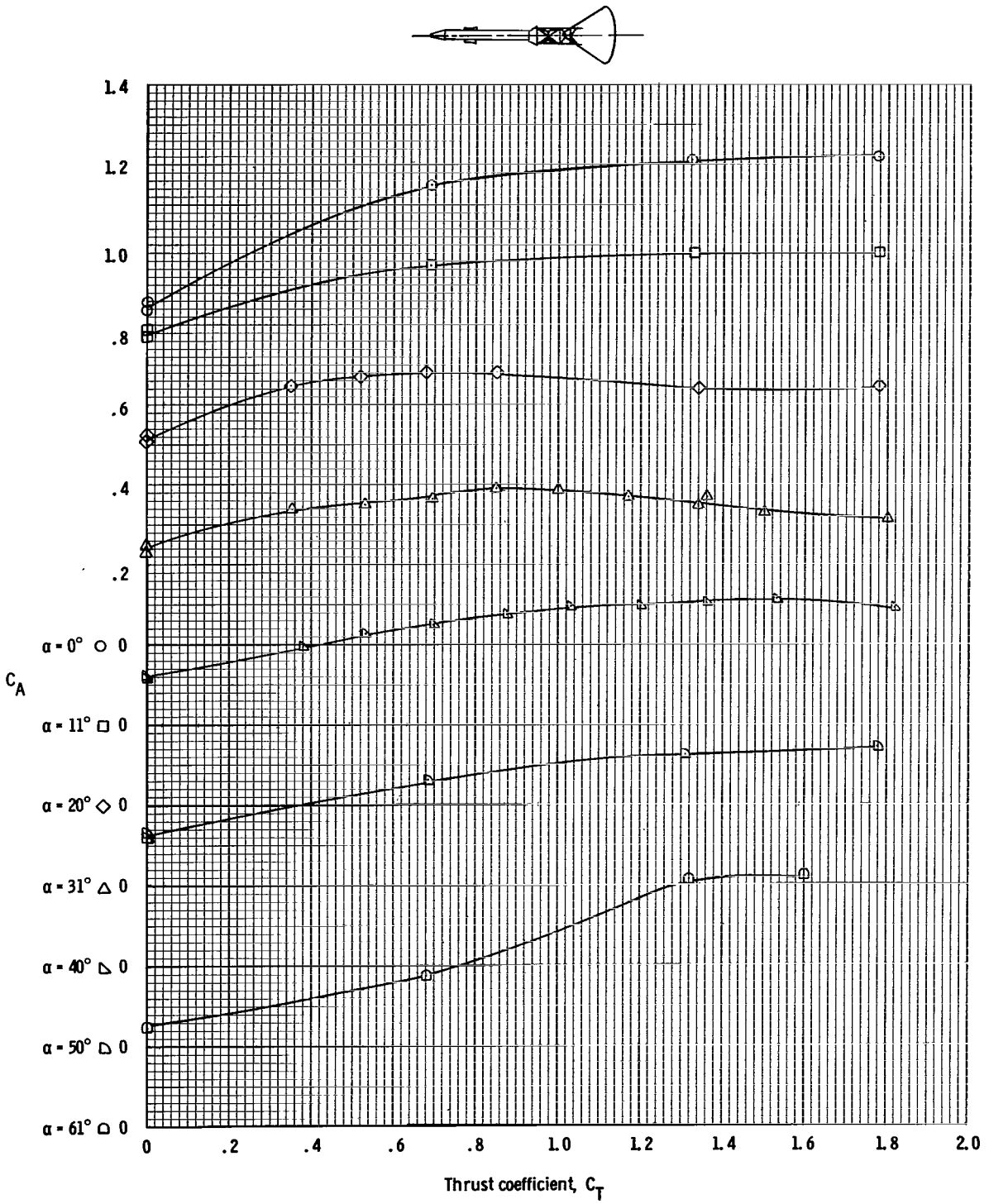

(r) Variation of axial-force coefficient with thrust coefficient at $M = 1.2$.

Figure 10. - Continued.

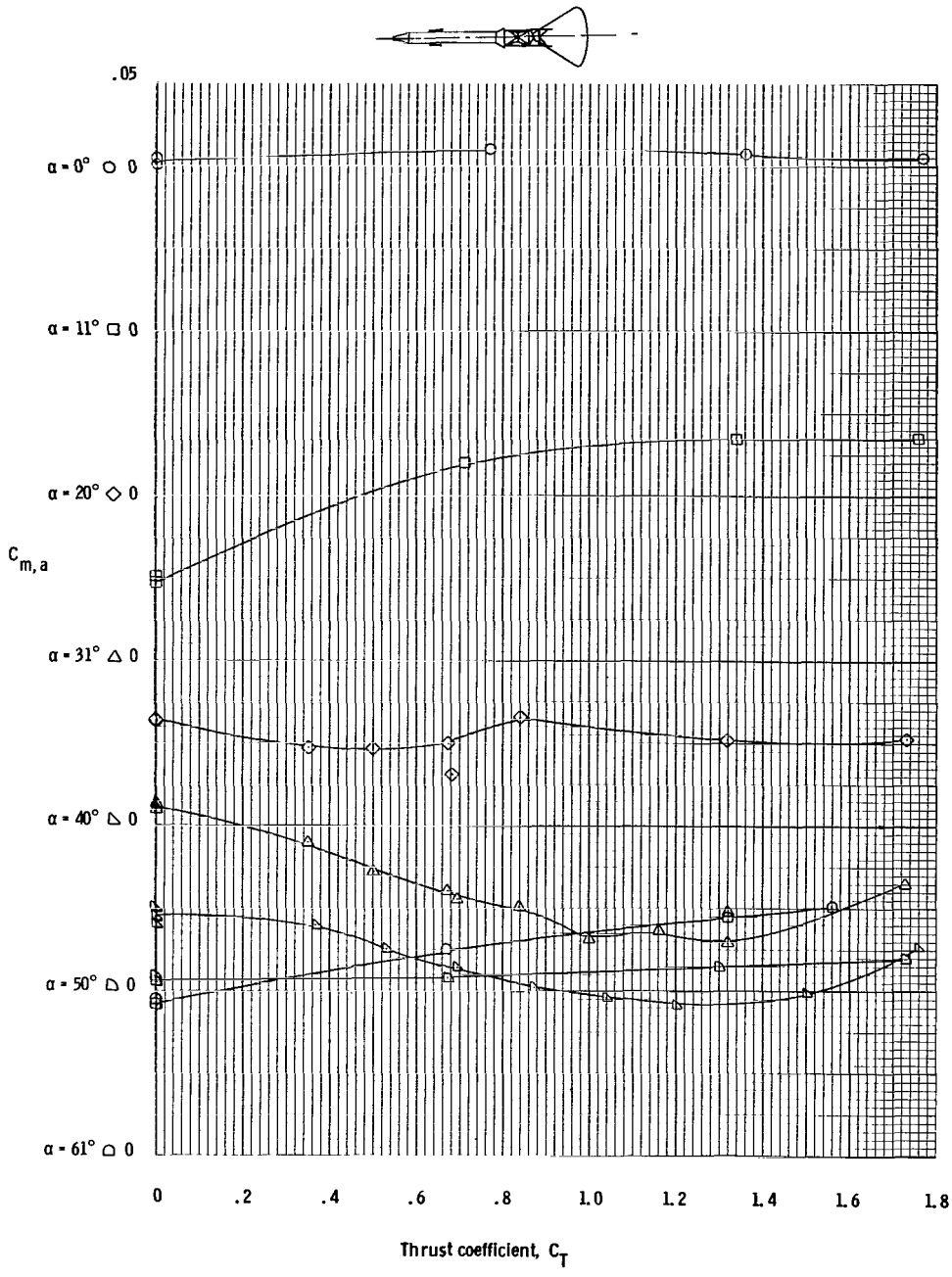

(s) Variation of pitching-moment coefficient with thrust coefficient at M = 1.3.

Figure 10. - Continued.

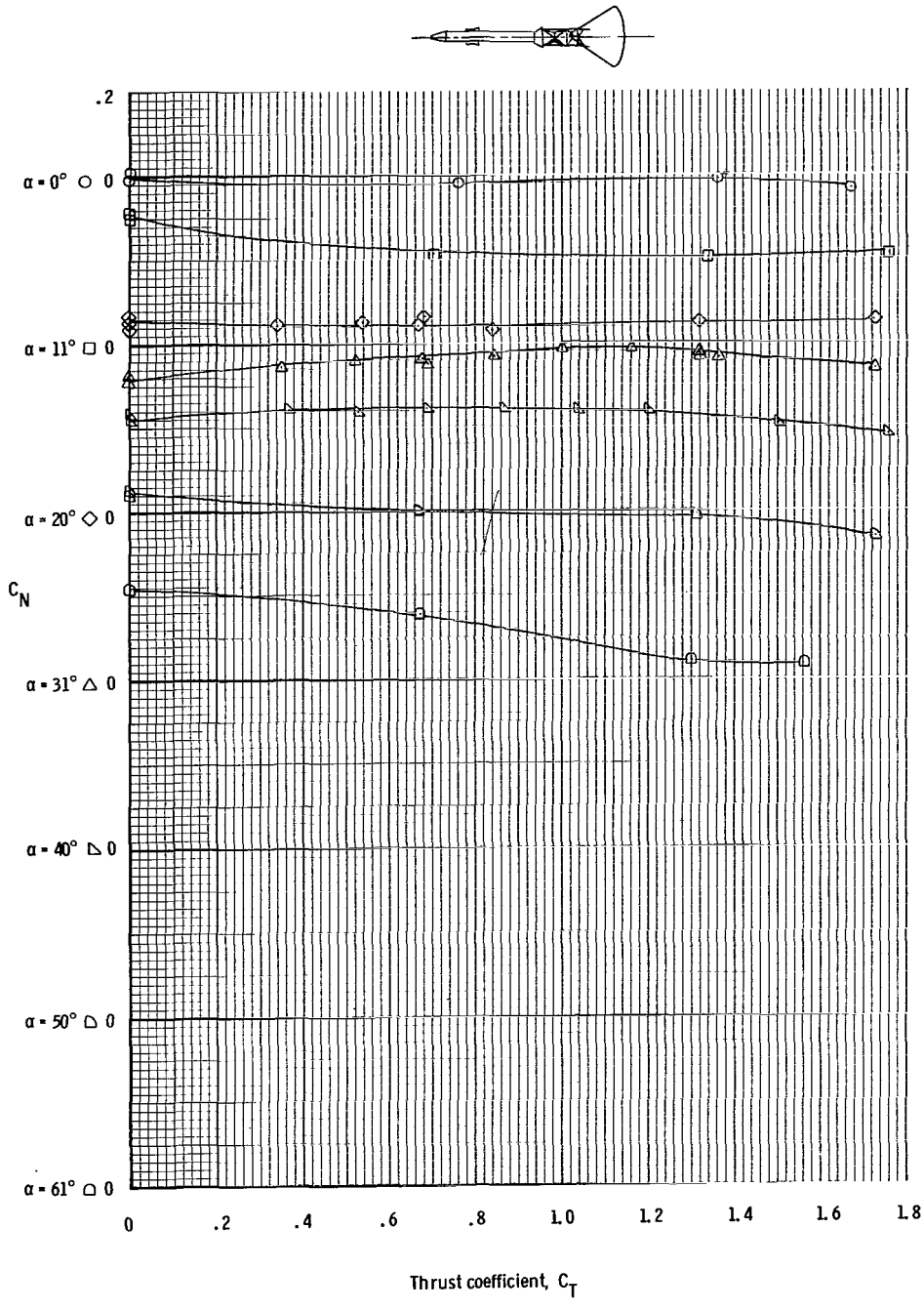

(t) Variation of normal-force coefficient with thrust coefficient at M = 1.3.

Figure 10. - Continued.

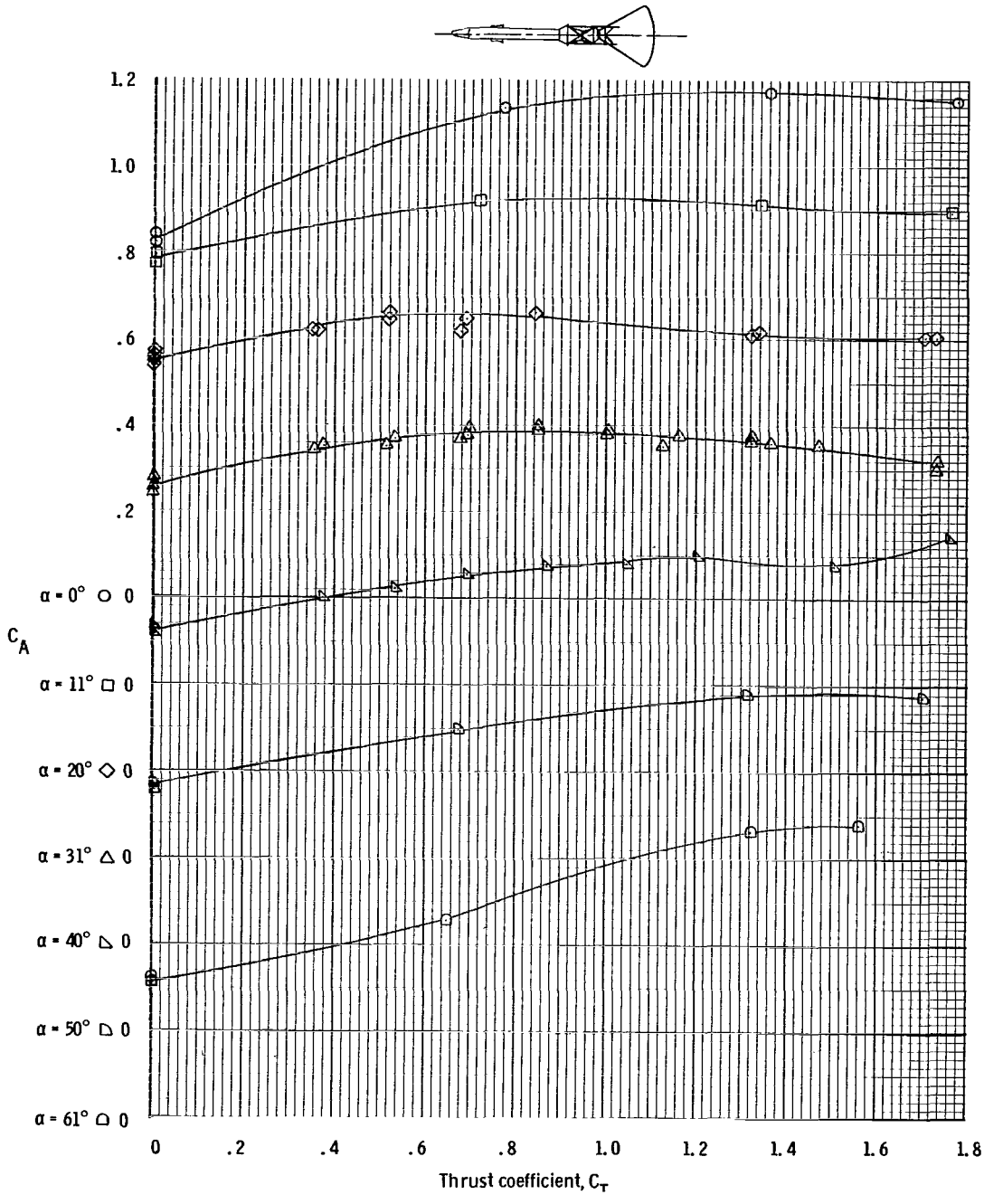

(u) Variation of axial-force coefficient with thrust coefficient at $M = 1.3$.

Figure 10. - Concluded.

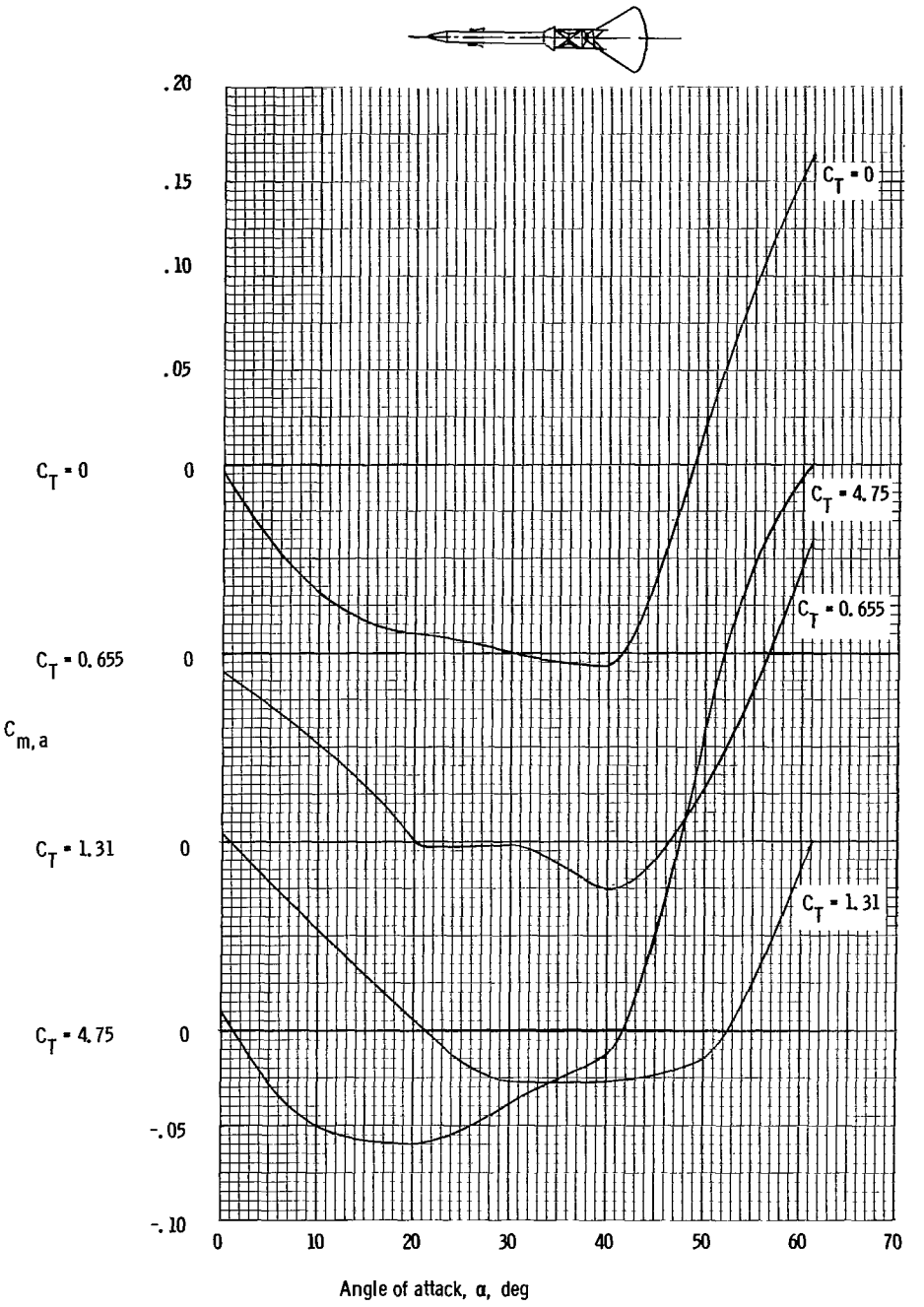

(a) $C_{m,a}$, $M = 0.5$.

Figure 11. - Variation of aerodynamic characteristics with angle of attack for the Apollo launch escape vehicle as determined at the Langley 16-Foot Tunnel.

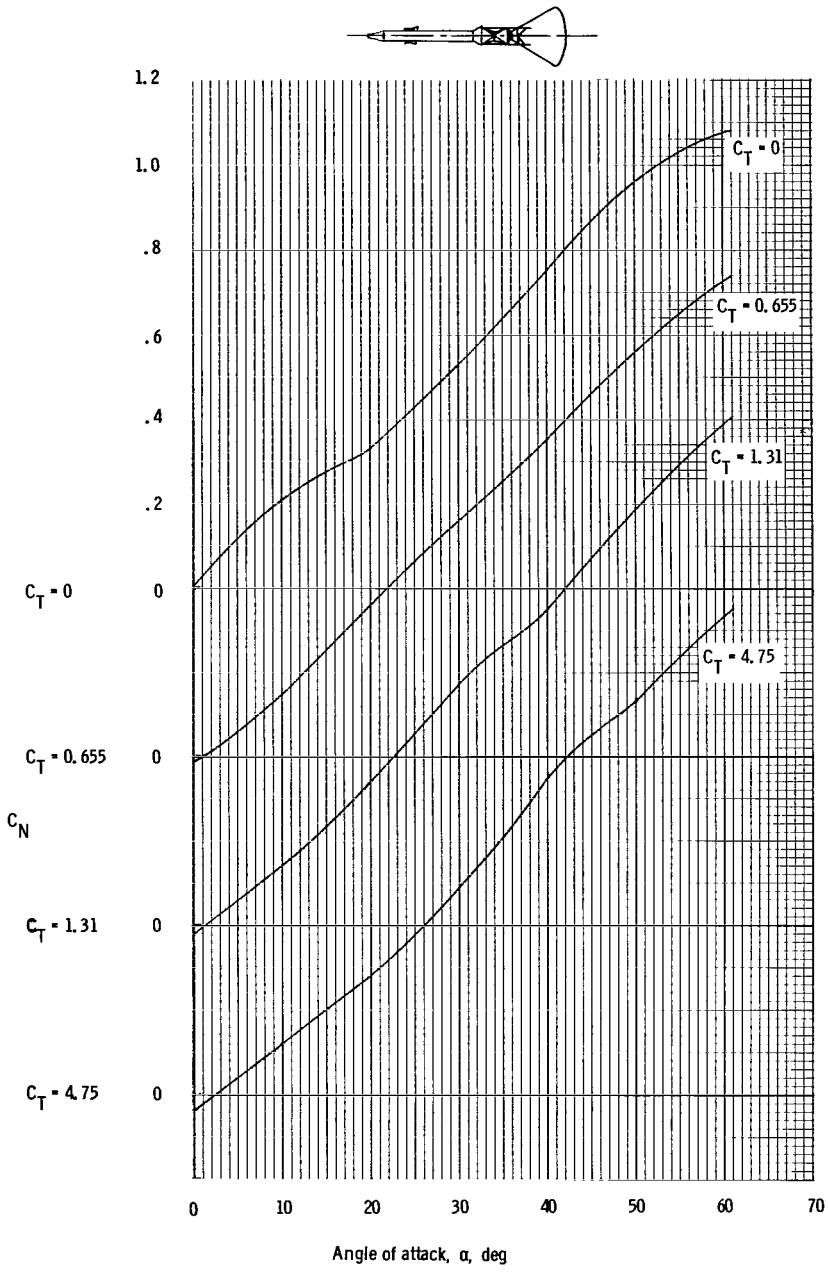

(b) C_N, M = 0.5.

Figure 11. - Continued.

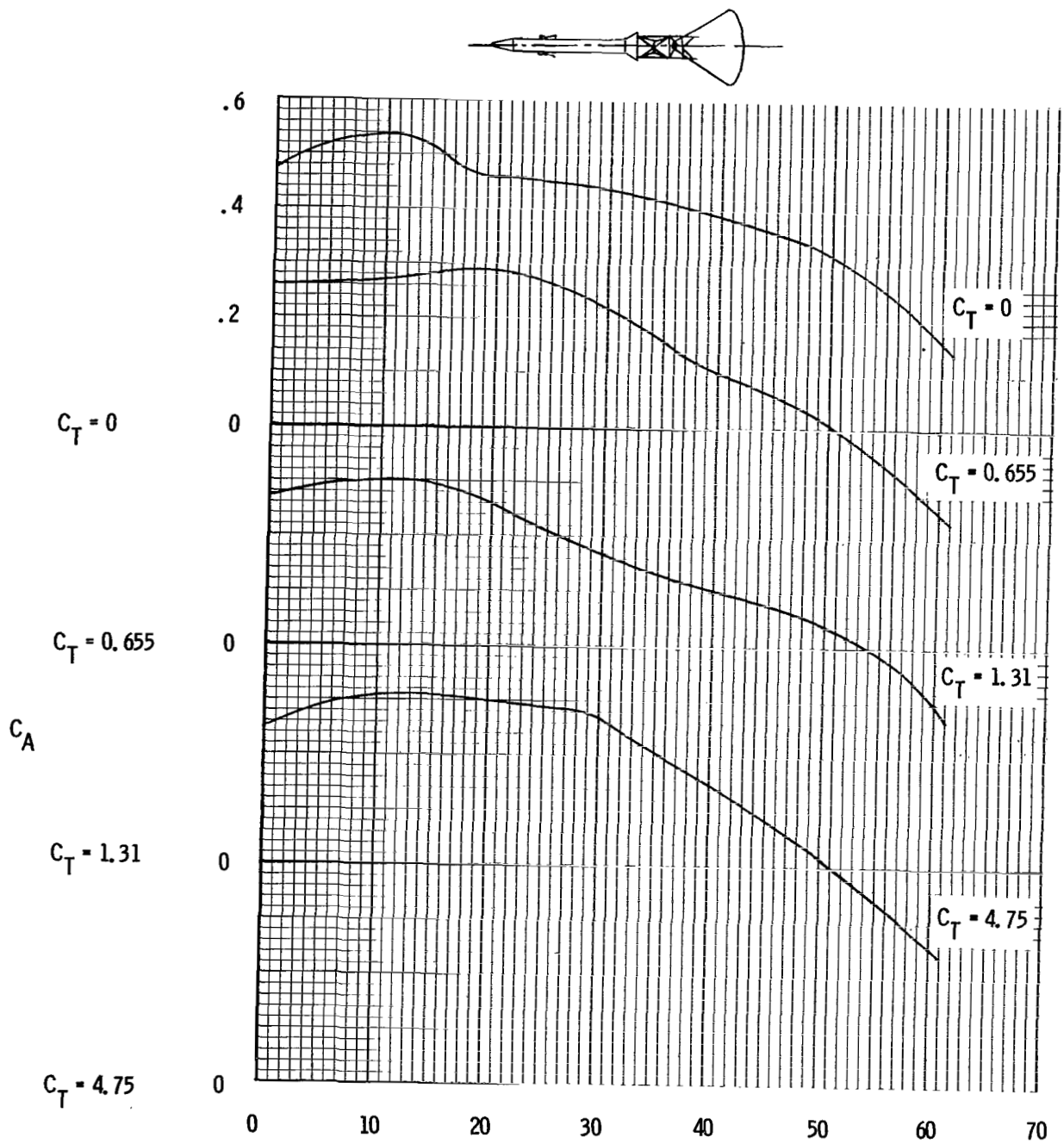

(c) C_A, $M \approx 0.5$.

Figure 11. - Continued.

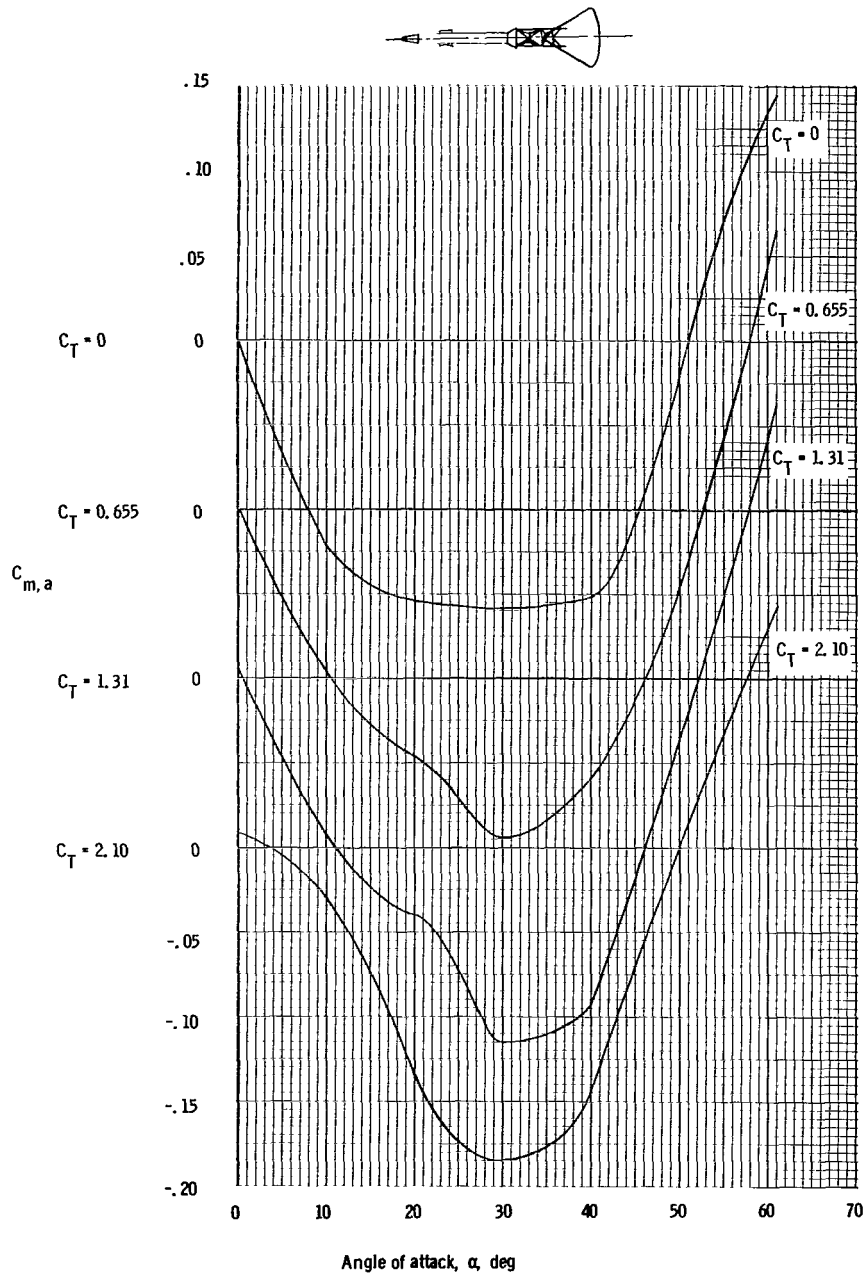

(d) $C_{m,a}$, $M = 0.9$.

Figure 11. - Continued.

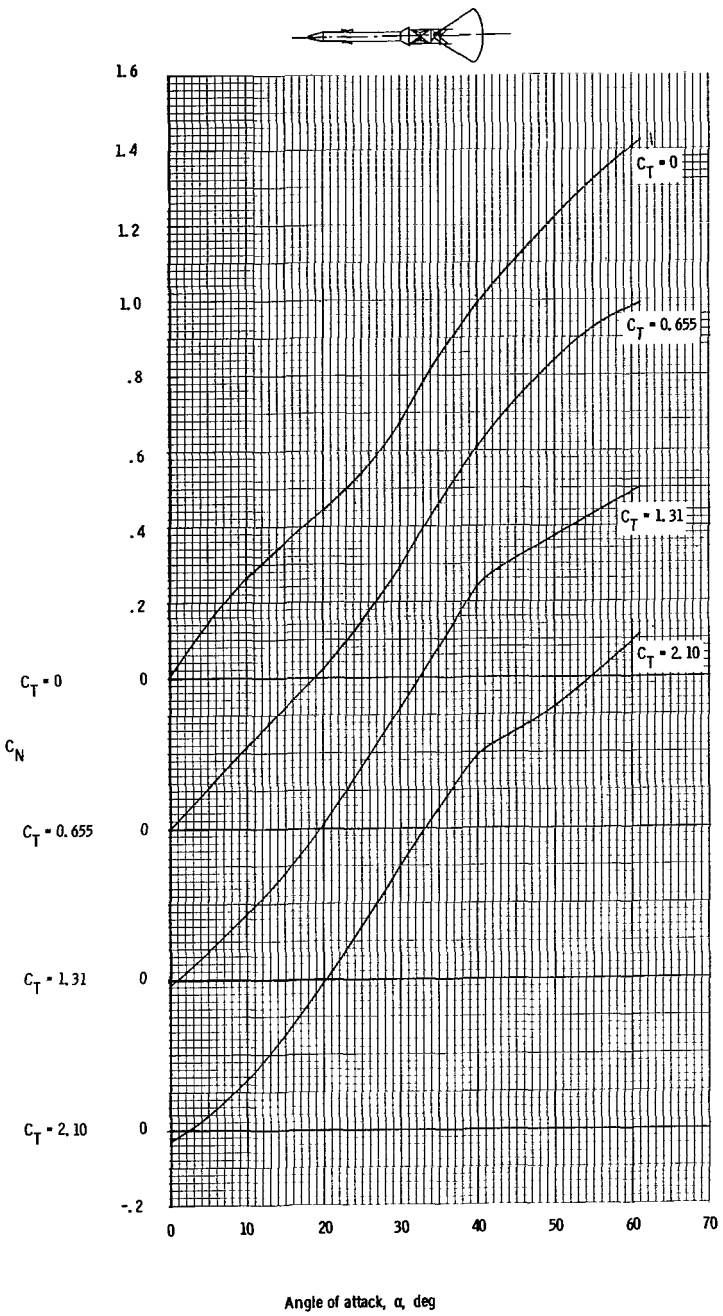

(e) C_N, $M = 0.9$.

Figure 11. - Continued.

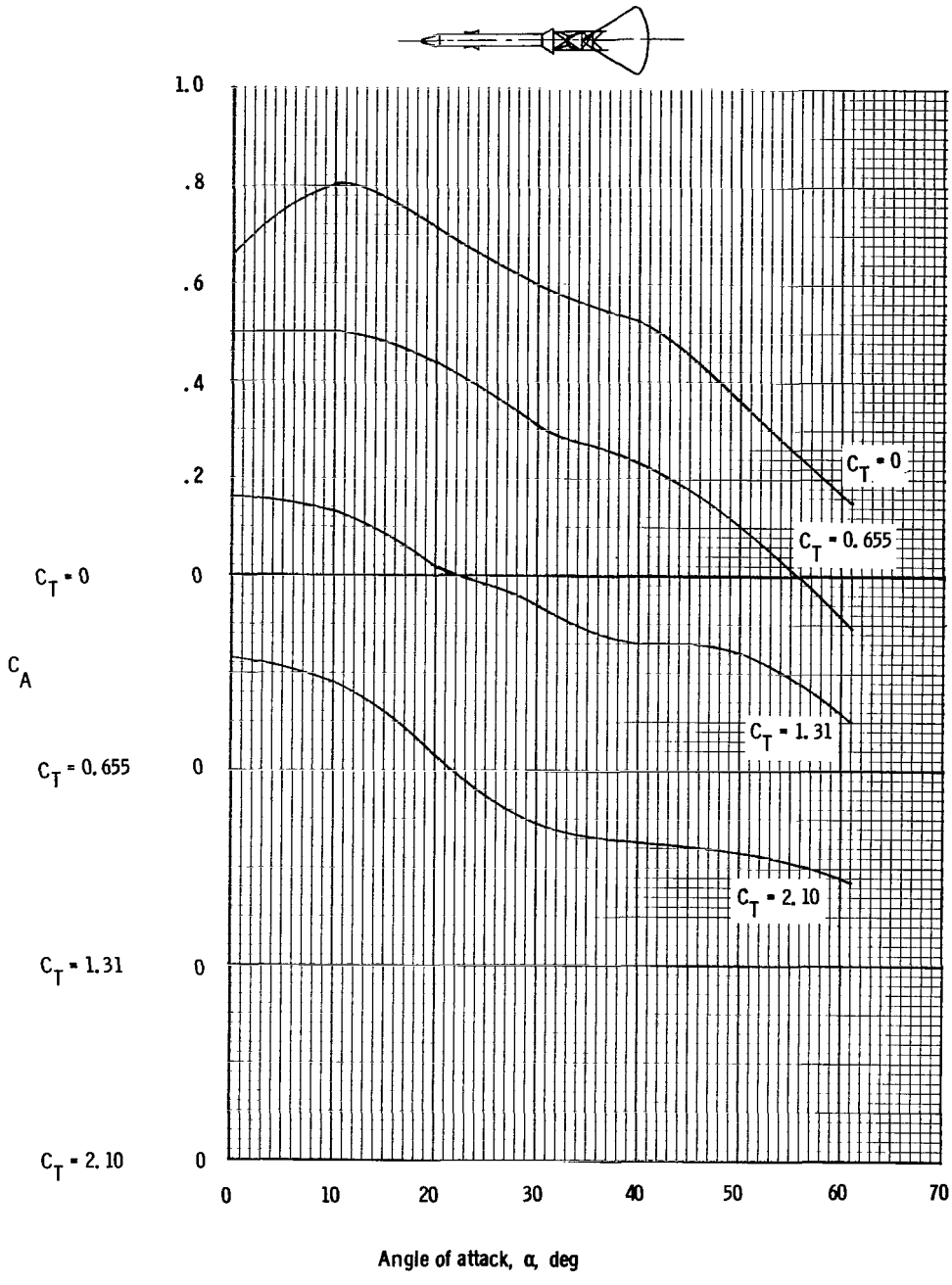

(f) C_A, $M = 0.9$.

Figure 11. - Continued.

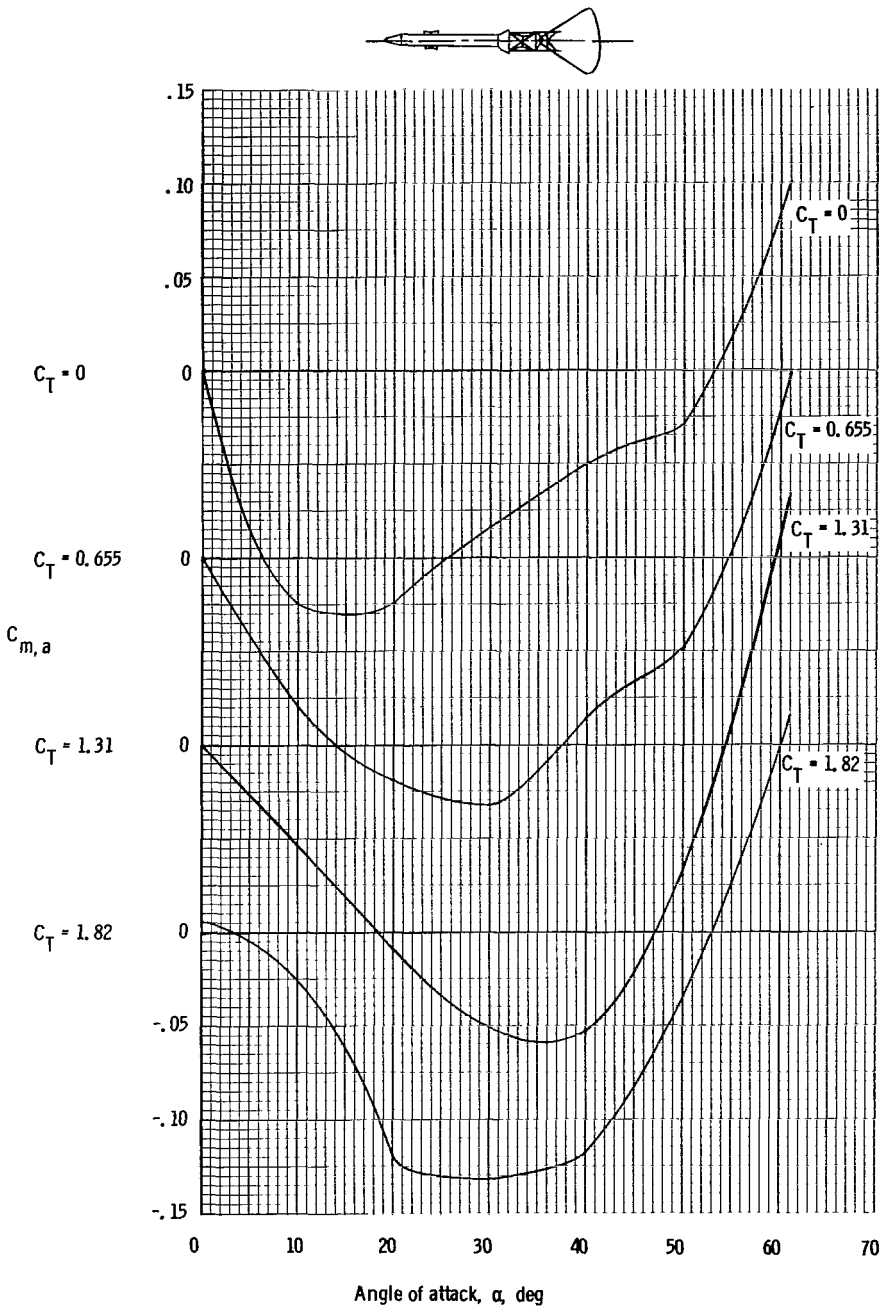

(g) $C_{m,a}$, M = 1.1.

Figure 11. - Continued.

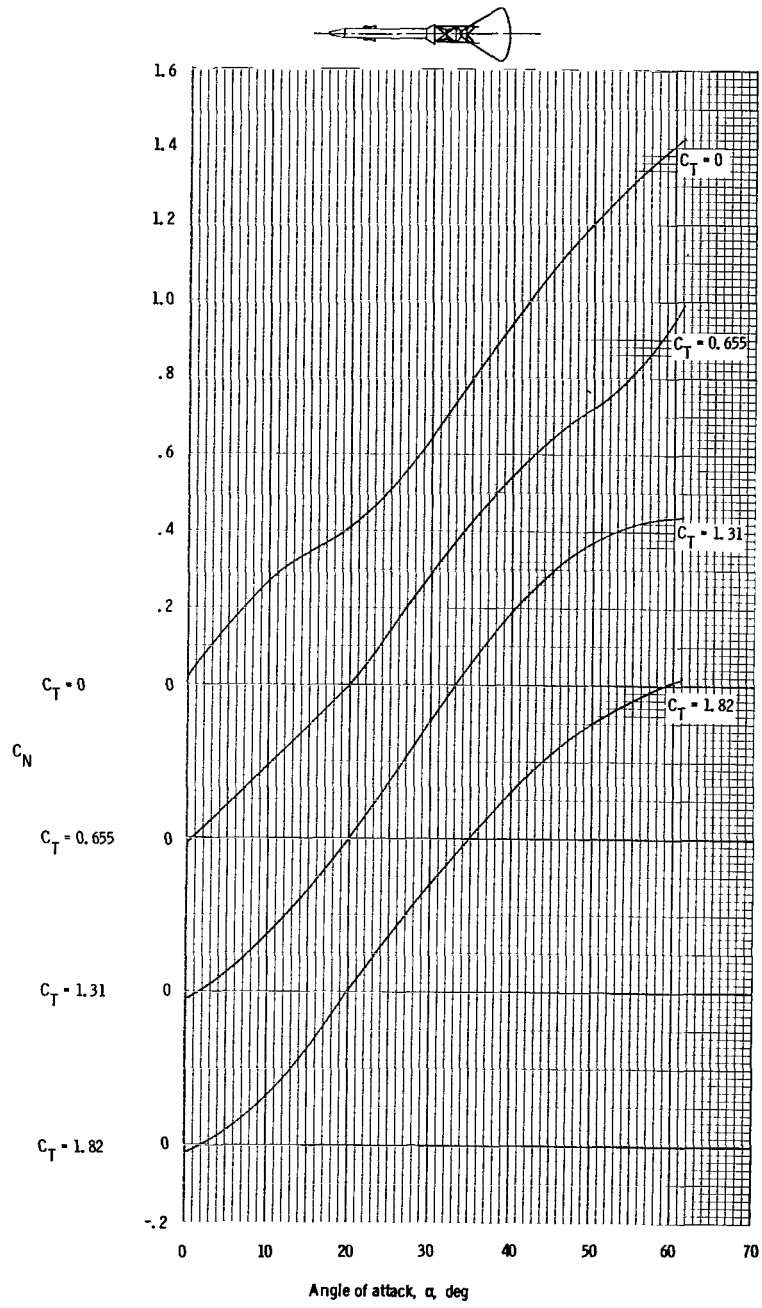

(h) C_N, M = 1.1.

Figure 11. - Continued.

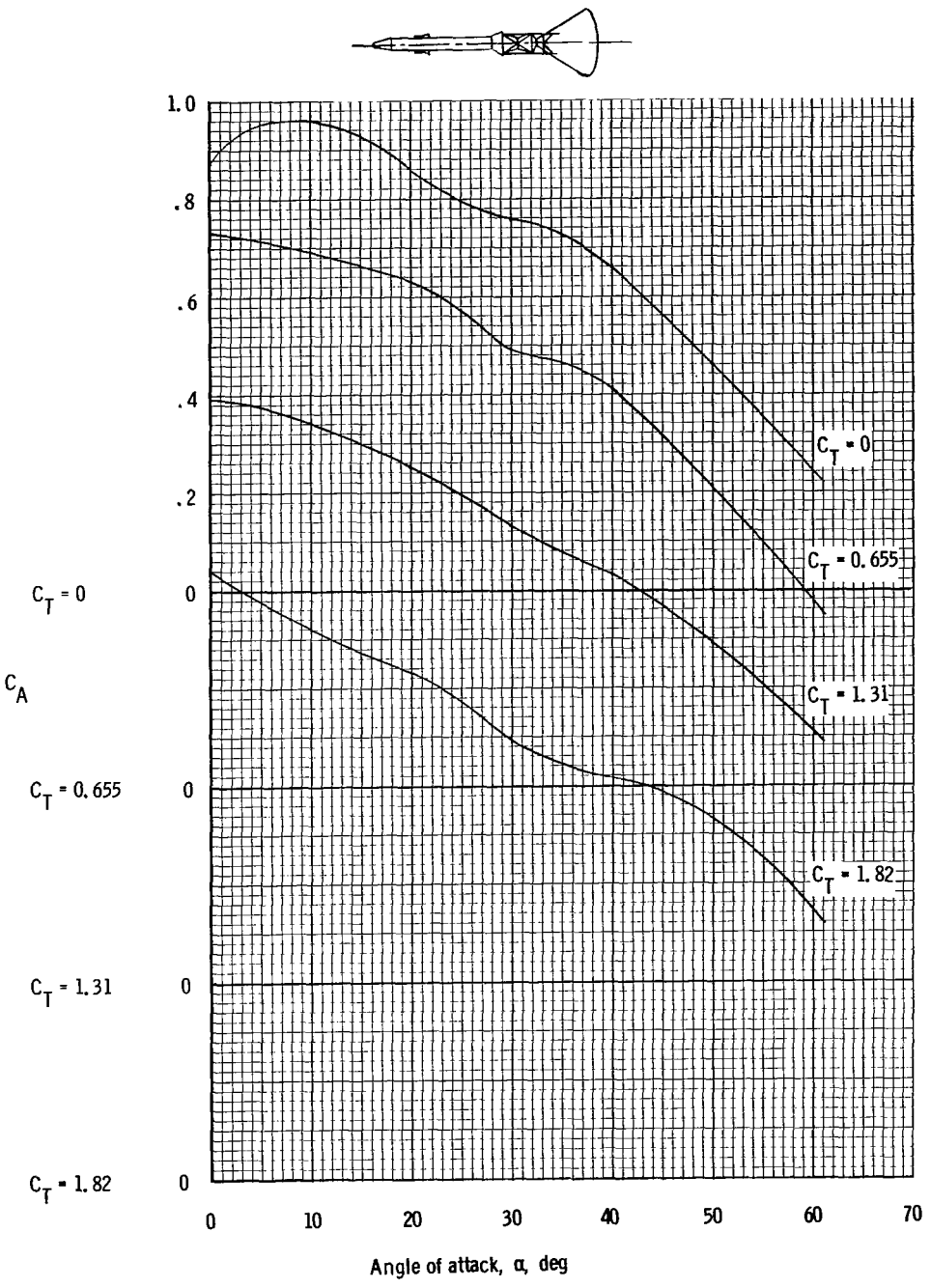

(i) C_A, $M = 1.1$.

Figure 11. - Continued.

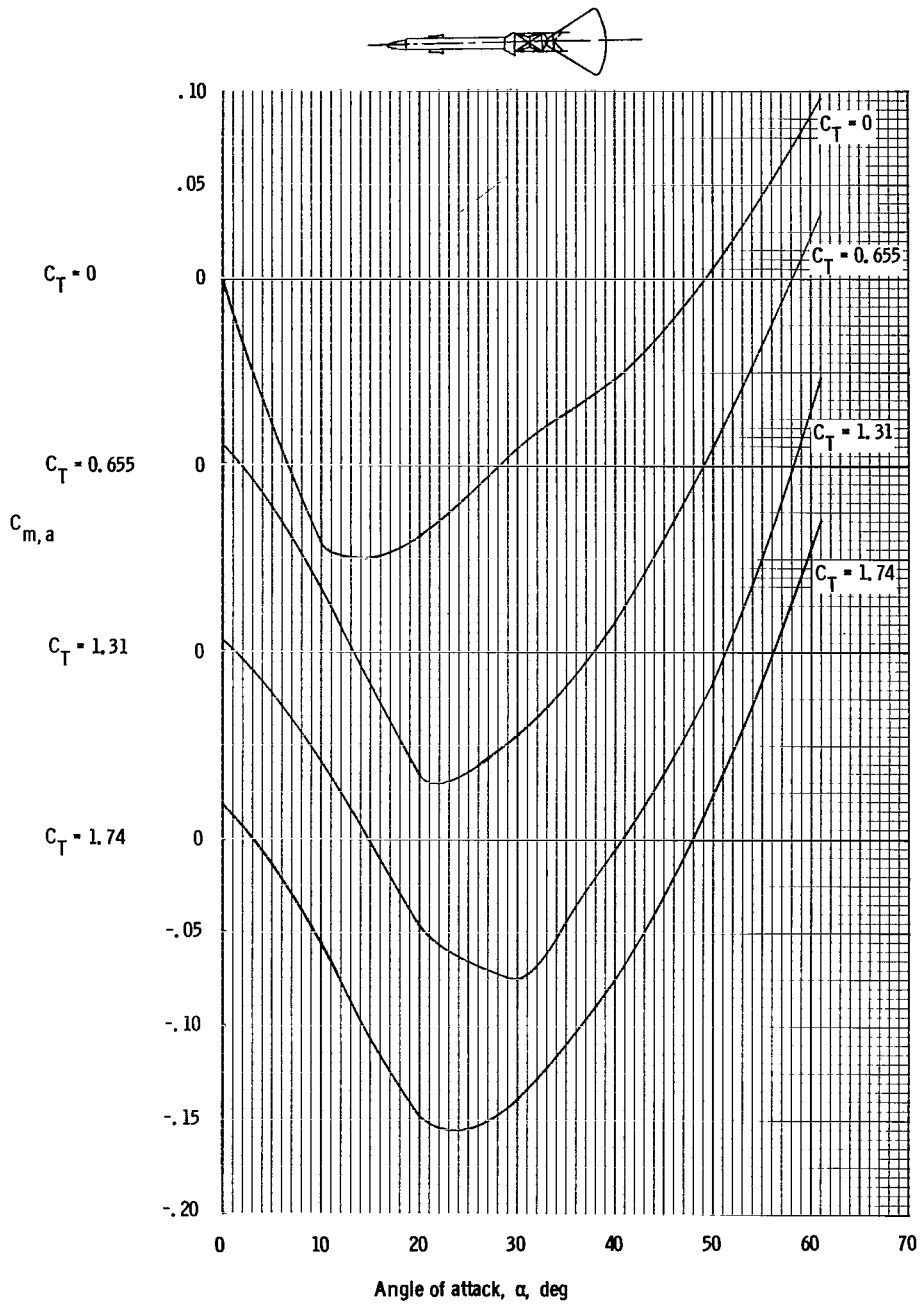

(j) $C_{m,a}$, $M = 1.3$.

Figure 11. - Continued.

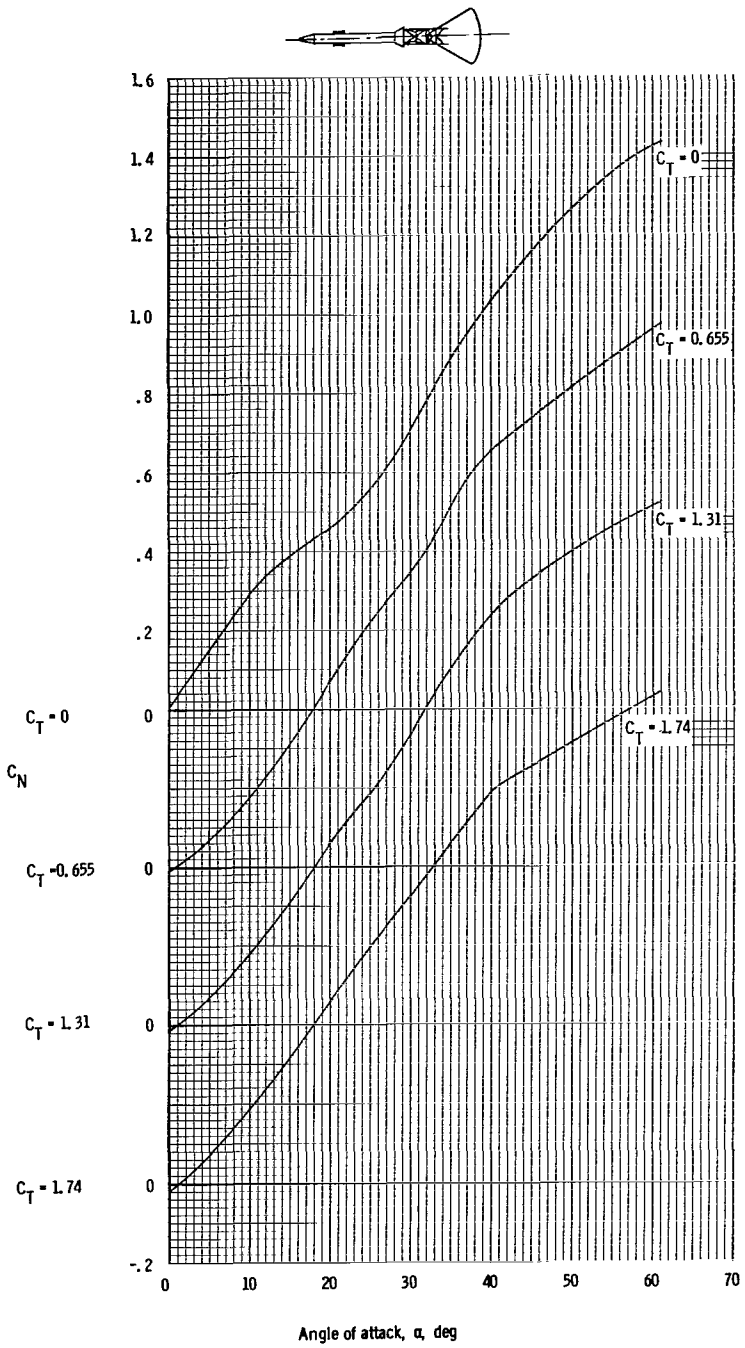

(k) C_N, M = 1.3.

Figure 11. - Continued.

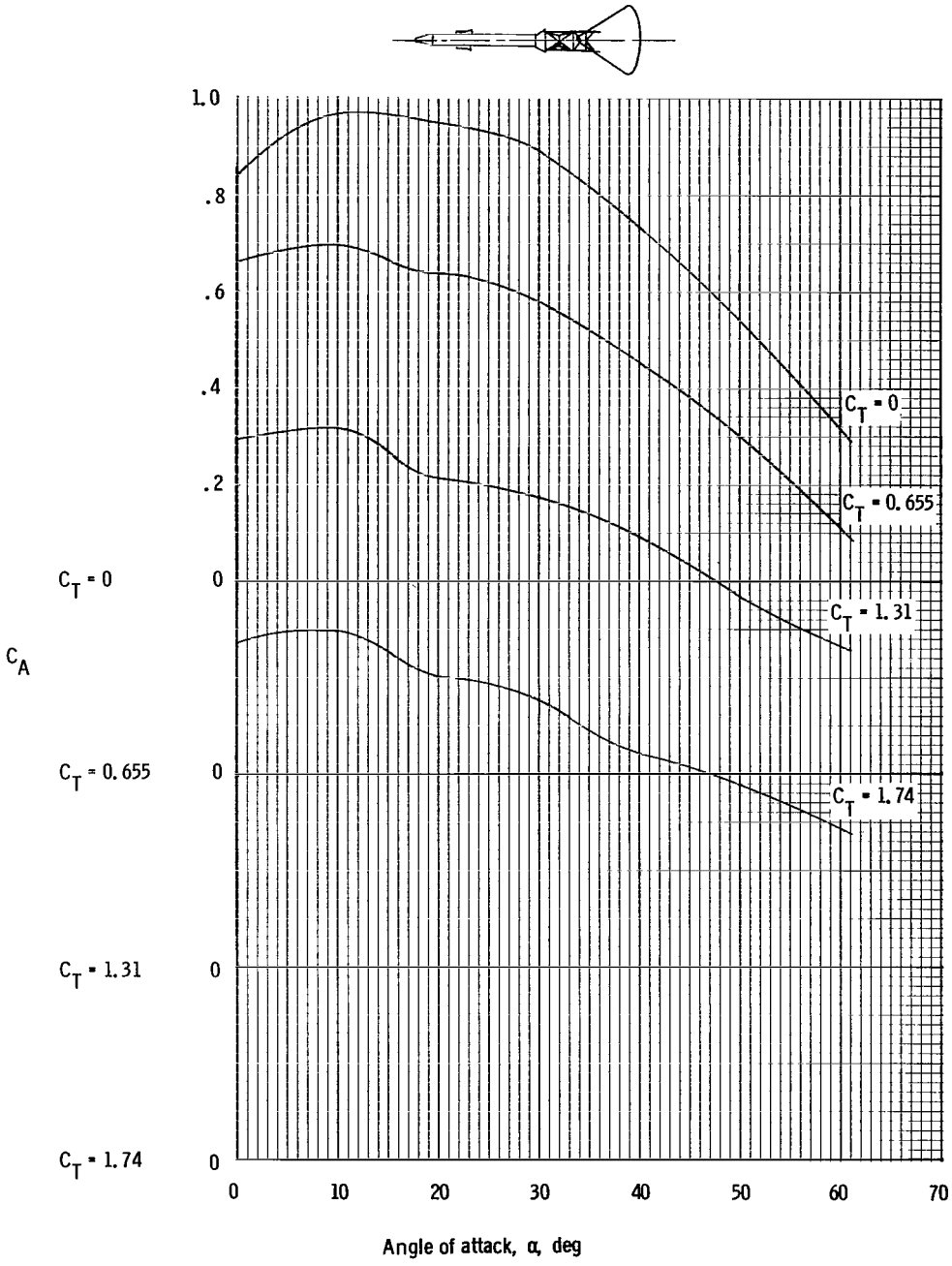

(l) C_A, M = 1.3.

Figure 11. - Concluded.

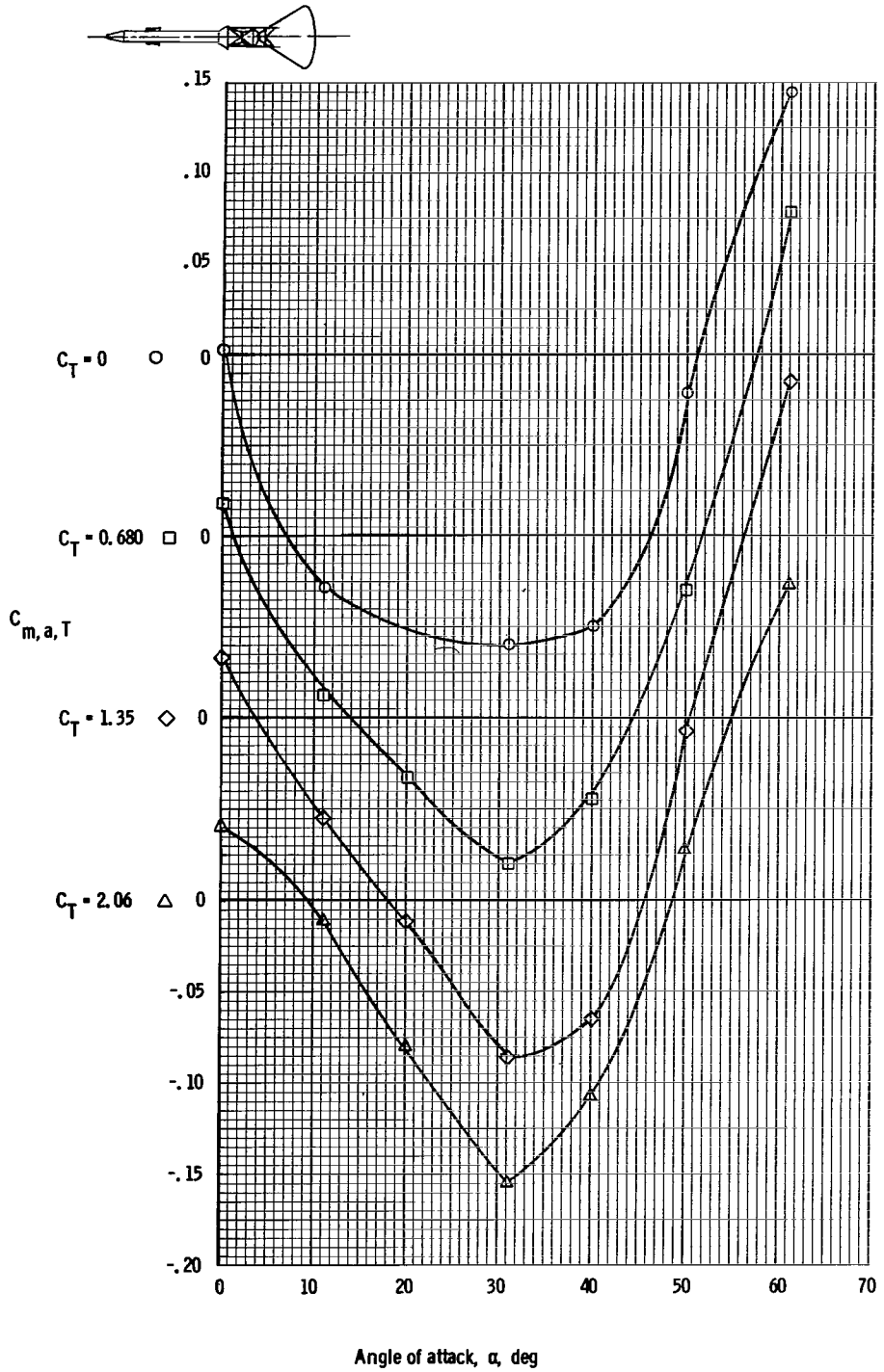

(a) Variation of total pitching-moment coefficient with angle of attack.

Figure 12. - Static, thrusting longitudinal stability characteristics for the Apollo launch escape vehicle determined in the Langley 16-Foot Tunnel at M = 0.9 (total coefficients, includes thrust components).

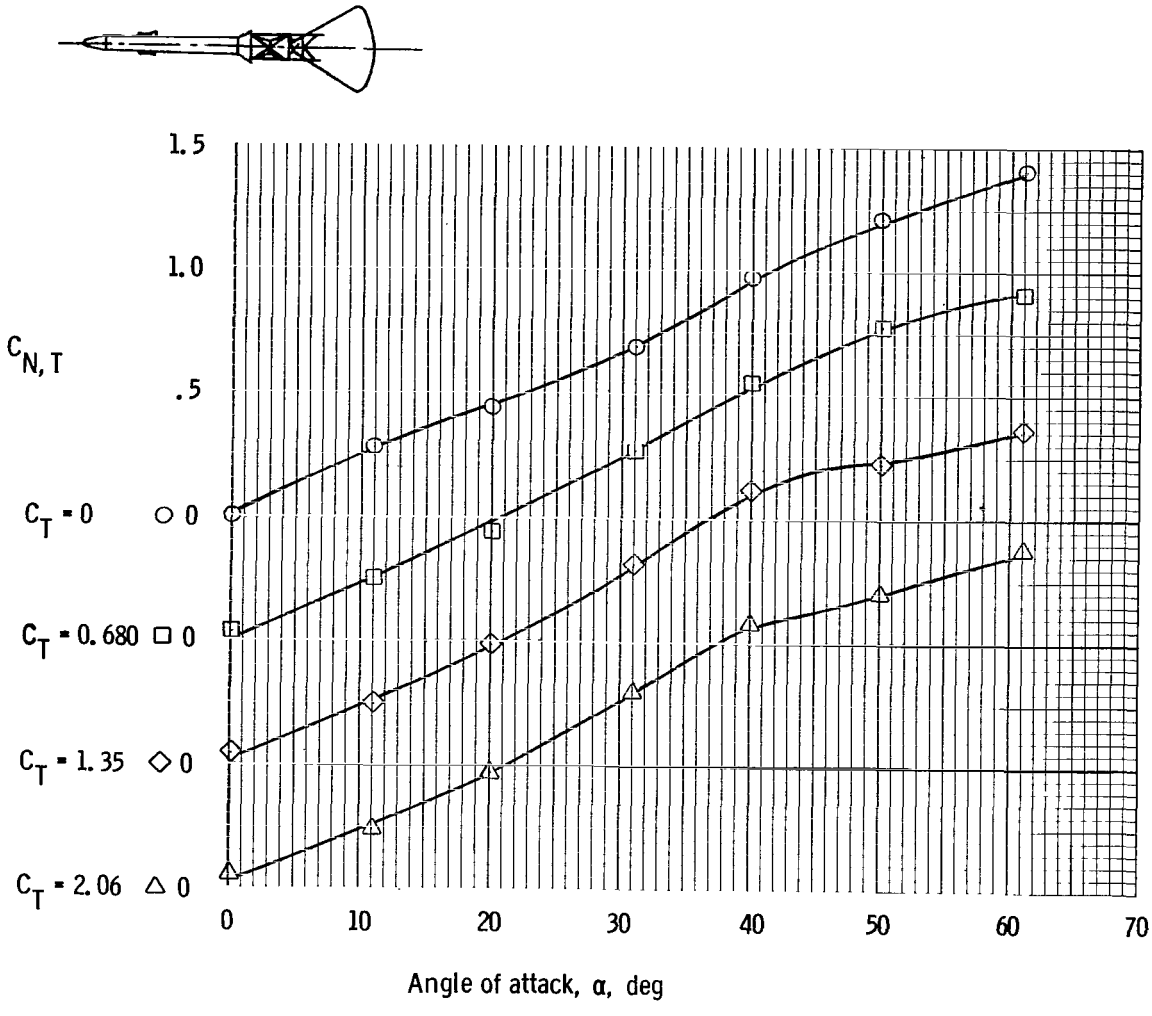

(b) Variation of total normal-force coefficient with angle of attack.

Figure 12. -Continued.

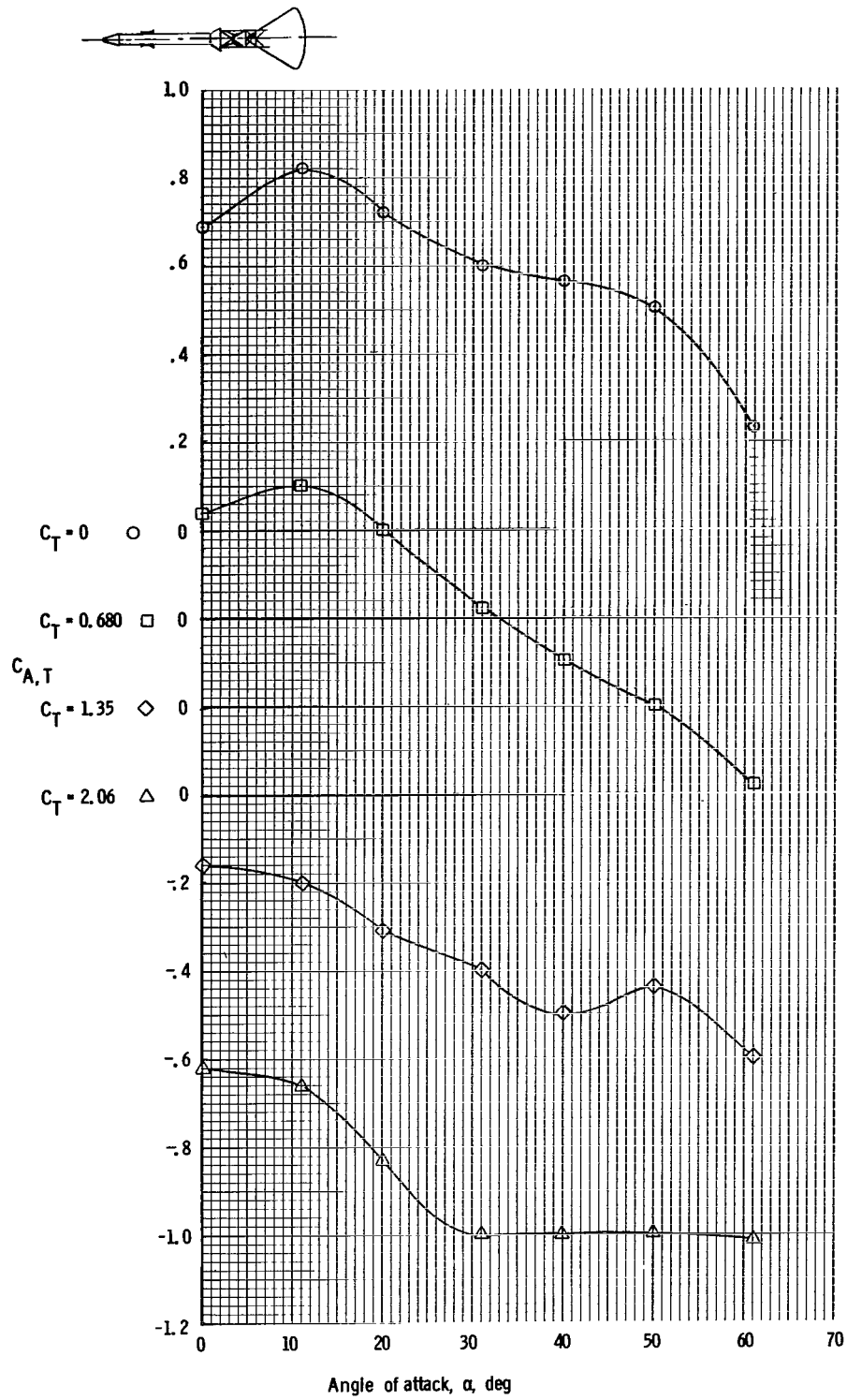

(c) Variation of total axial-force coefficient with angle of attack.

Figure 12. - Concluded.

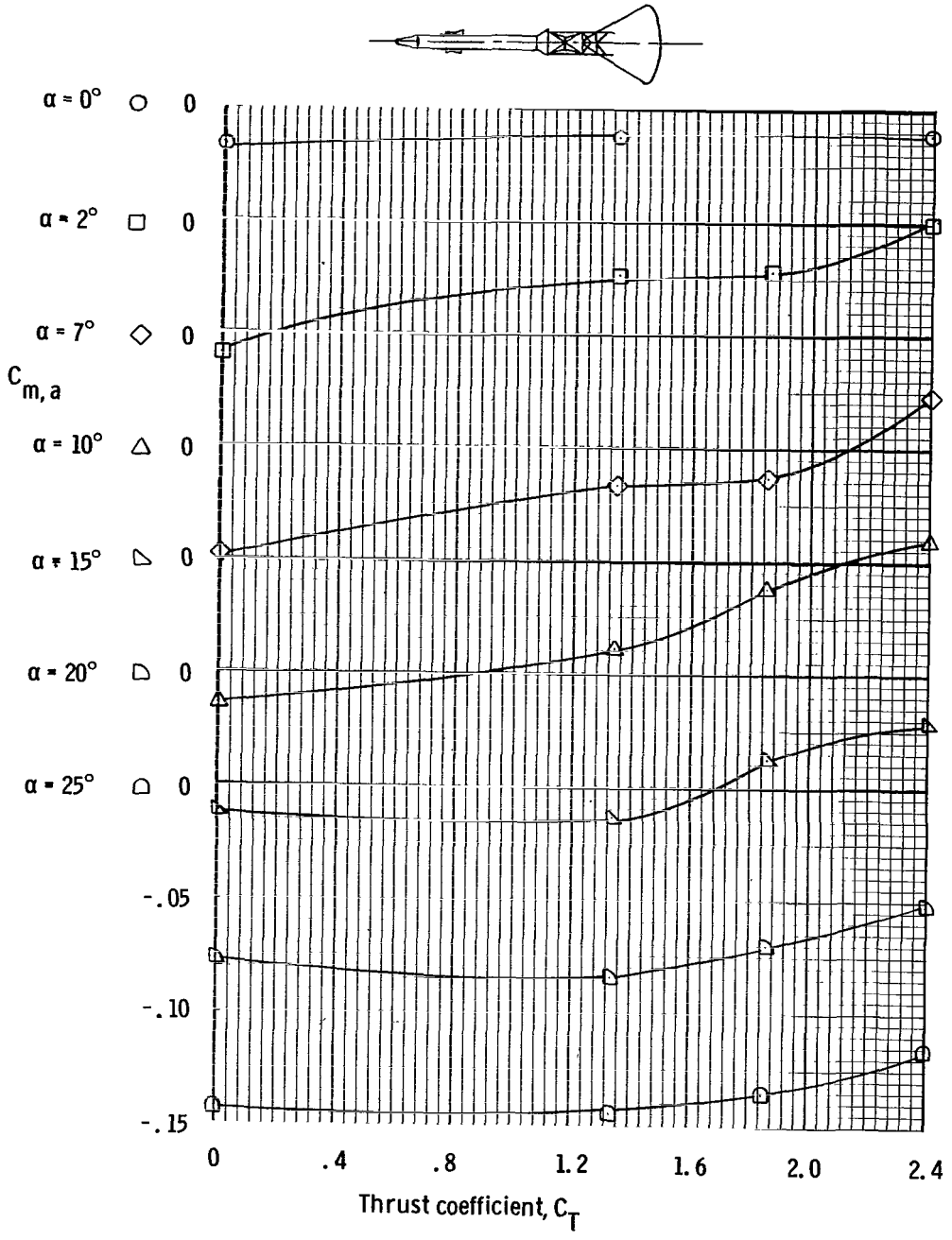

(a) Variation of pitching-moment coefficient with thrust coefficient at M = 0.7.

Figure 13.- Static, thrusting longitudinal stability characteristics of the Apollo launch escape vehicle determined in the AEDC-A Tunnel at Mach numbers from 0.7 to 5.97.

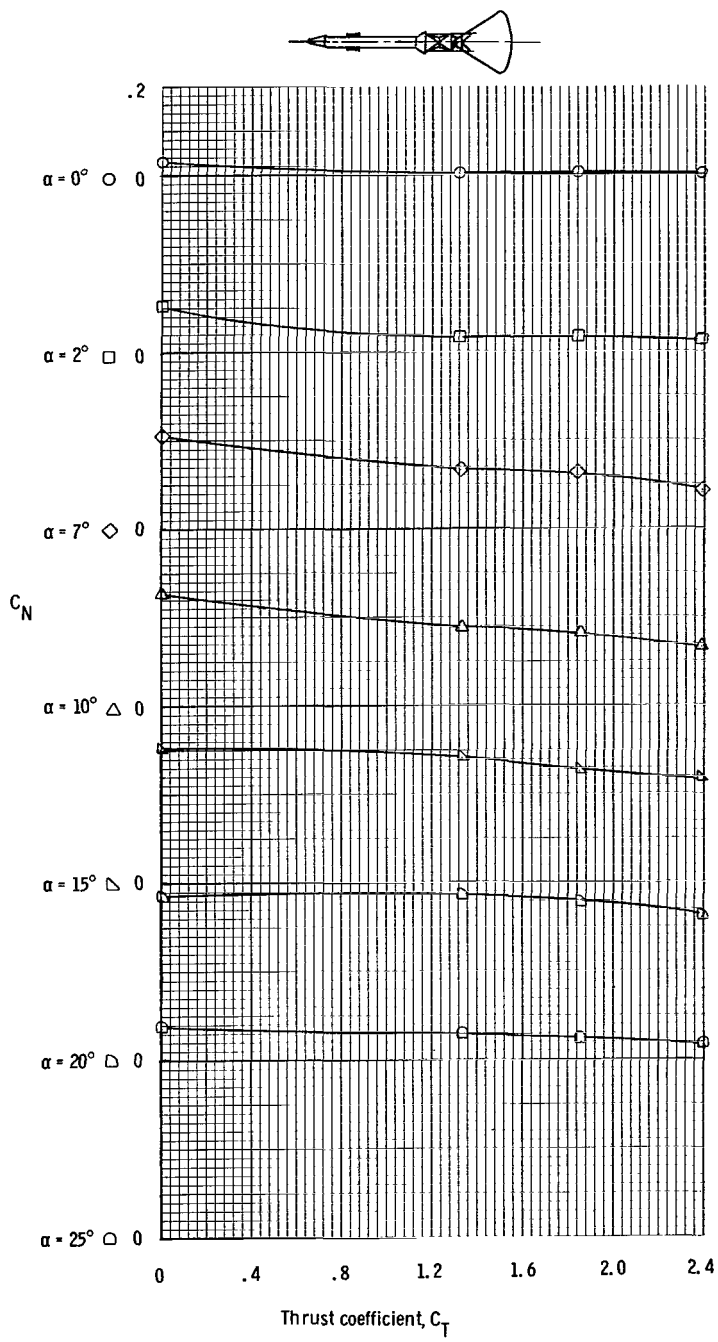

(b) Variation of normal-force coefficient with thrust coefficient at M = 0.7.

Figure 13. - Continued.

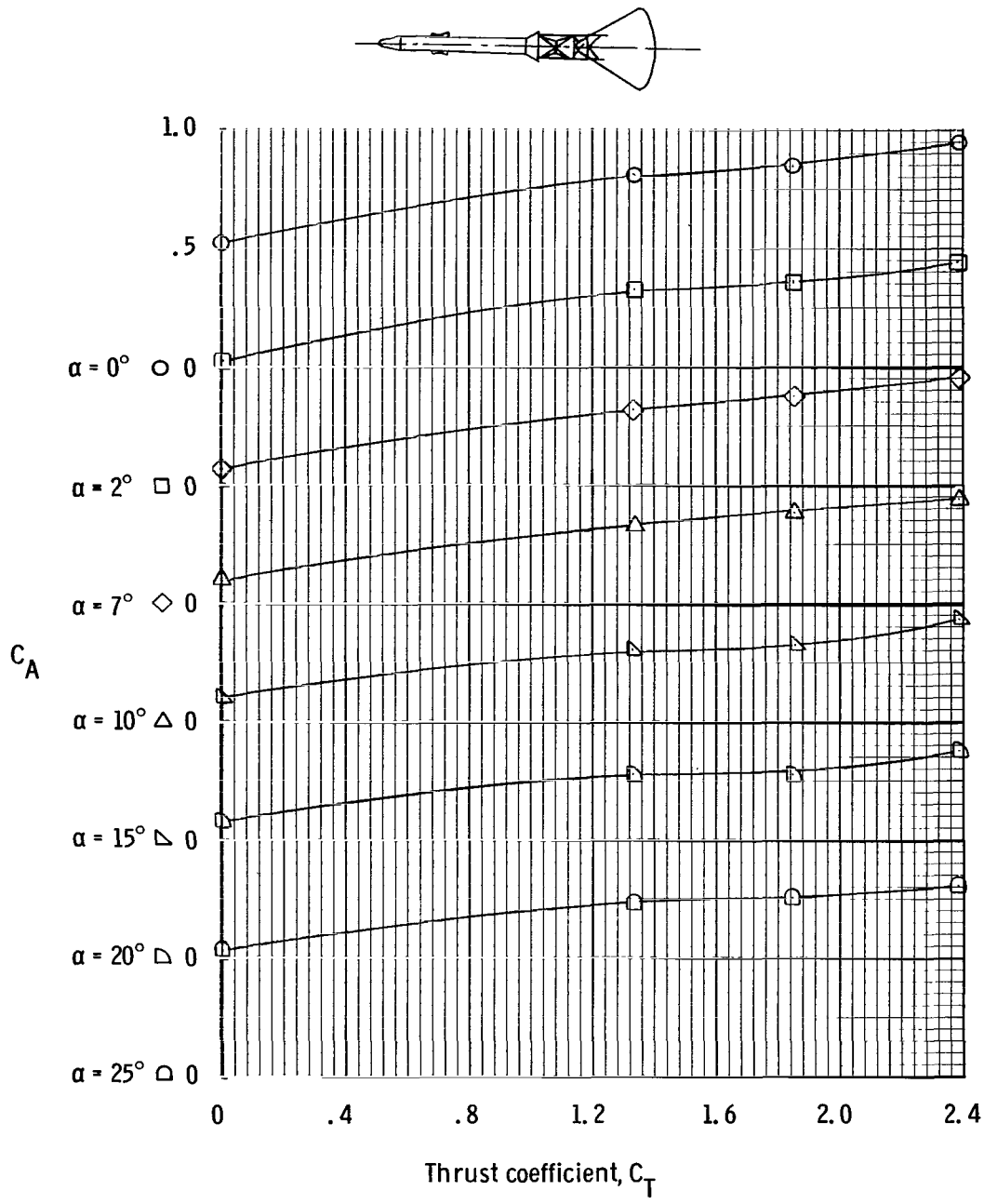

(c) Variation of axial-force coefficient with thrust coefficient at M = 0.7.

Figure 13. - Continued.

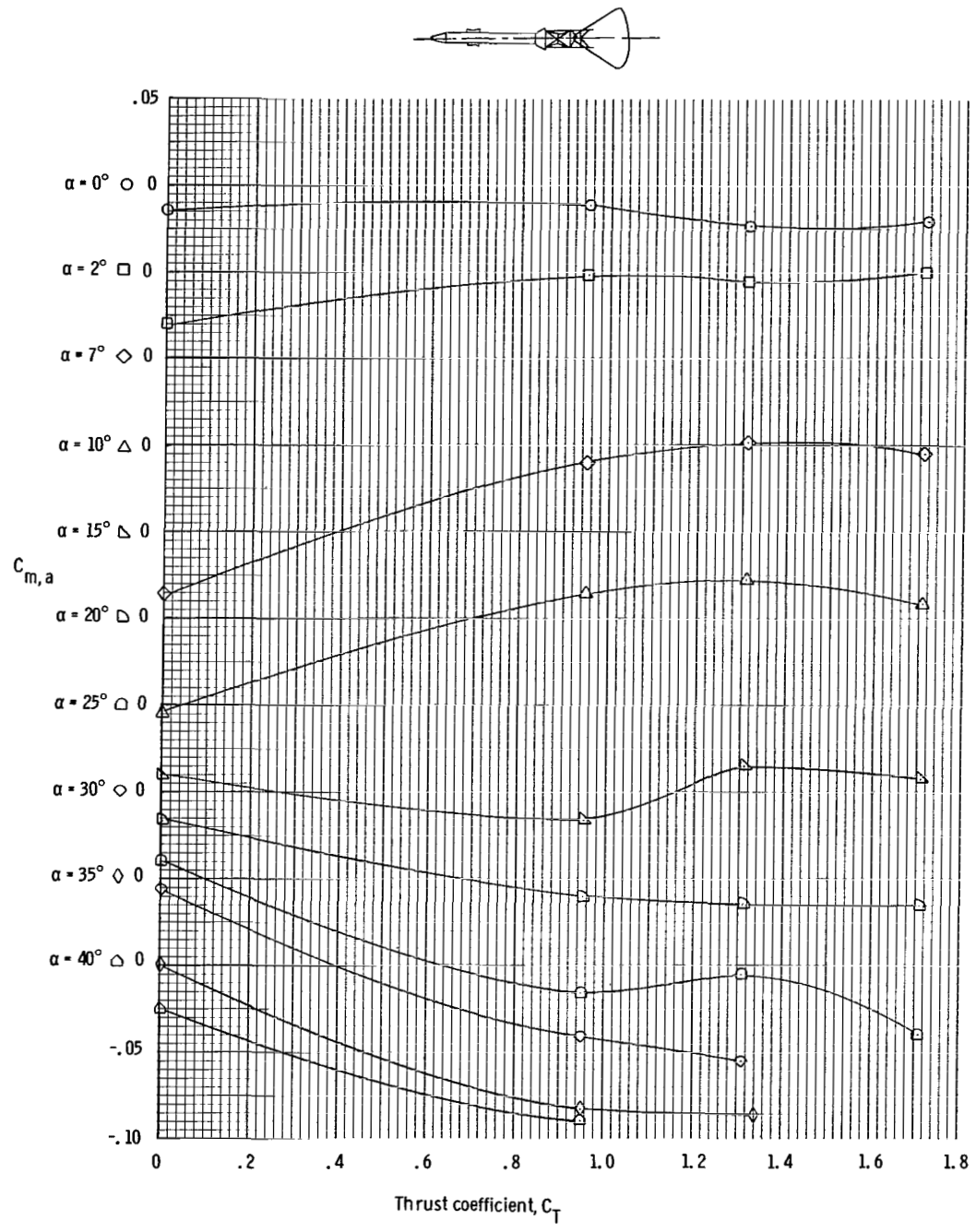

(d) Variation of pitching-moment coefficient with thrust coefficient at M = 1.48.

Figure 13. - Continued.

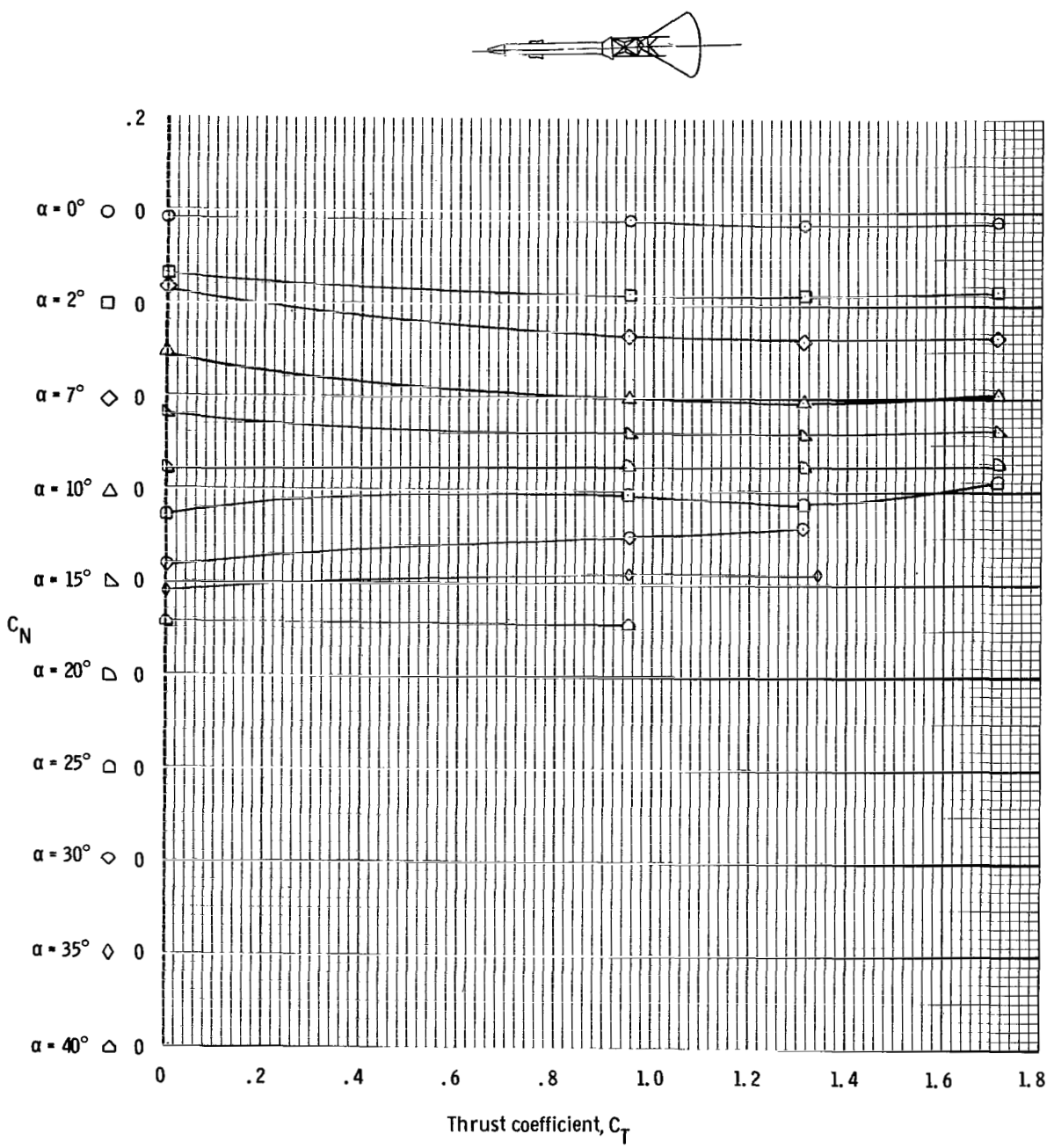

(e) Variation of normal-force coefficient with thrust coefficient at $M = 1.48$.

Figure 13. - Continued.

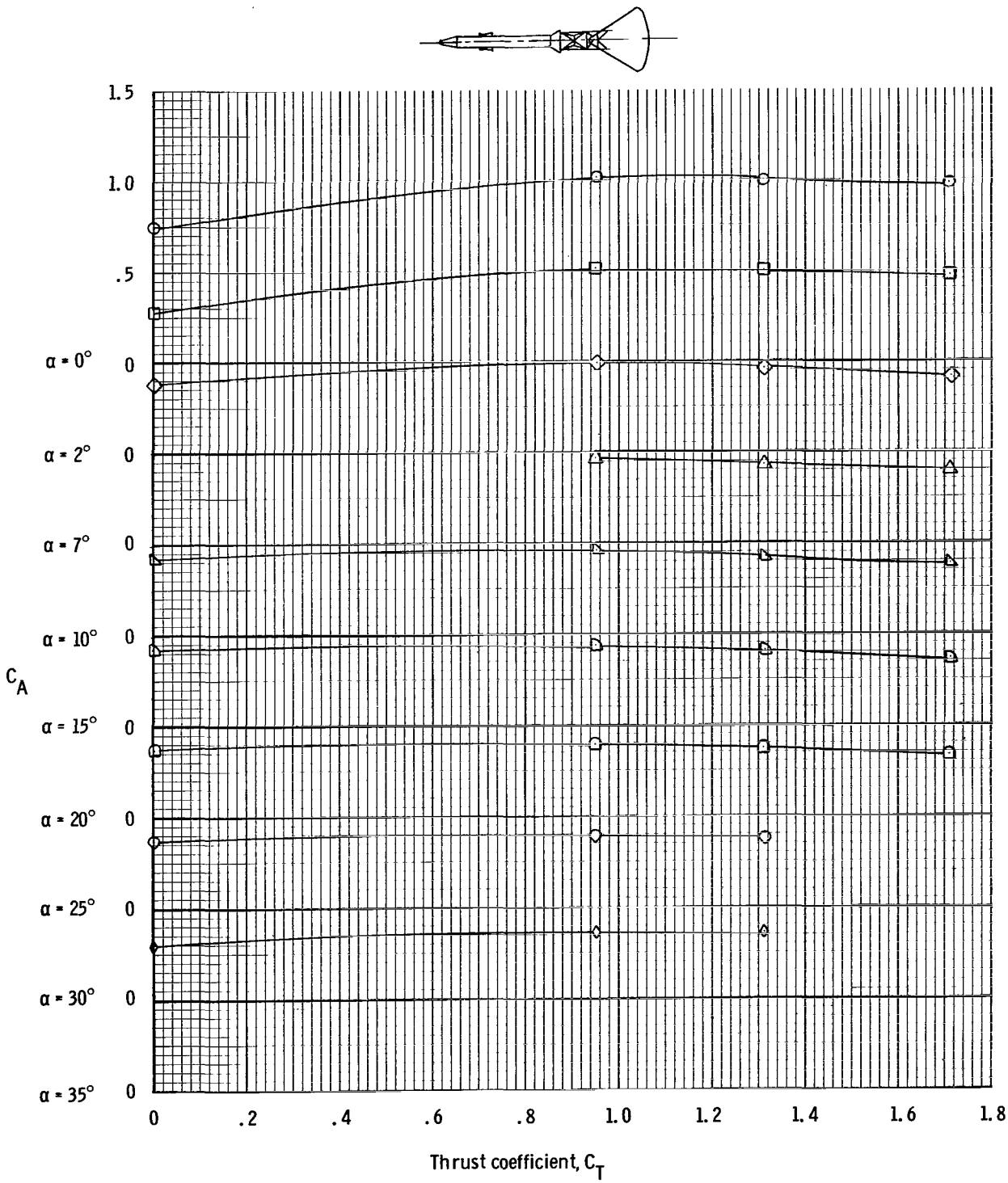

(f) Variation of axial-force coefficient with thrust coefficient at $M = 1.48$.

Figure 13. - Continued.

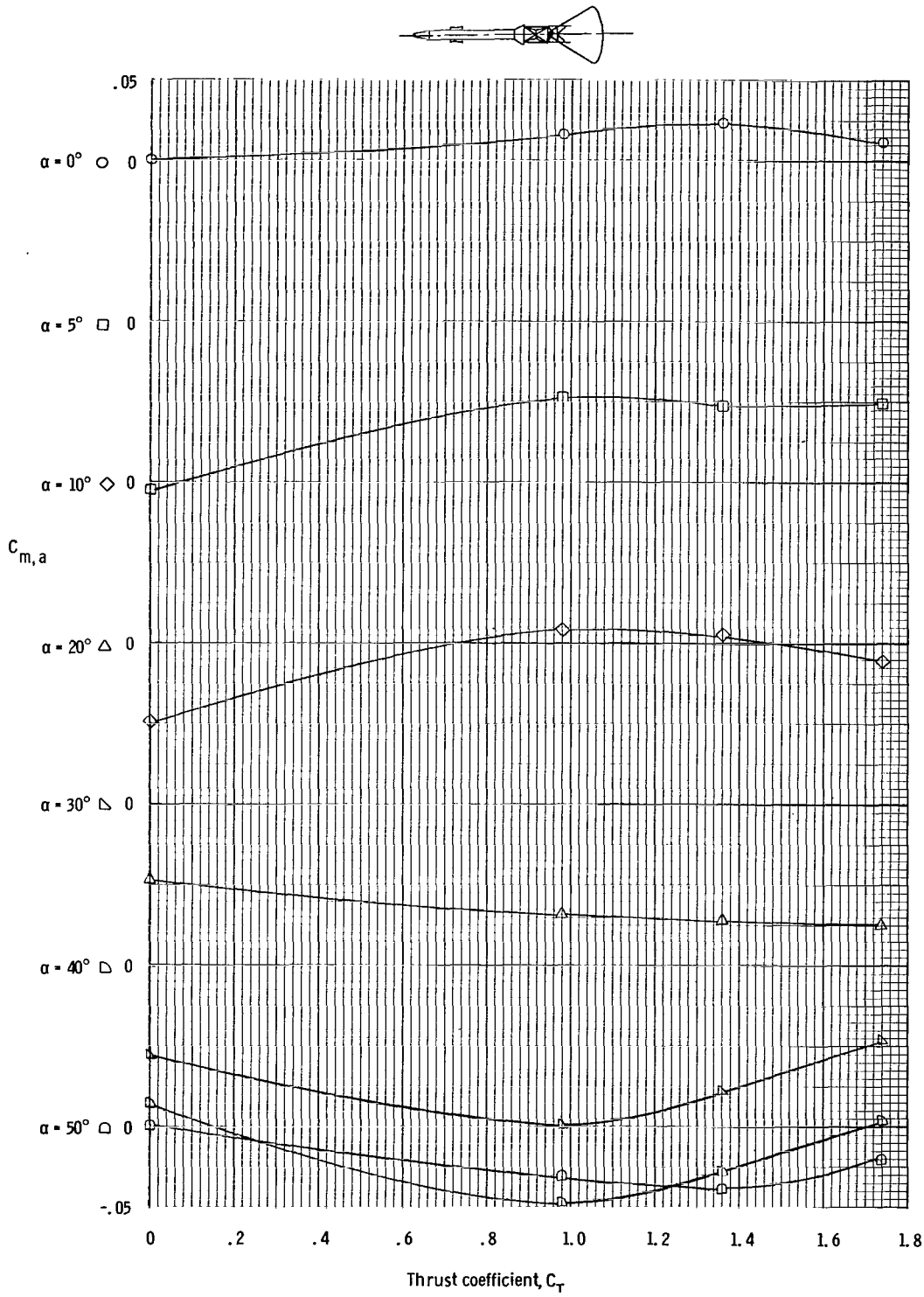

(g) Variation of pitching-moment coefficient with thrust coefficient at $M = 1.98$.

Figure 13. - Continued.

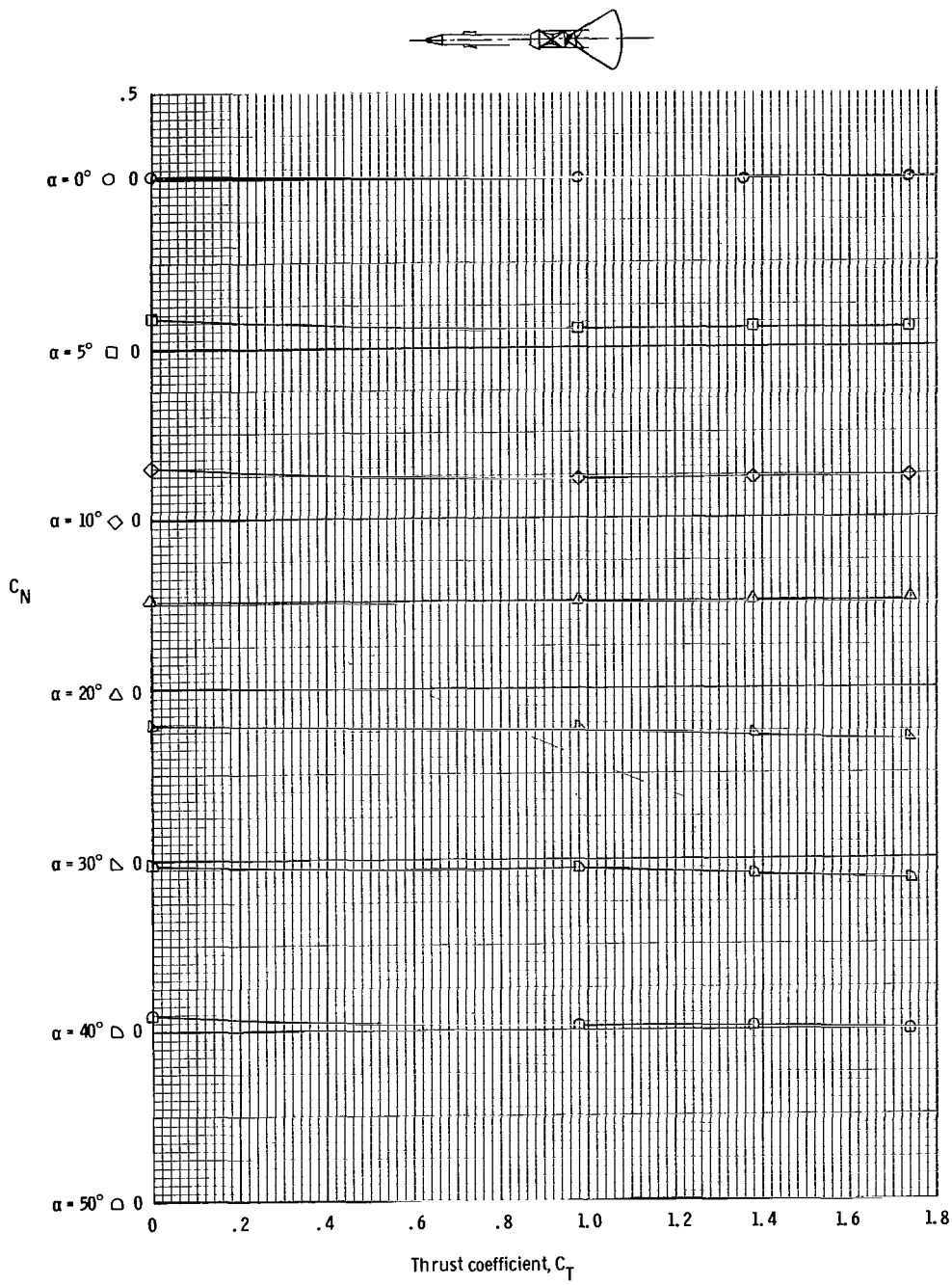

(h) Variation of normal-force coefficient with thrust coefficient at M = 1.98.

Figure 13. - Continued.

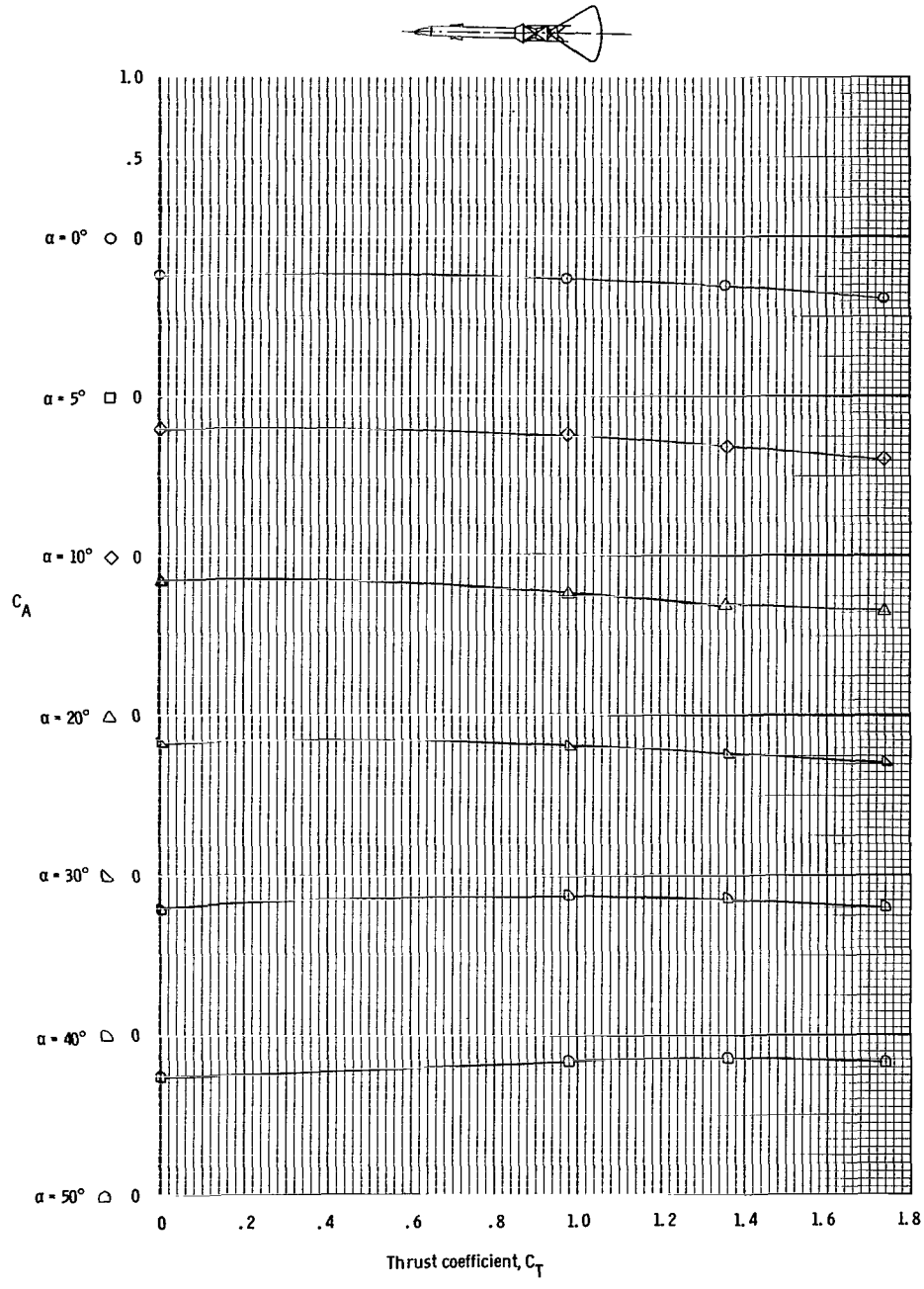

(i) Variation of axial-force coefficient with thrust coefficient at M = 1.98.

Figure 13. - Continued.

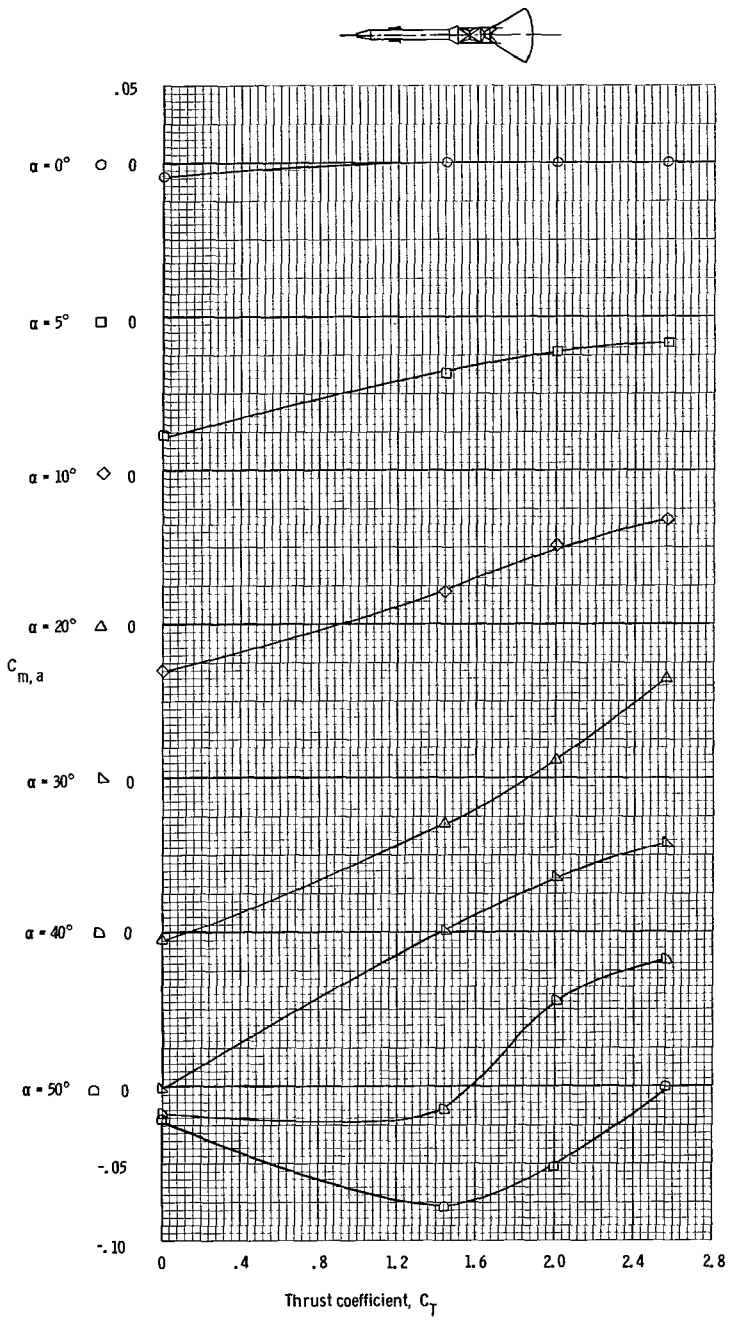

(j) Variation of pitching-moment coefficient with thrust coefficient at M = 2.99.

Figure 13. - Continued.

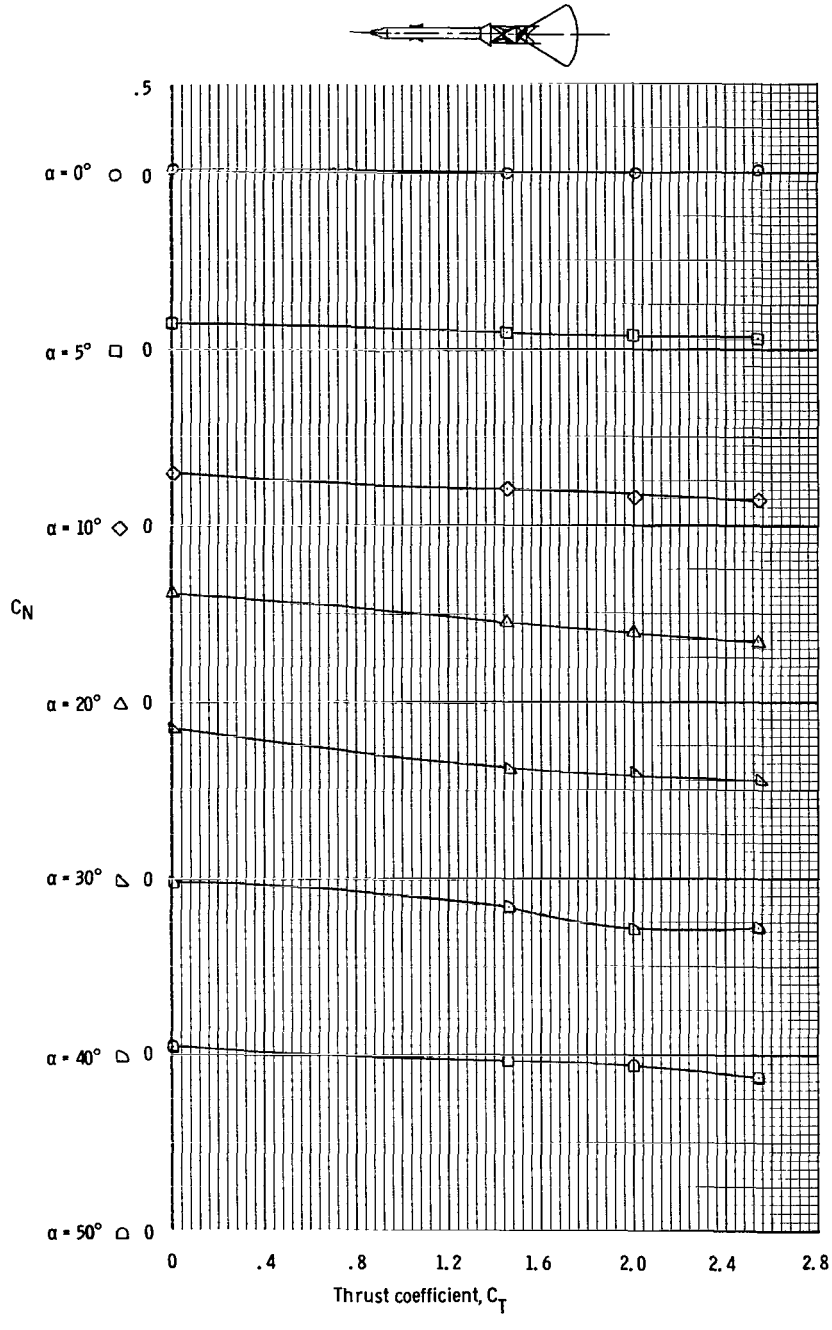

(k) Variation of normal-force coefficient with thrust coefficient at M = 2.99.

Figure 13. - Continued.

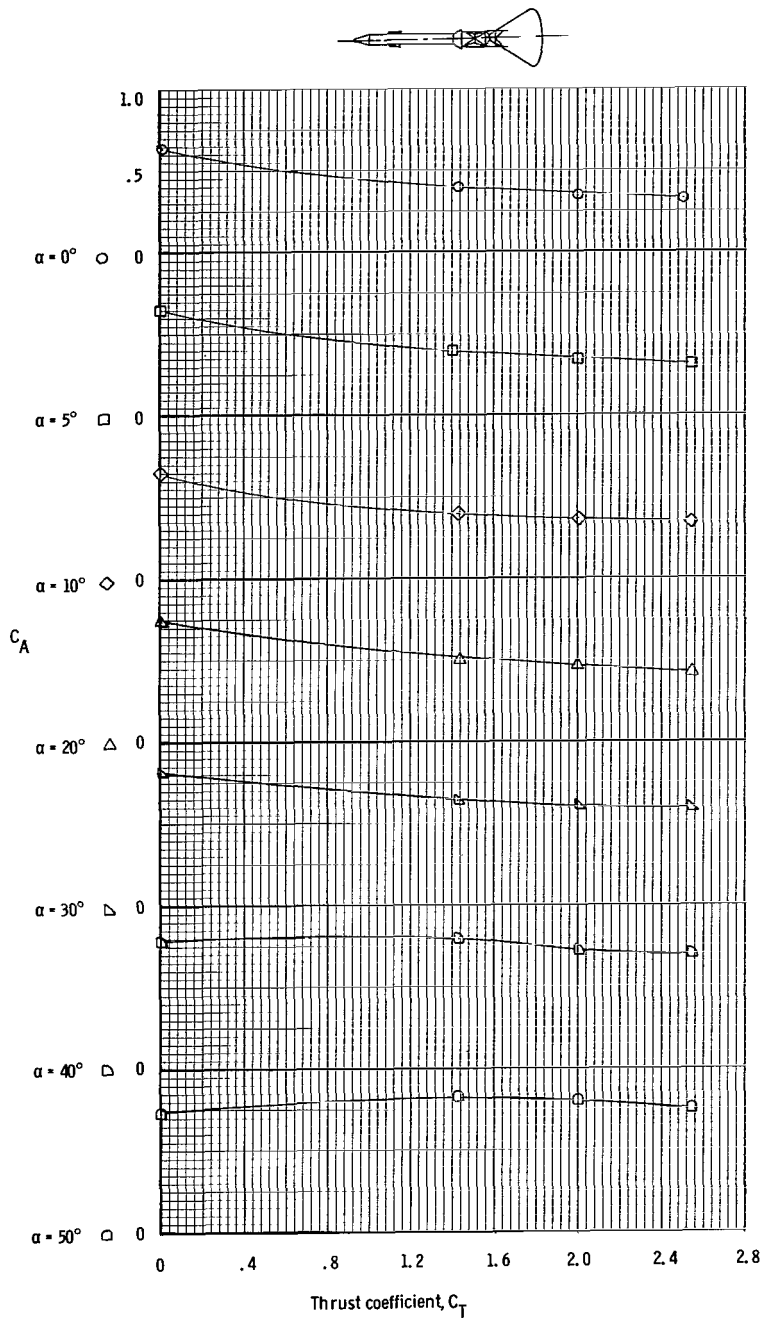

(l) Variation of axial-force coefficient with thrust coefficient at M = 2.99.

Figure 13. - Continued.

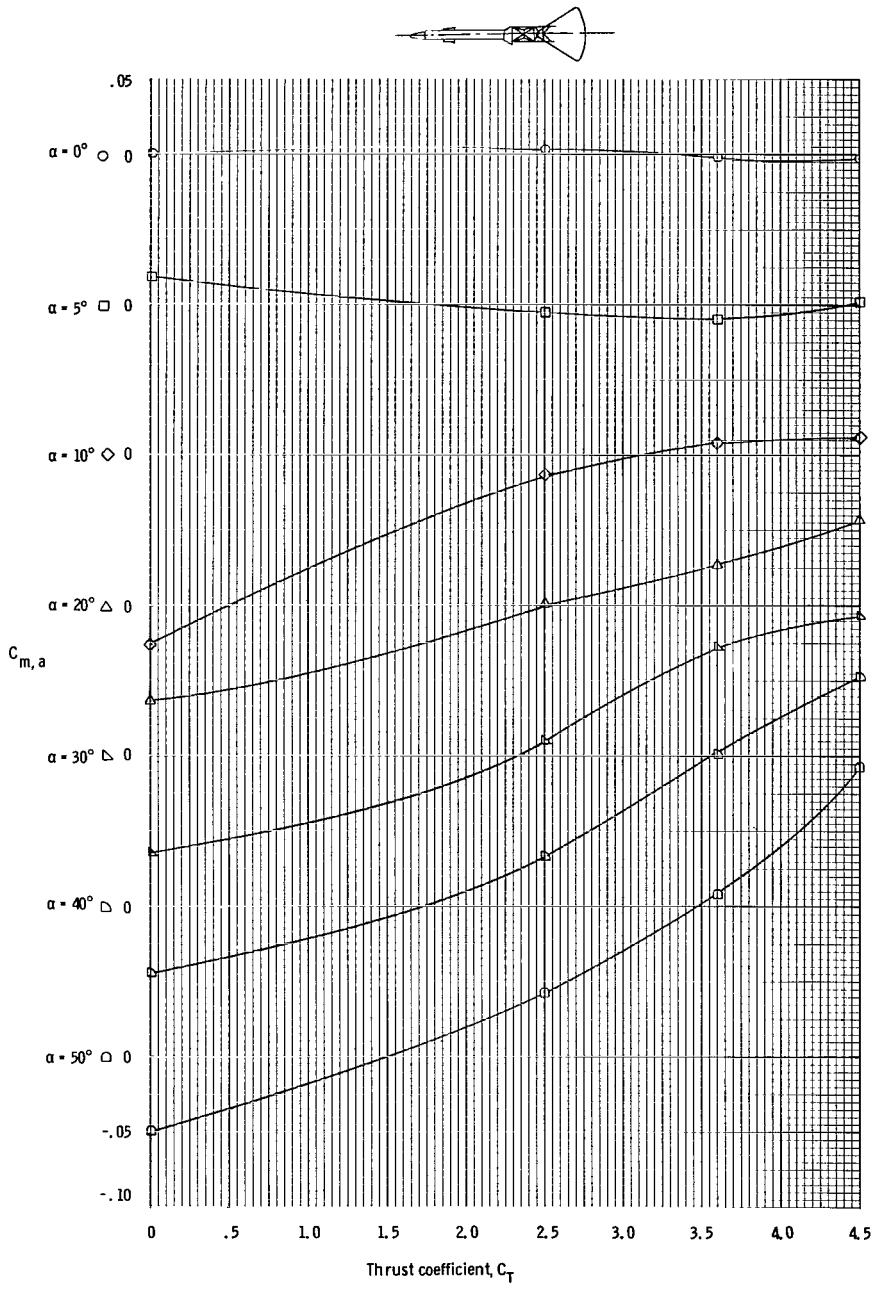

(m) Variation of pitching-moment coefficient with thrust coefficient at M = 3.99.

Figure 13. - Continued.

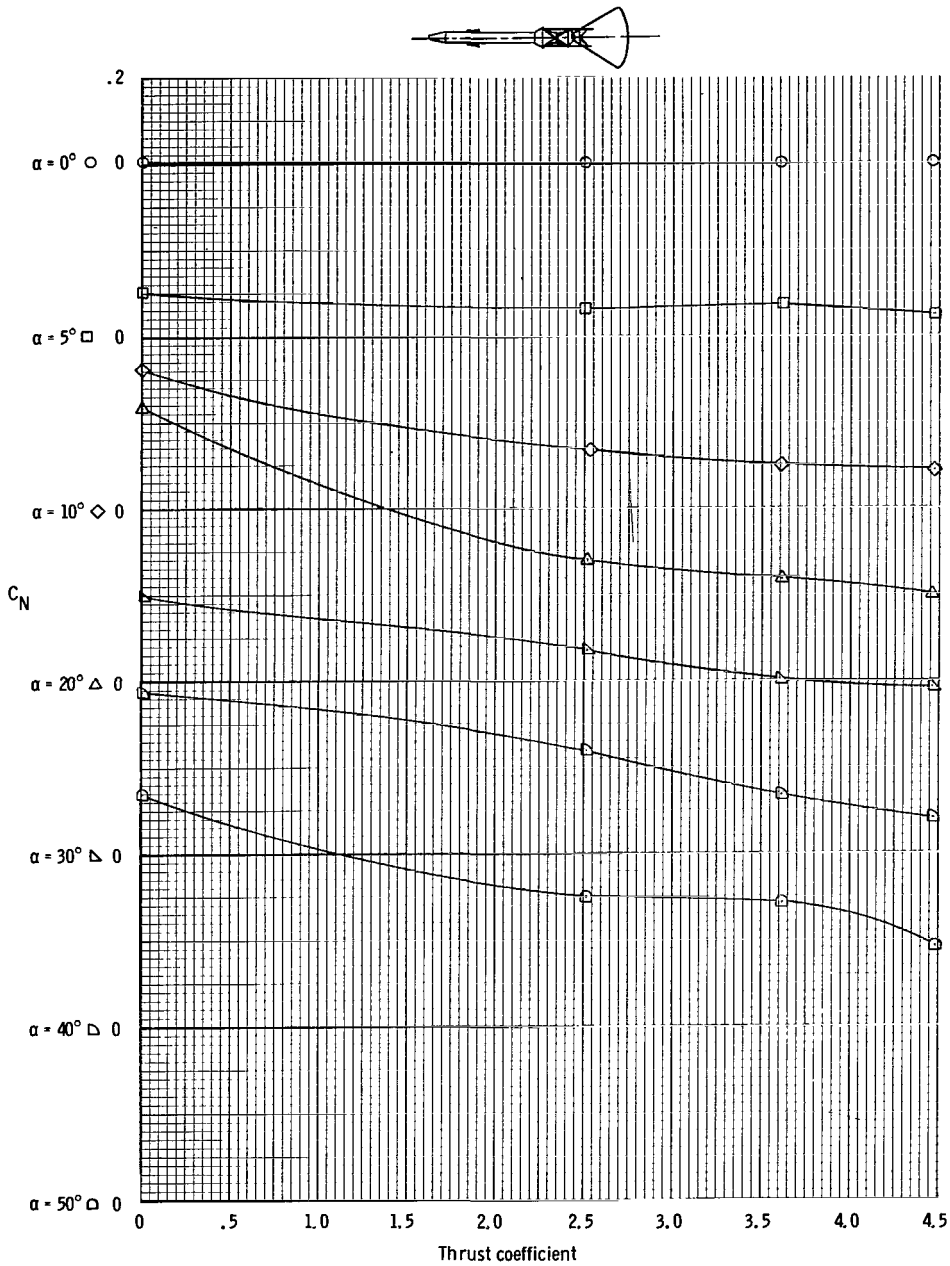

(n) Variation of normal-force coefficient with thrust coefficient at M = 3.99.

Figure 13. - Continued.

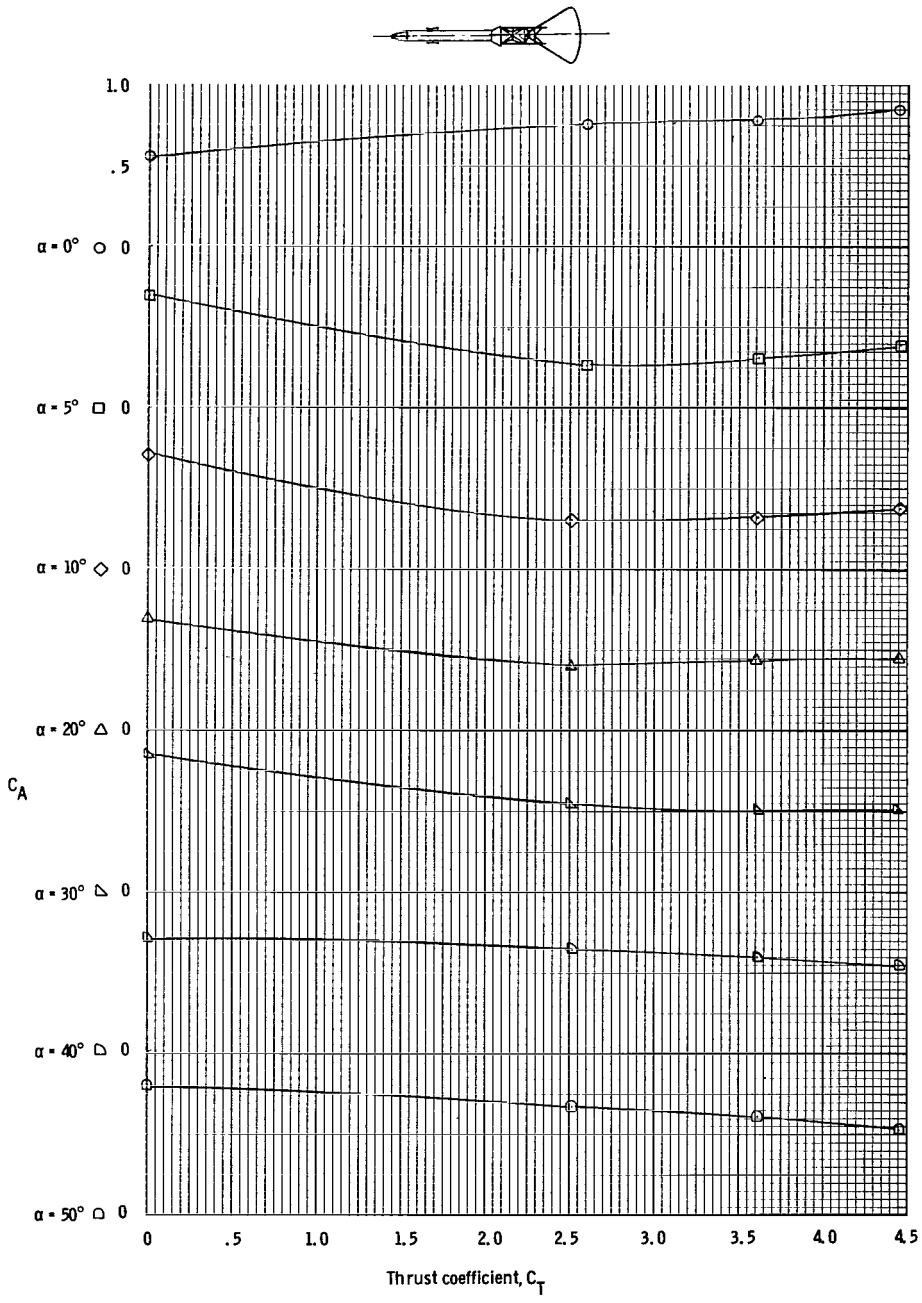

(o) Variation of axial-force coefficient with thrust coefficient at M = 3.99.

Figure 13. - Continued.

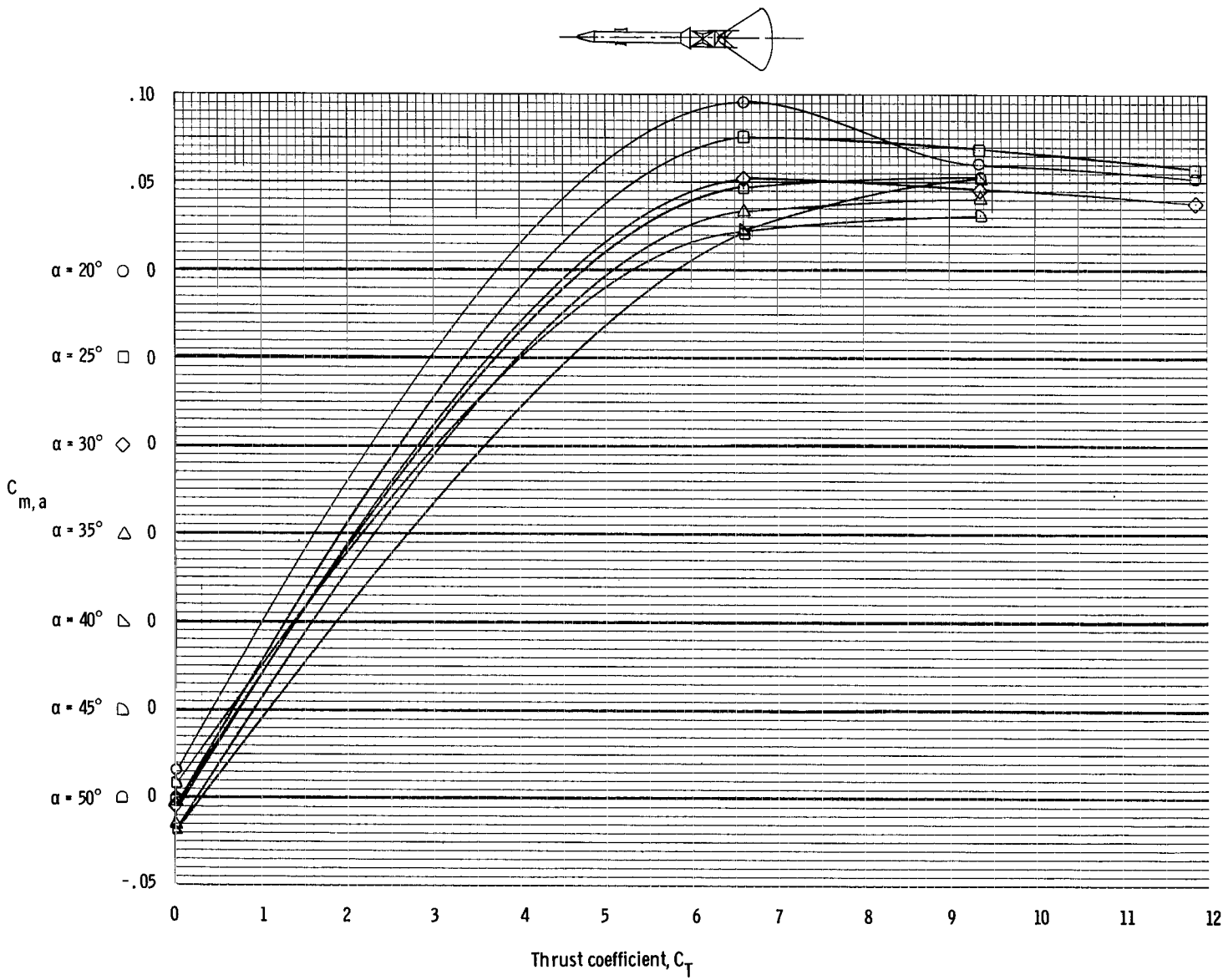

(p) Variation of pitching-moment coefficient with thrust coefficient at $M = 4.99$.

Figure 13. - Continued.

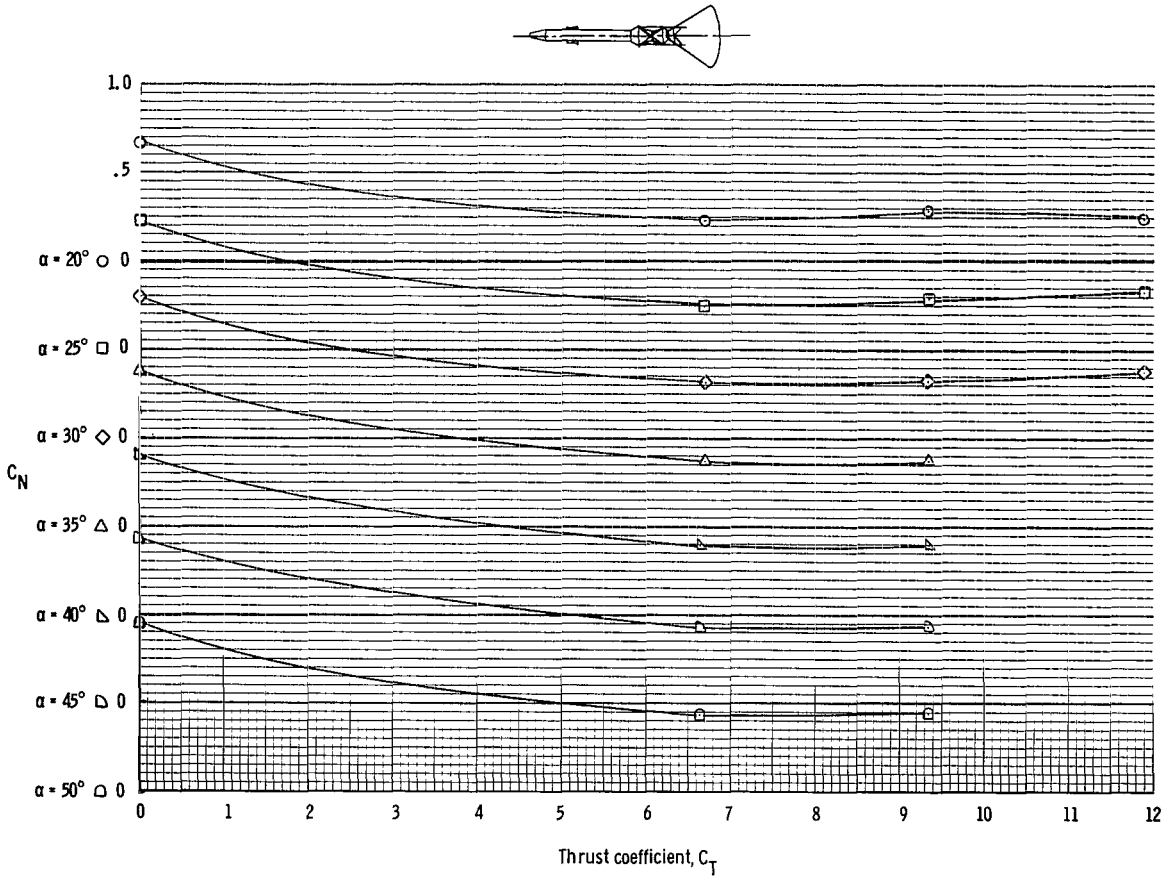

(q) Variation of normal-force coefficient with thrust coefficient at $M = 4.99$.

Figure 13. - Continued.

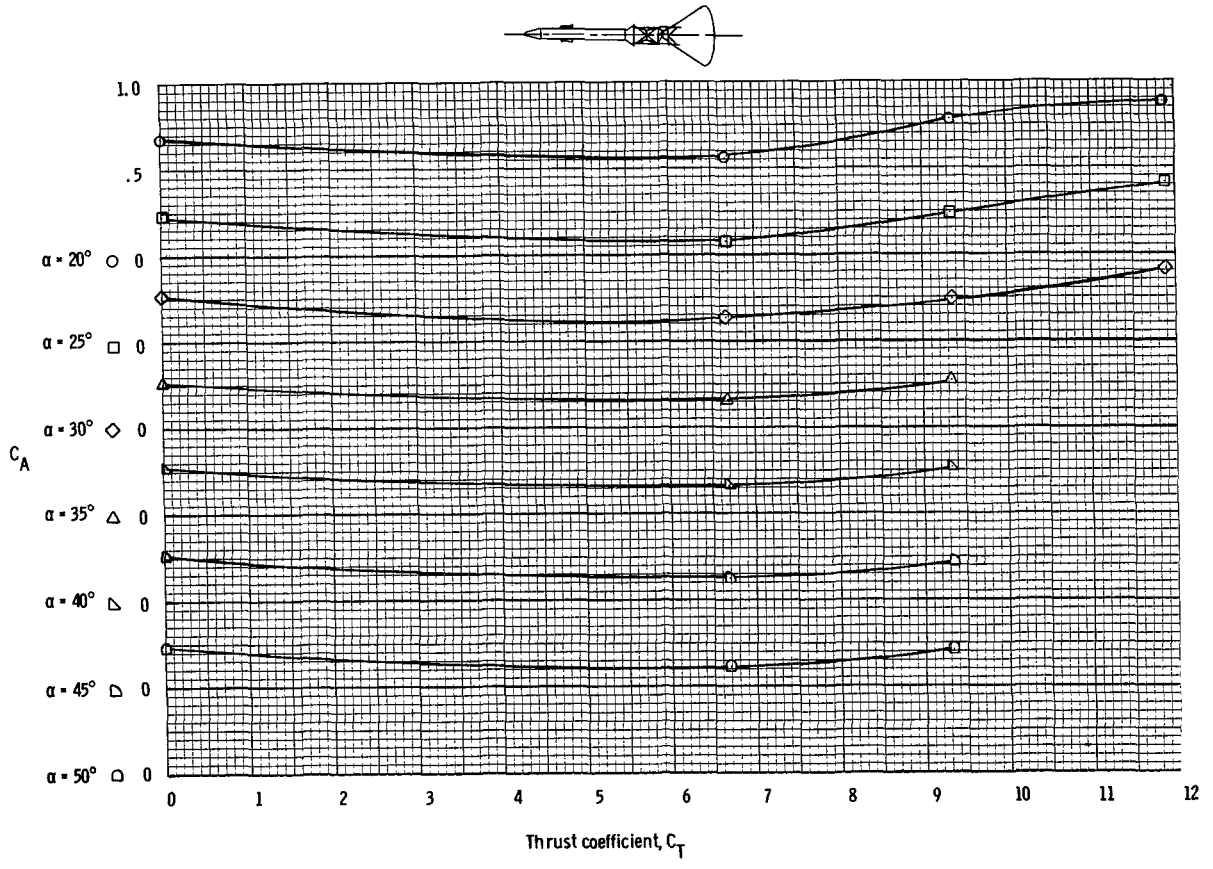

(r) Variation of axial-force coefficient with thrust coefficient at $M = 4.99$.

Figure 13. - Continued.

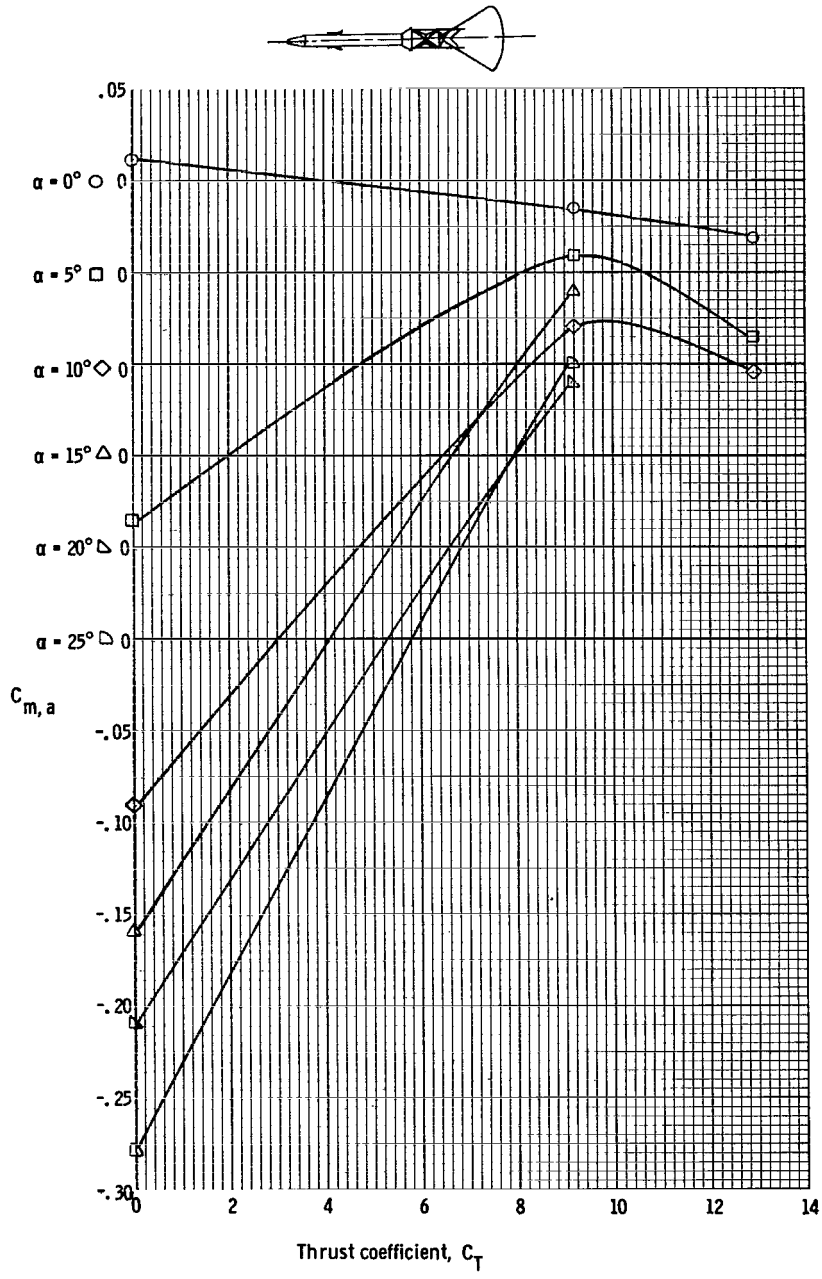

(s) Variation of pitching-moment coefficient with thrust coefficient at M = 5.97.

Figure 13. - Continued.

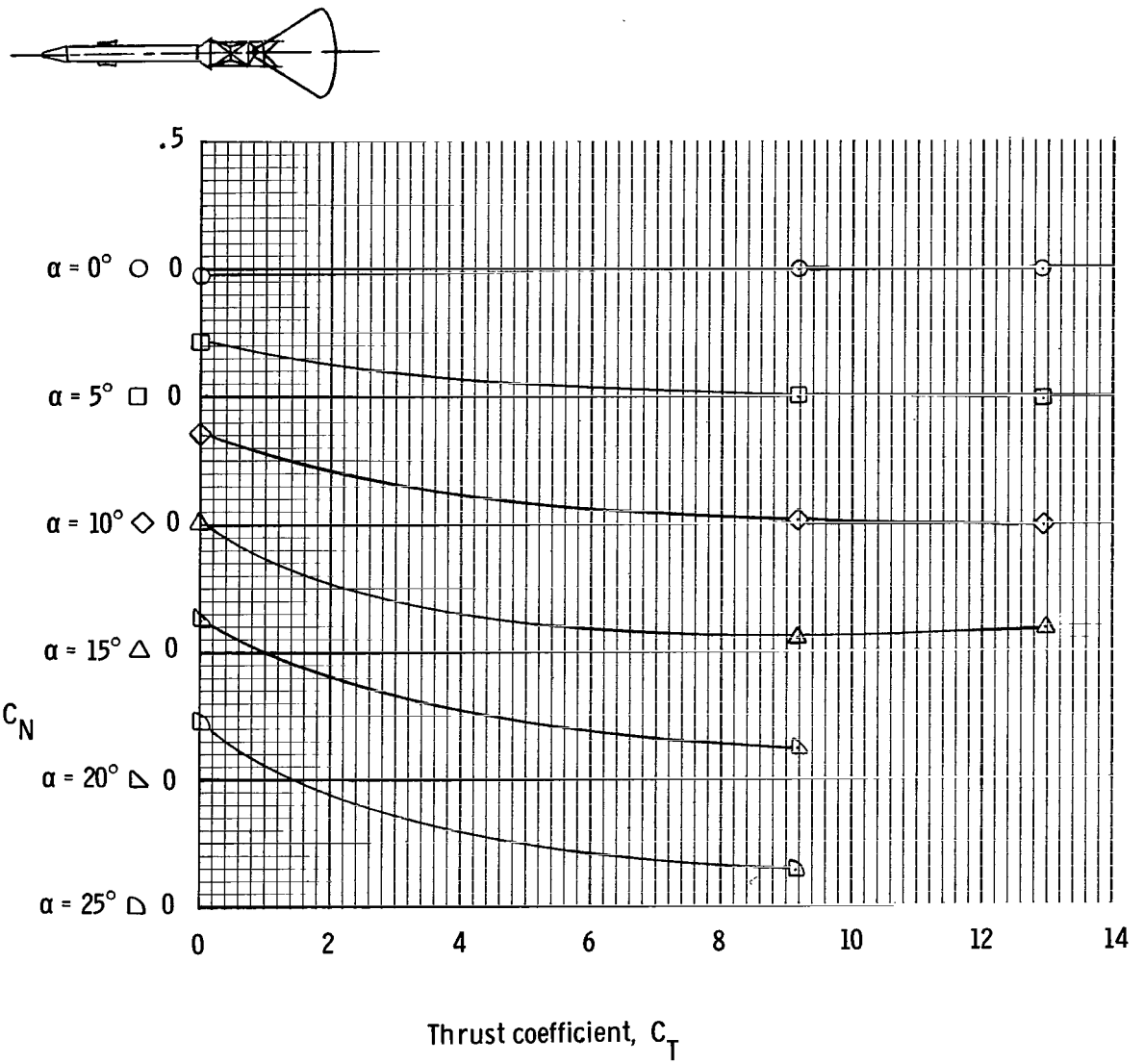

(t) Variation of normal-force coefficient with thrust coefficient at $M = 5.97$.

Figure 13. - Continued.

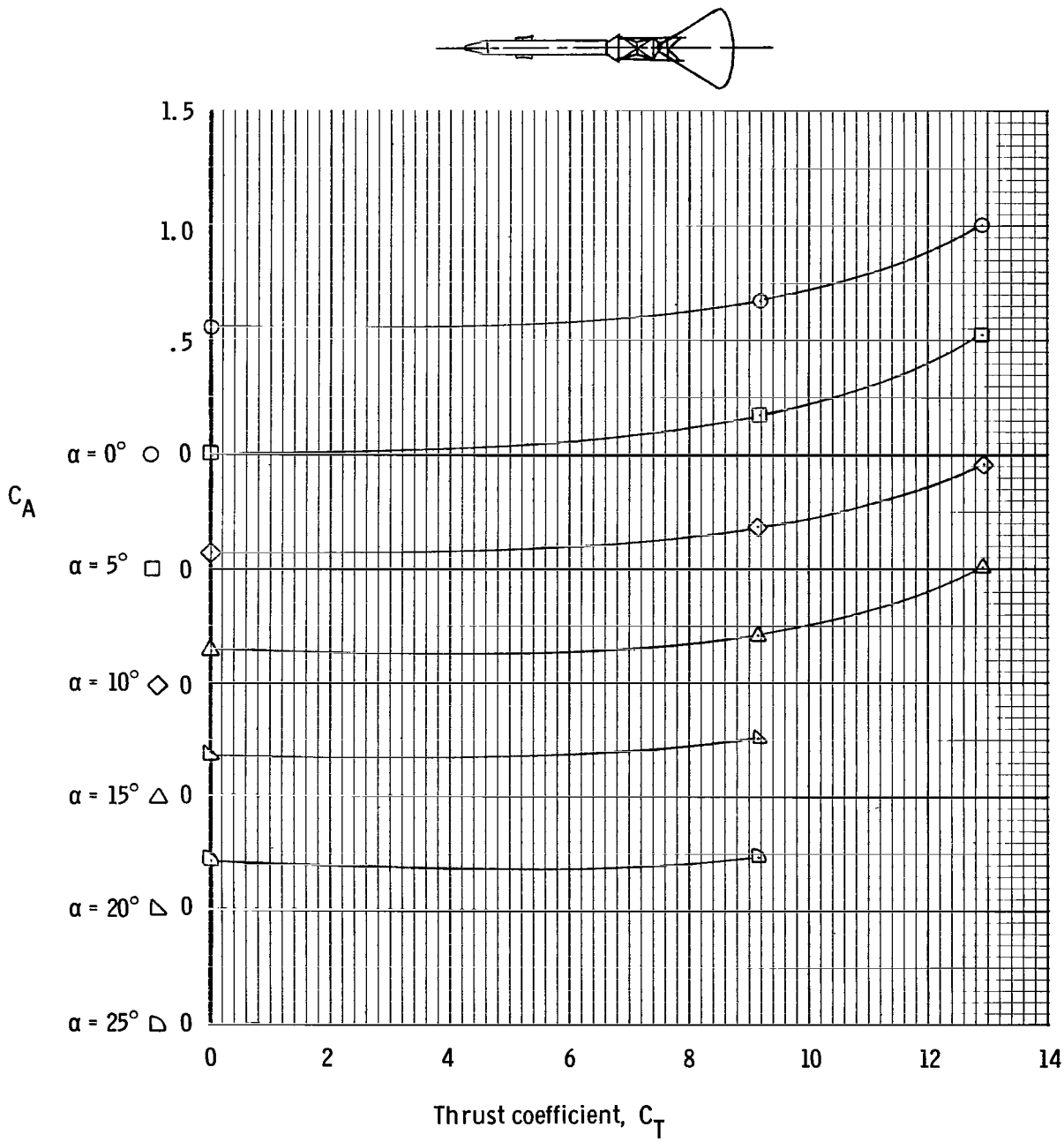

(u) Variation of axial-force coefficient with thrust coefficient at M = 5.97.

Figure 13. - Concluded.

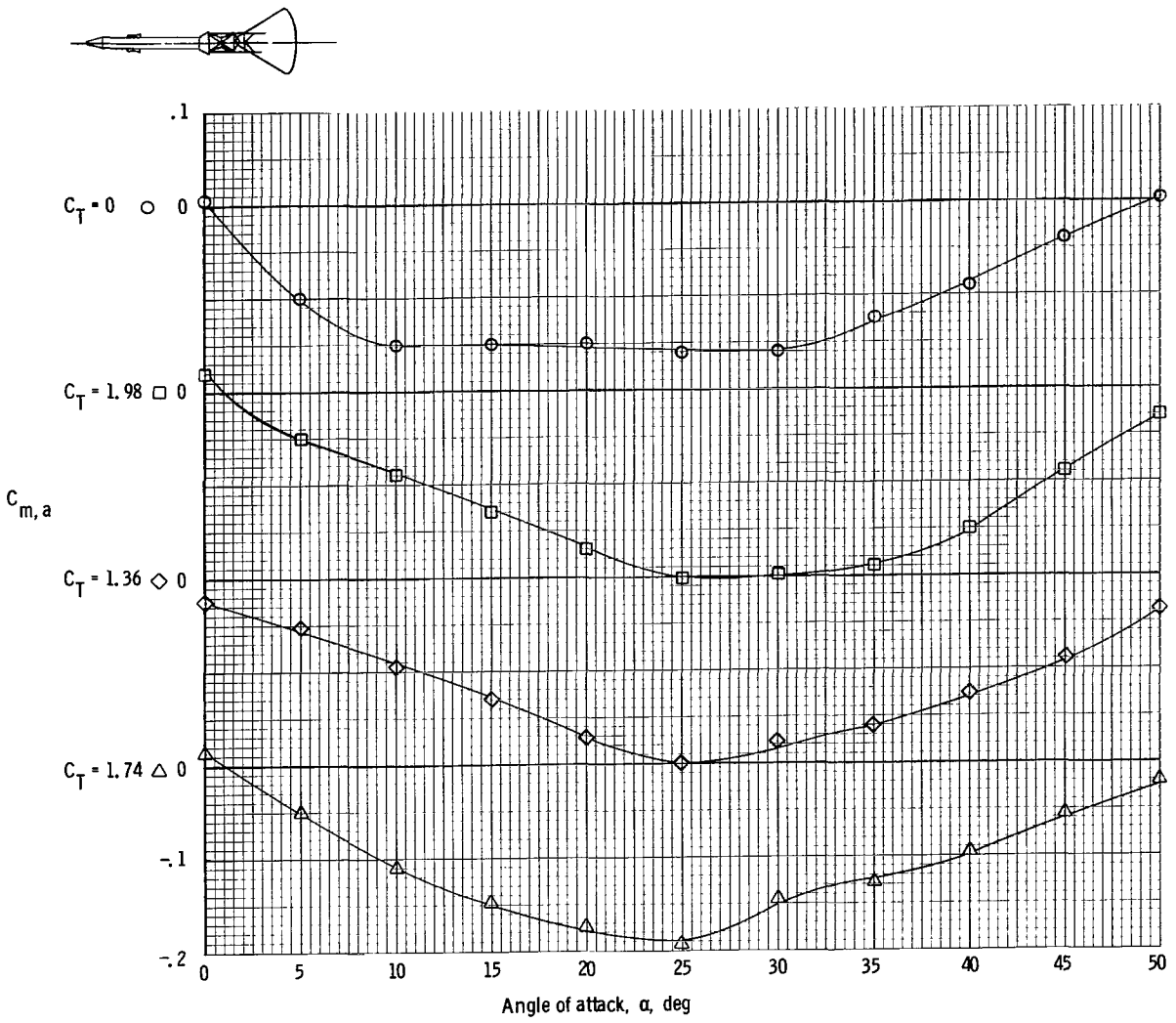

(a) Variation of pitching-moment coefficient with angle of attack at M = 1.98.

Figure 14. - Static, thrusting longitudinal stability characteristics of the Apollo launch escape vehicle at M = 1.98 to 5.97 as determined in the AEDC-A Tunnel.

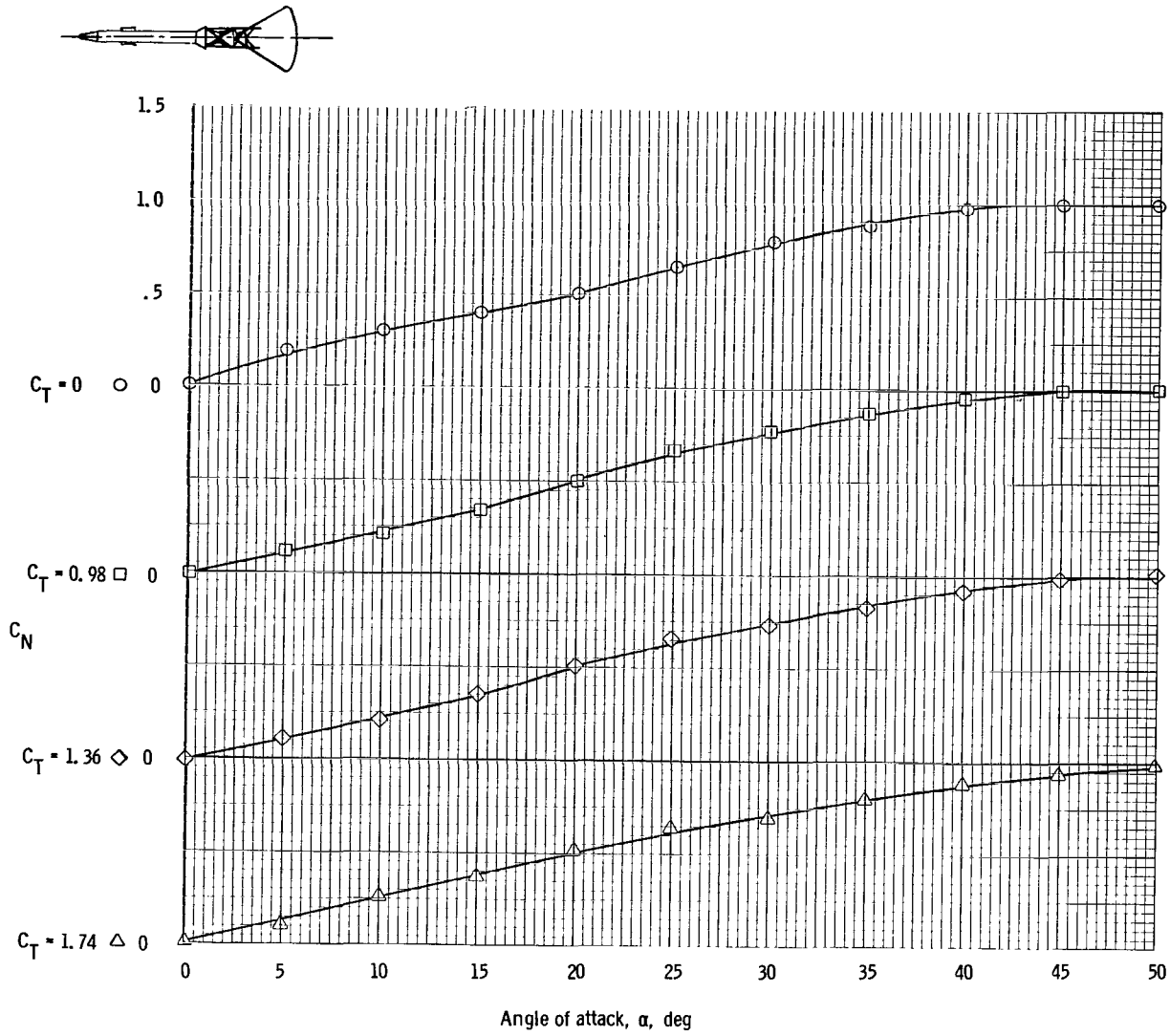

(b) Variation of normal-force coefficient with angle of attack at M = 1.98.

Figure 14. - Continued.

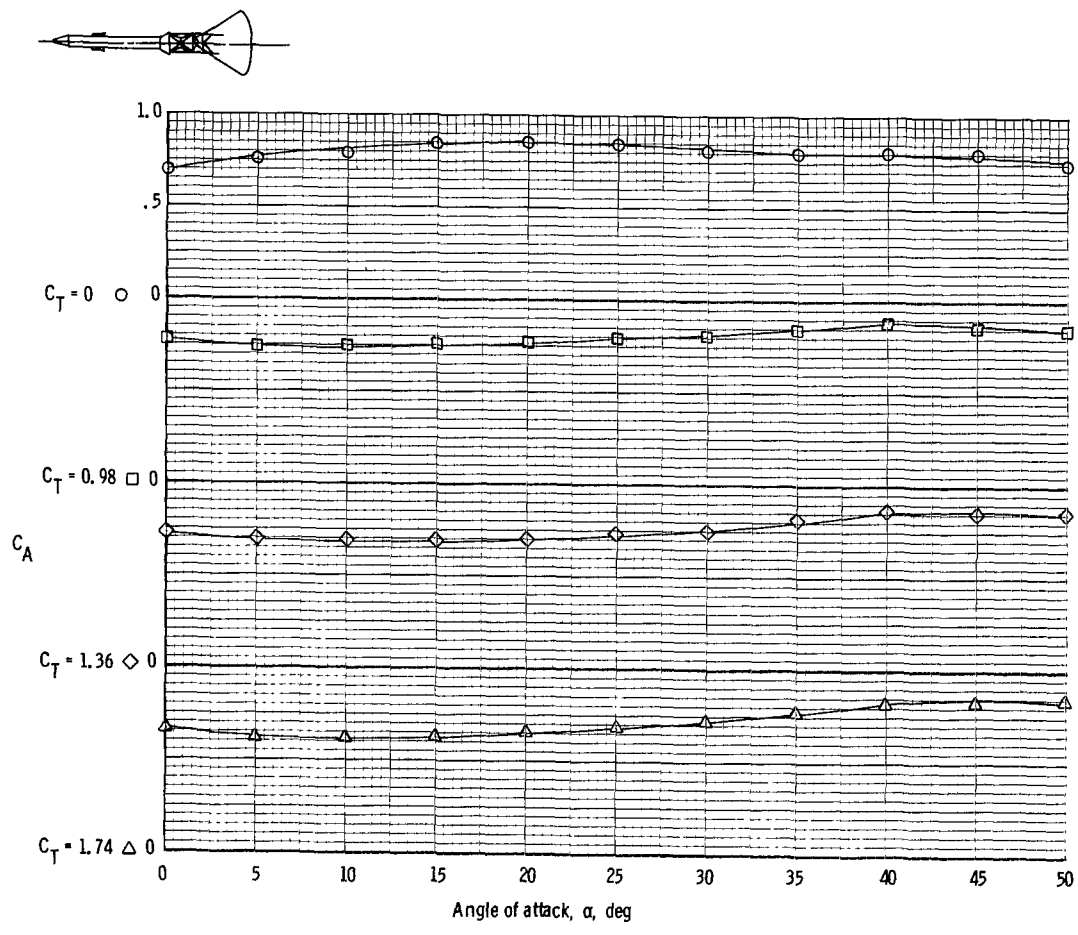

(c) Variation of axial-force coefficient with angle of attack at $M = 1.98$.

Figure 14. - Continued.

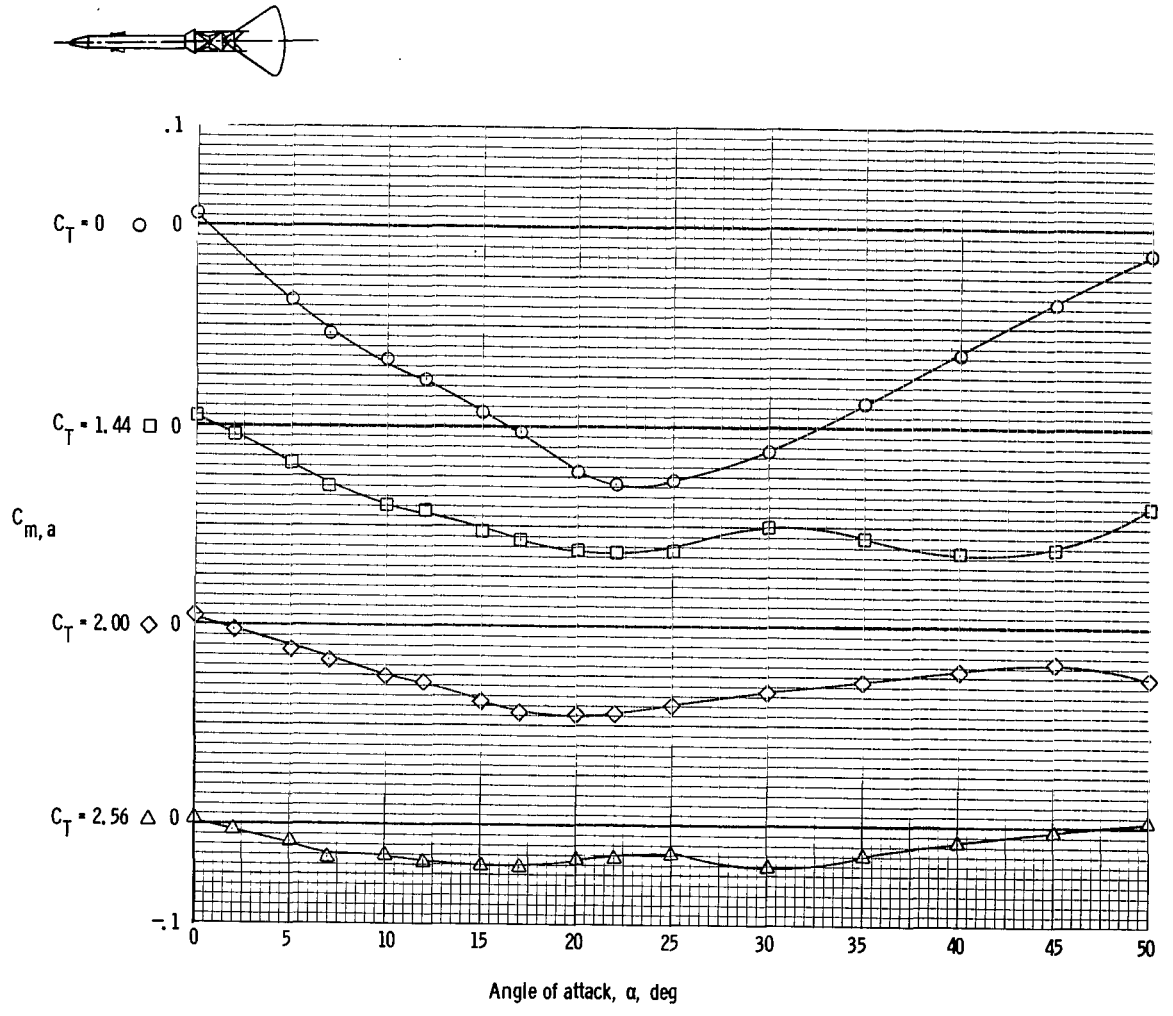

(d) Variation of pitching-moment coefficient with angle of attack at $M = 2.99$.

Figure 14. - Continued.

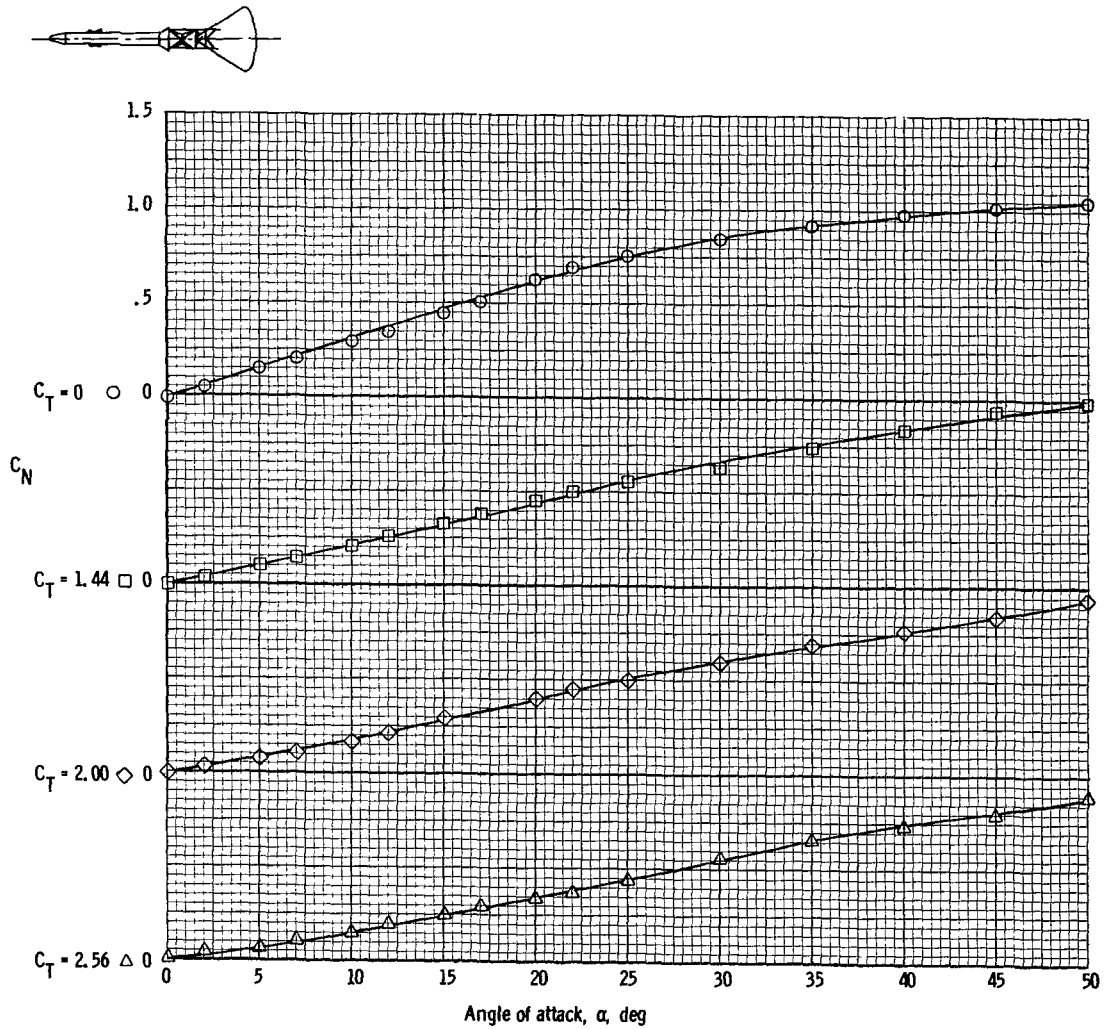

(e) Variation of normal-force coefficient with angle of attack at $M = 2.99$.

Figure 14. - Continued.

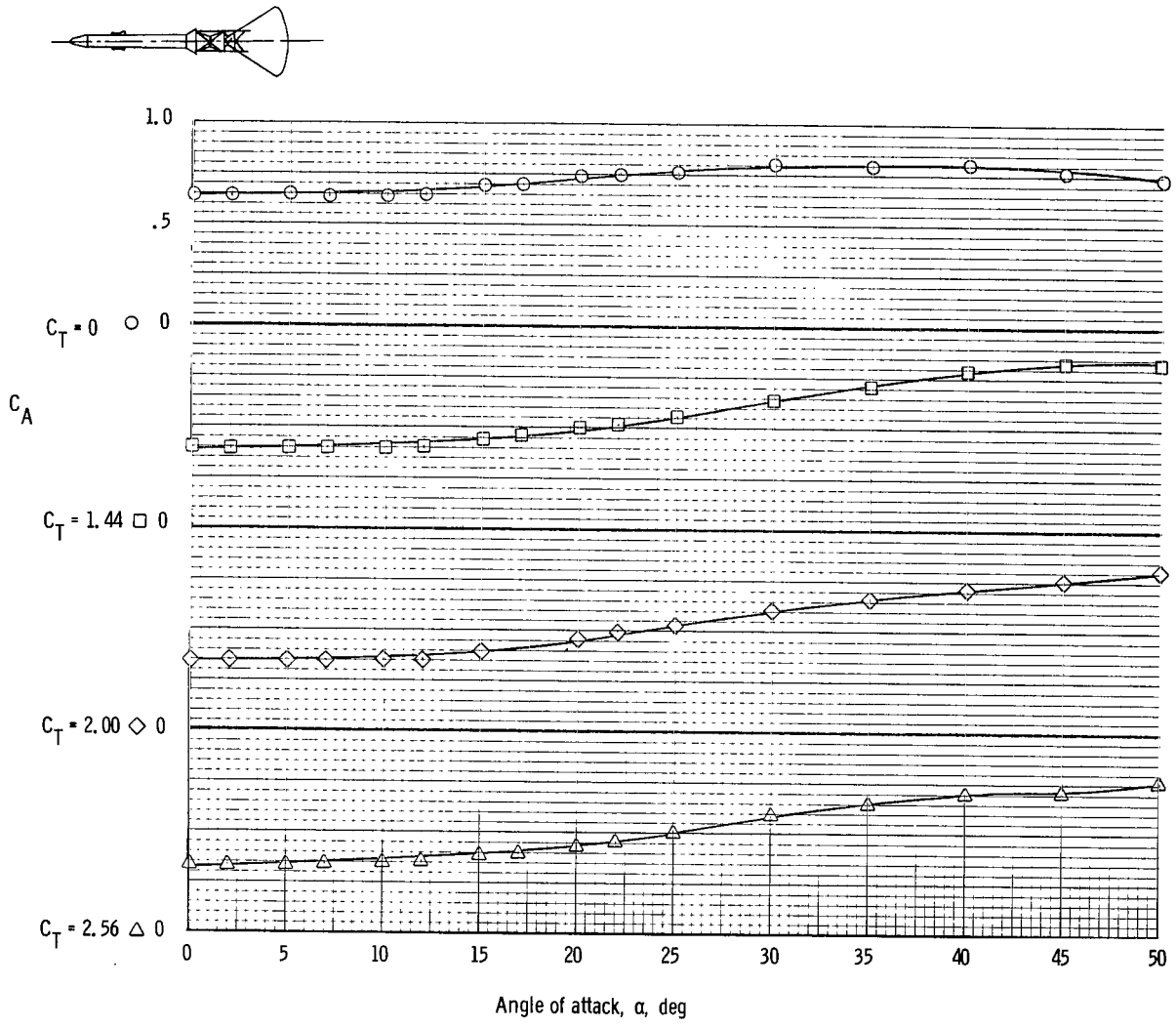

(f) Variation of axial-force coefficient with angle of attack at M = 2.99.

Figure 14. - Continued.

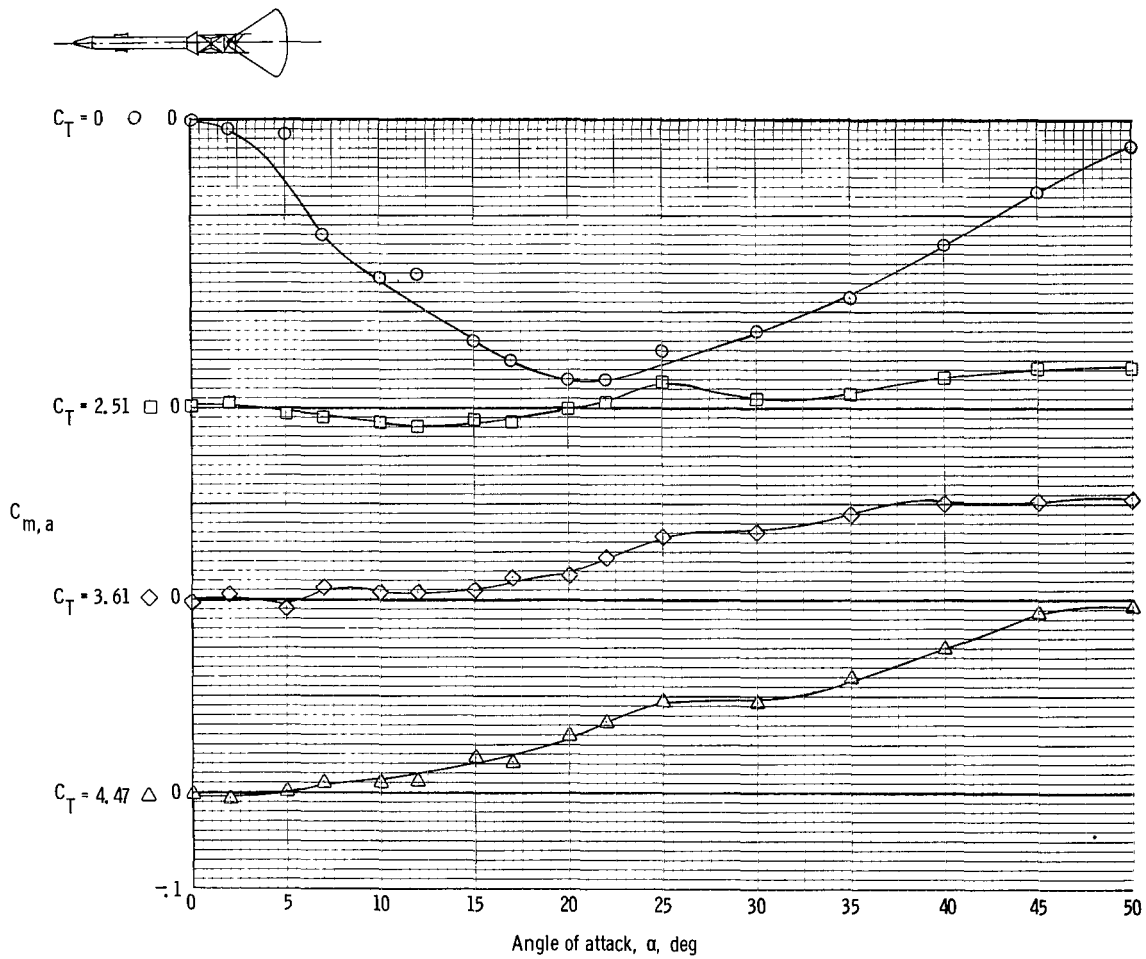

(g) Variation of pitching-moment coefficient with angle of attack at $M = 3.99$.

Figure 14. - Continued.

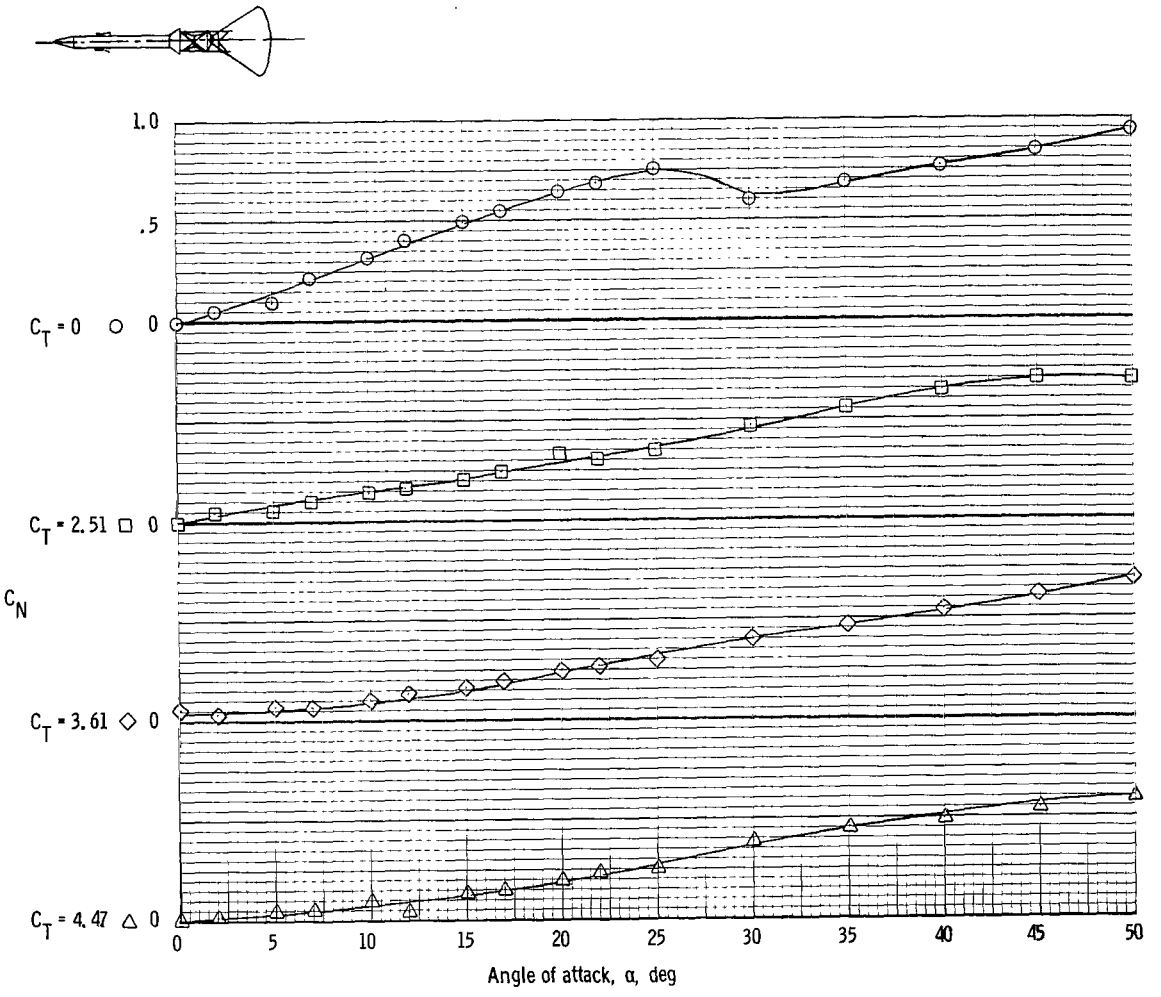

(h) Variation of normal-force coefficient with angle of attack at $M = 3.99$.

Figure 14. - Continued.

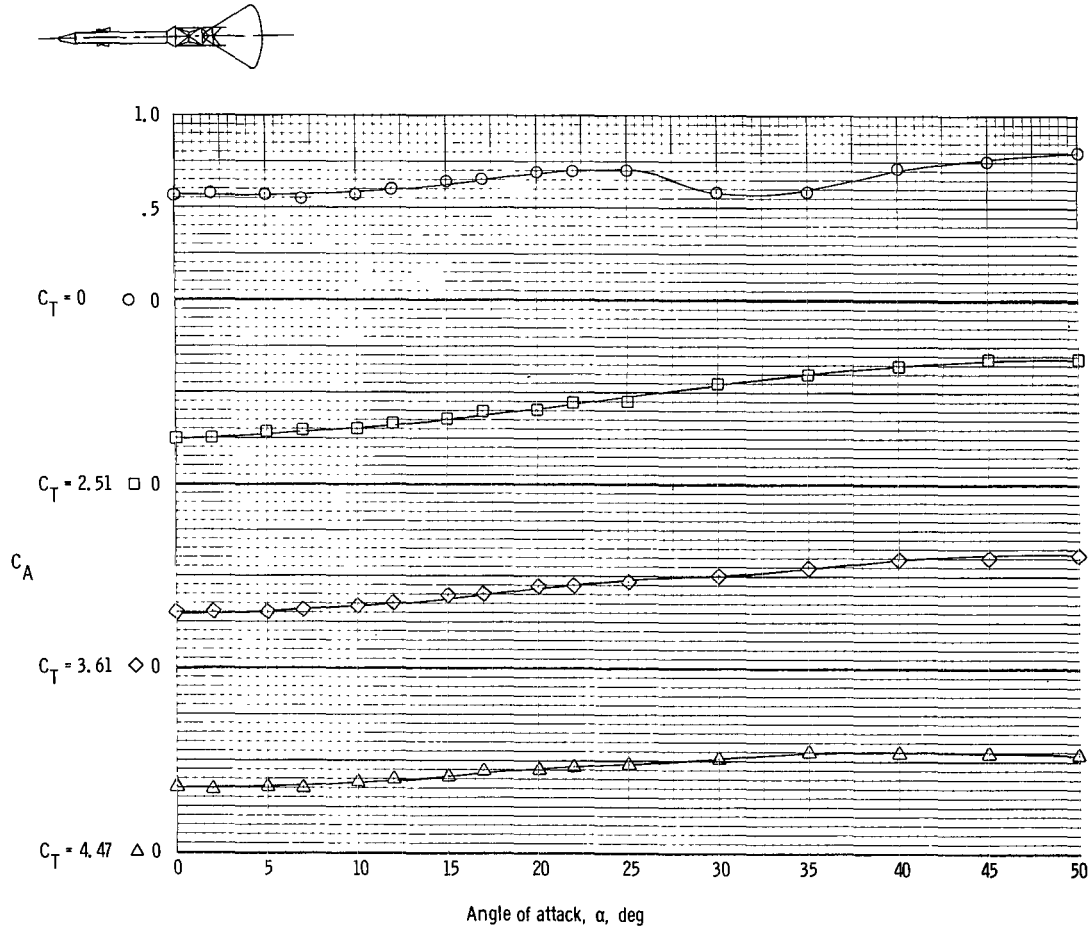

(i) Variation of axial-force coefficient with angle of attack at $M = 3.99$.

Figure 14. - Continued.

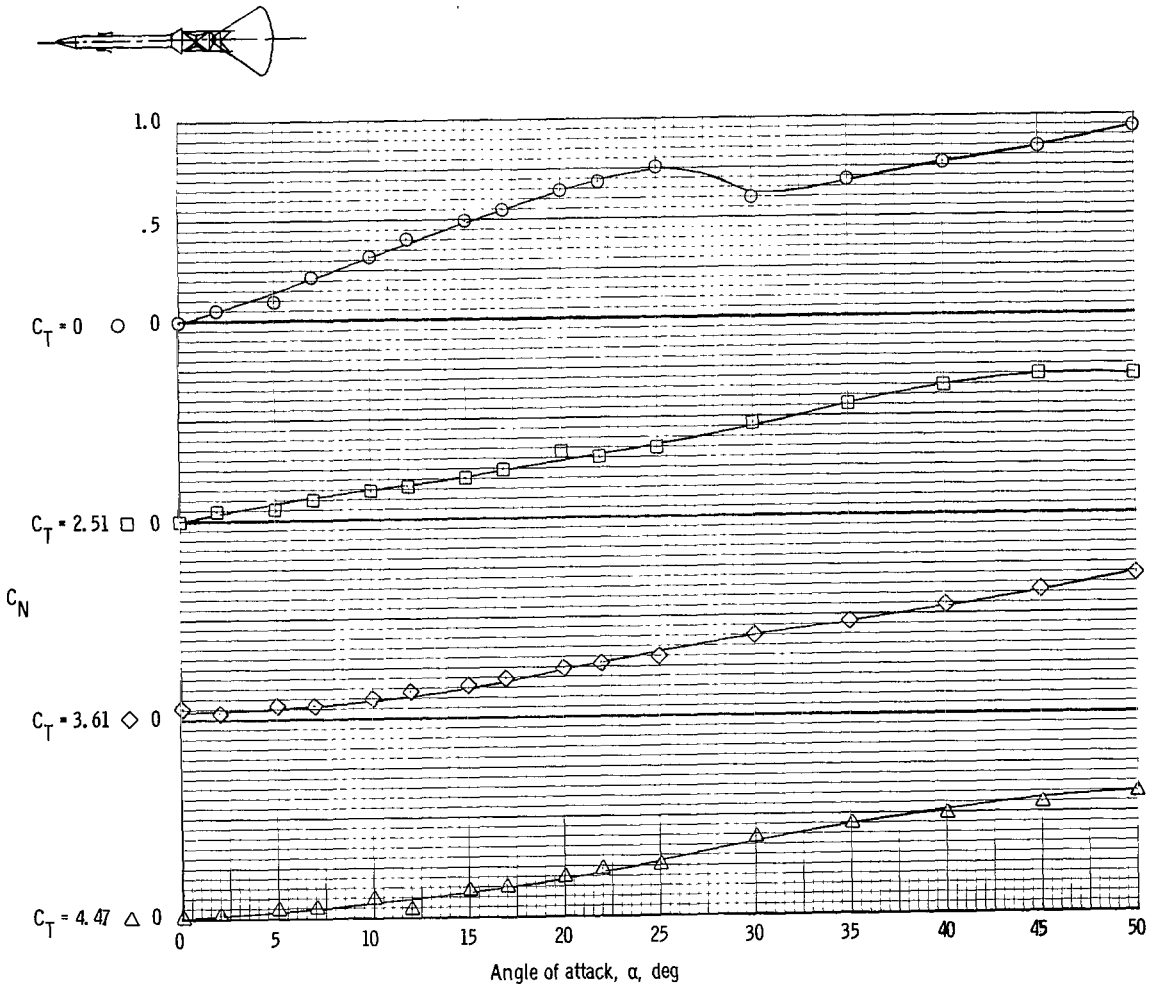

(h) Variation of normal-force coefficient with angle of attack at $M = 3.99$.

Figure 14. - Continued.

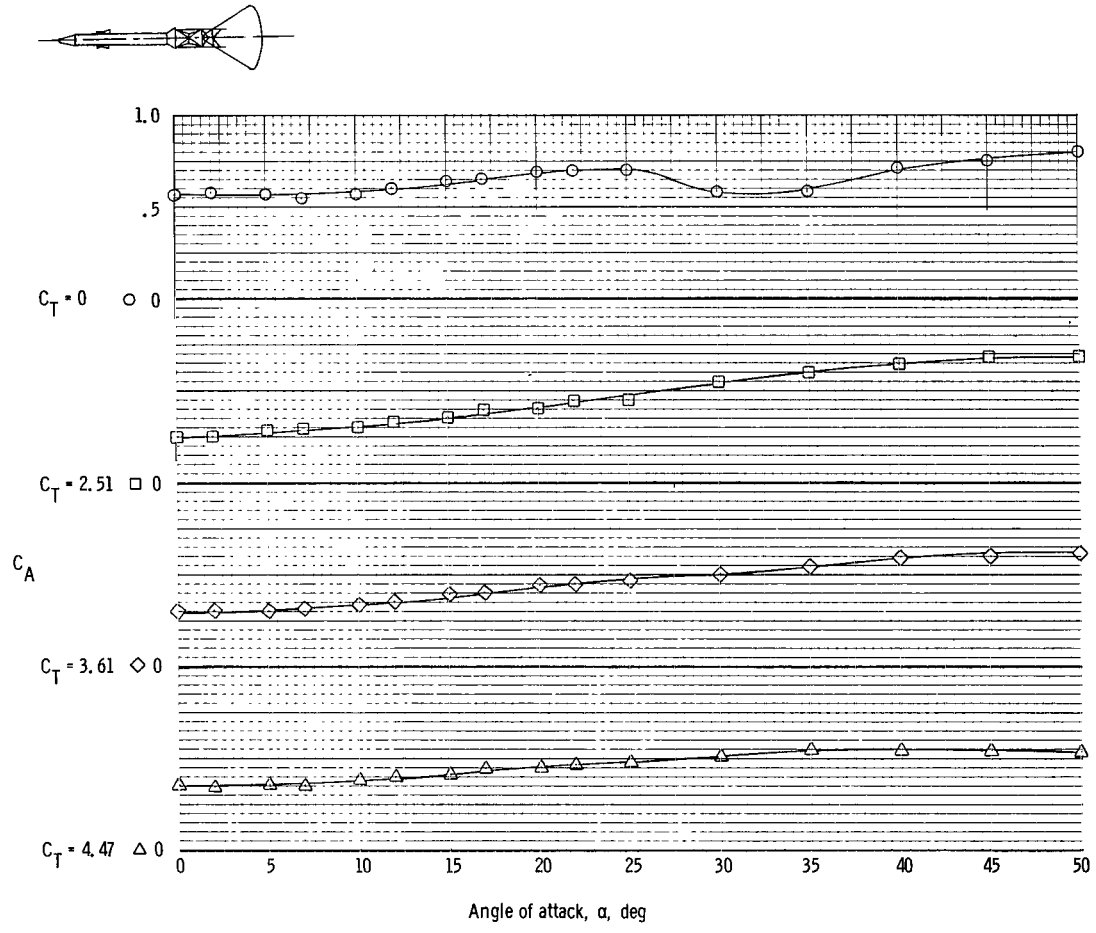

(i) Variation of axial-force coefficient with angle of attack at $M = 3.99$.

Figure 14. - Continued.

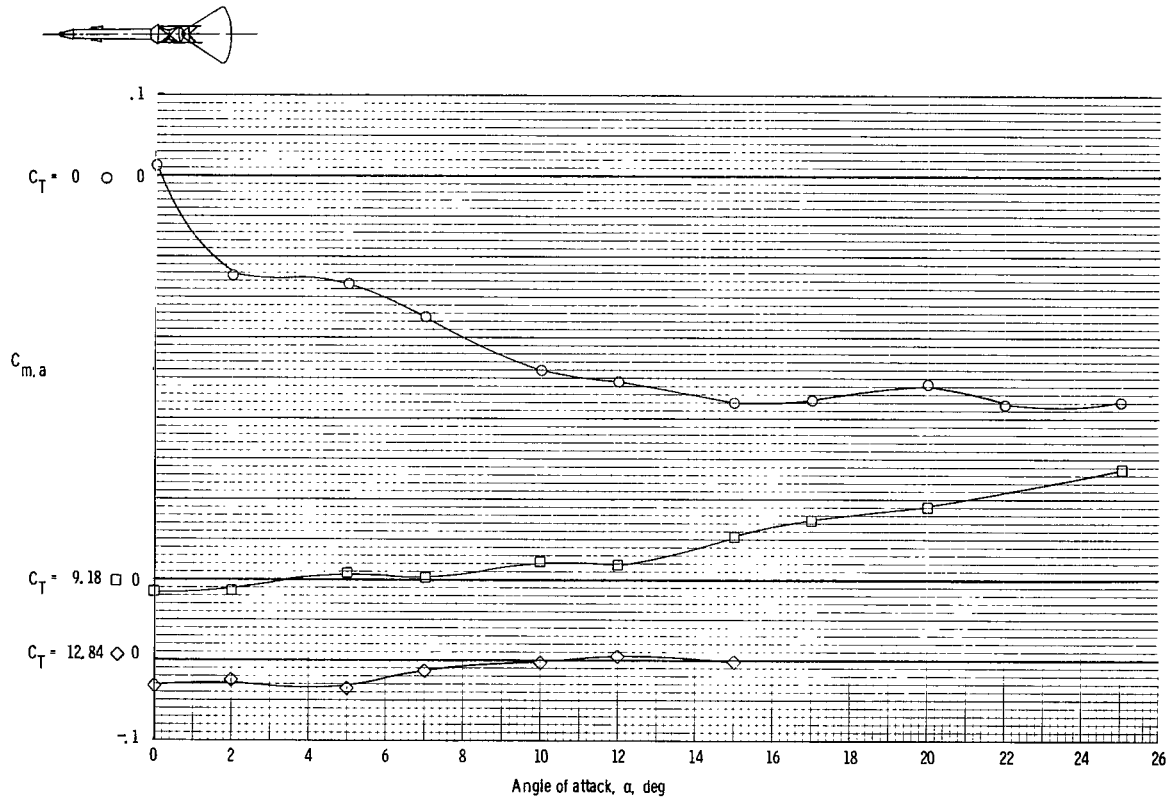

(j) Variation of pitching-moment coefficient with angle of attack at $M = 5.97$.

Figure 14. - Continued.

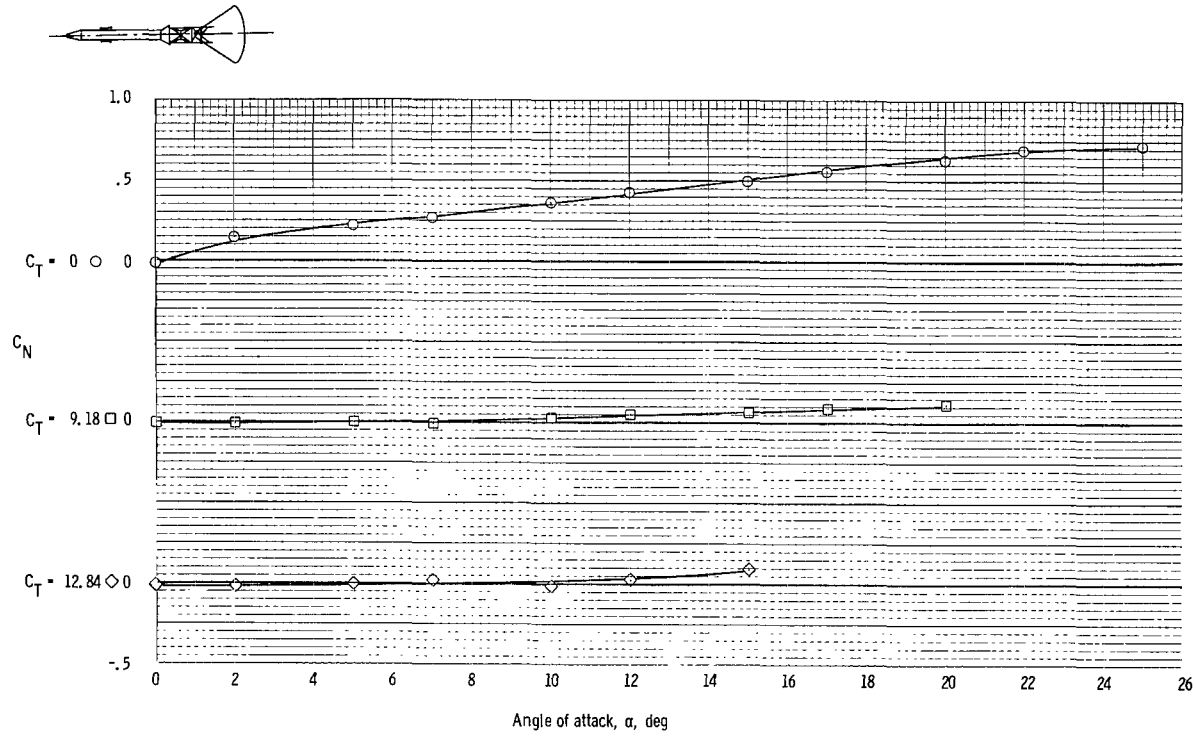

(k) Variation of normal-force coefficient with angle of attack at $M = 5.97$.

Figure 14. - Continued.

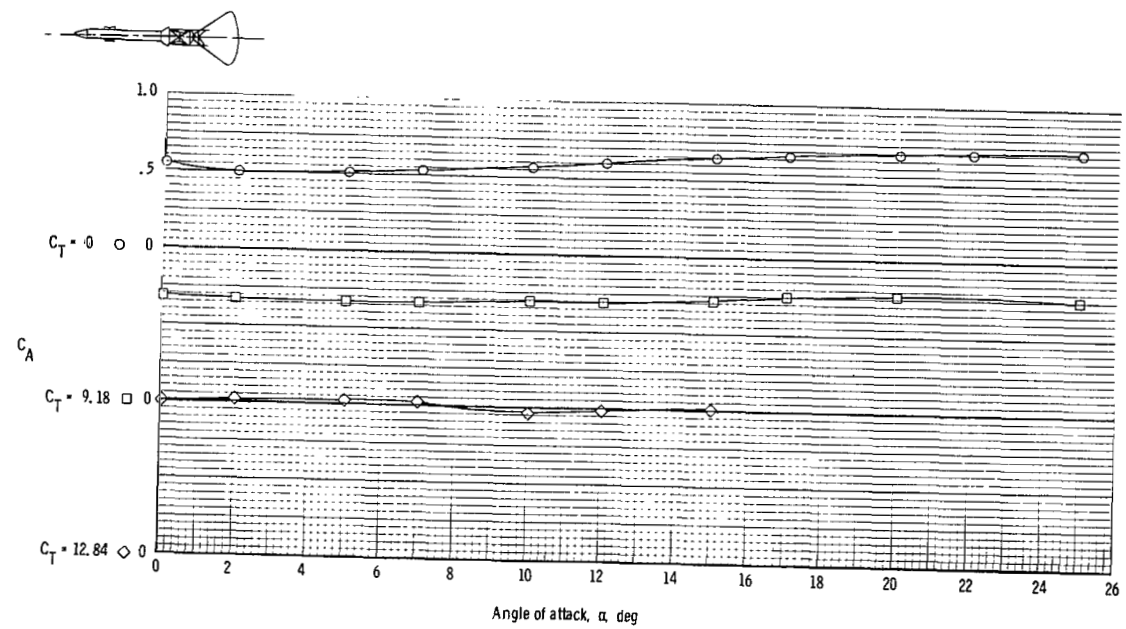

(l) Variation of axial-force coefficient with angle of attack at $M = 5.97$.

Figure 14. - Concluded.

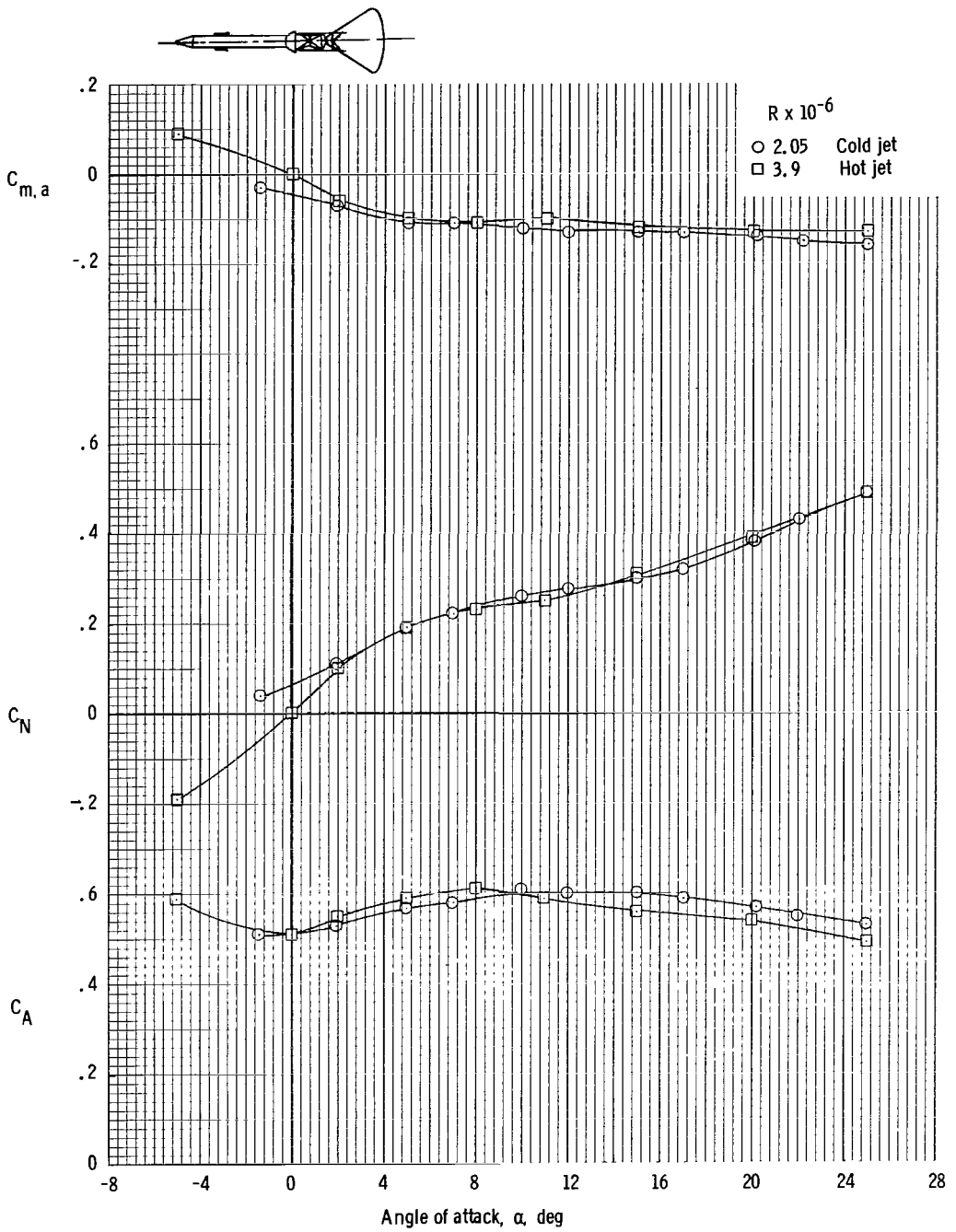

(a) Variation of pitching-moment, normal-force, and axial-force coefficients with angle of attack at $C_T = 0$.

Figure 15. - A comparison of hot-jet and cold-jet longitudinal stability characteristics of the Apollo launch escape vehicle as determined in the Langley 16-Foot Tunnel and the AEDC-A Tunnel at $M = 0.7$.

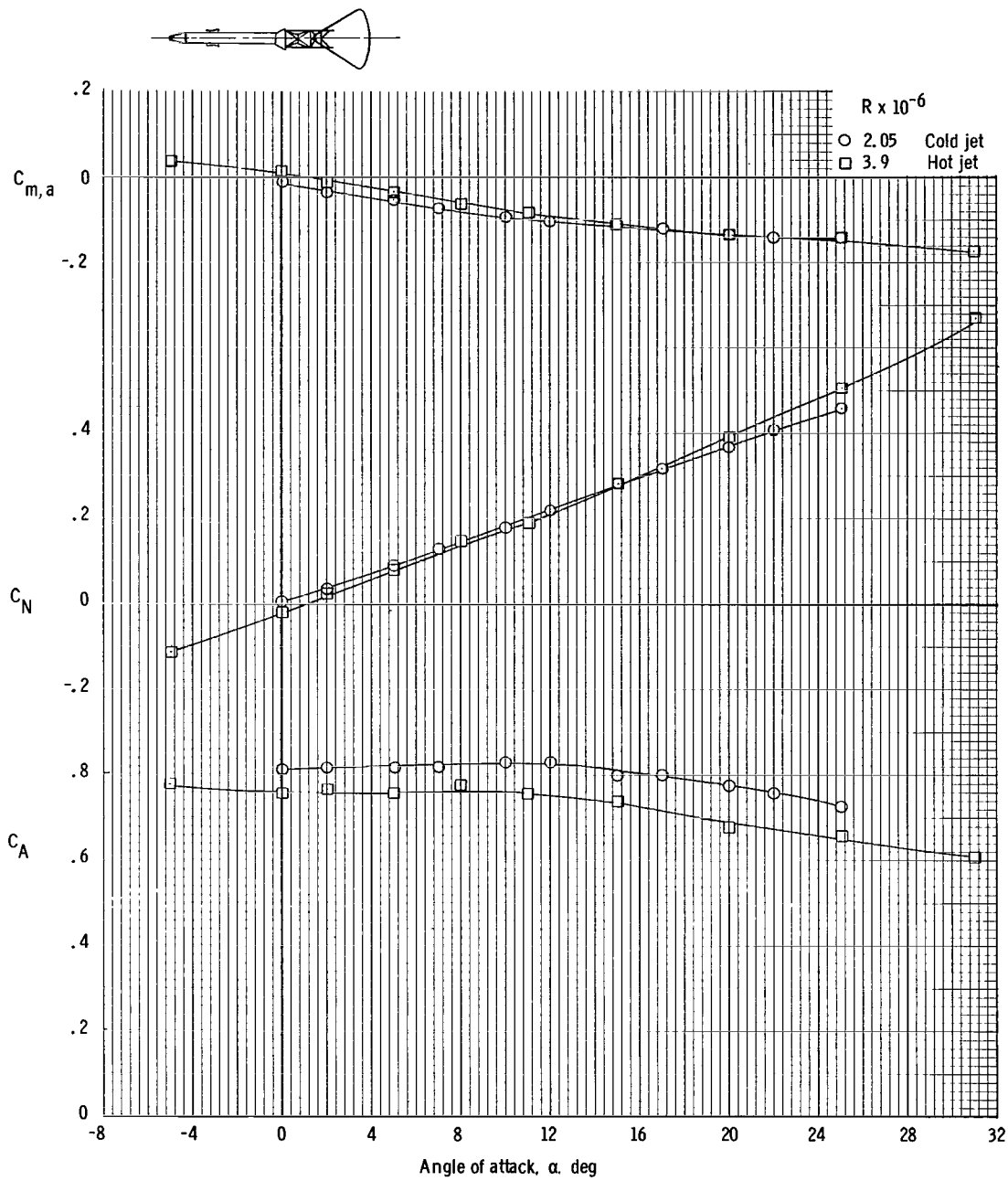

(b) Variation of pitching-moment, normal-force, and axial-force coefficients with angle of attack at $C_T = 1.34$.

Figure 15. - Continued.

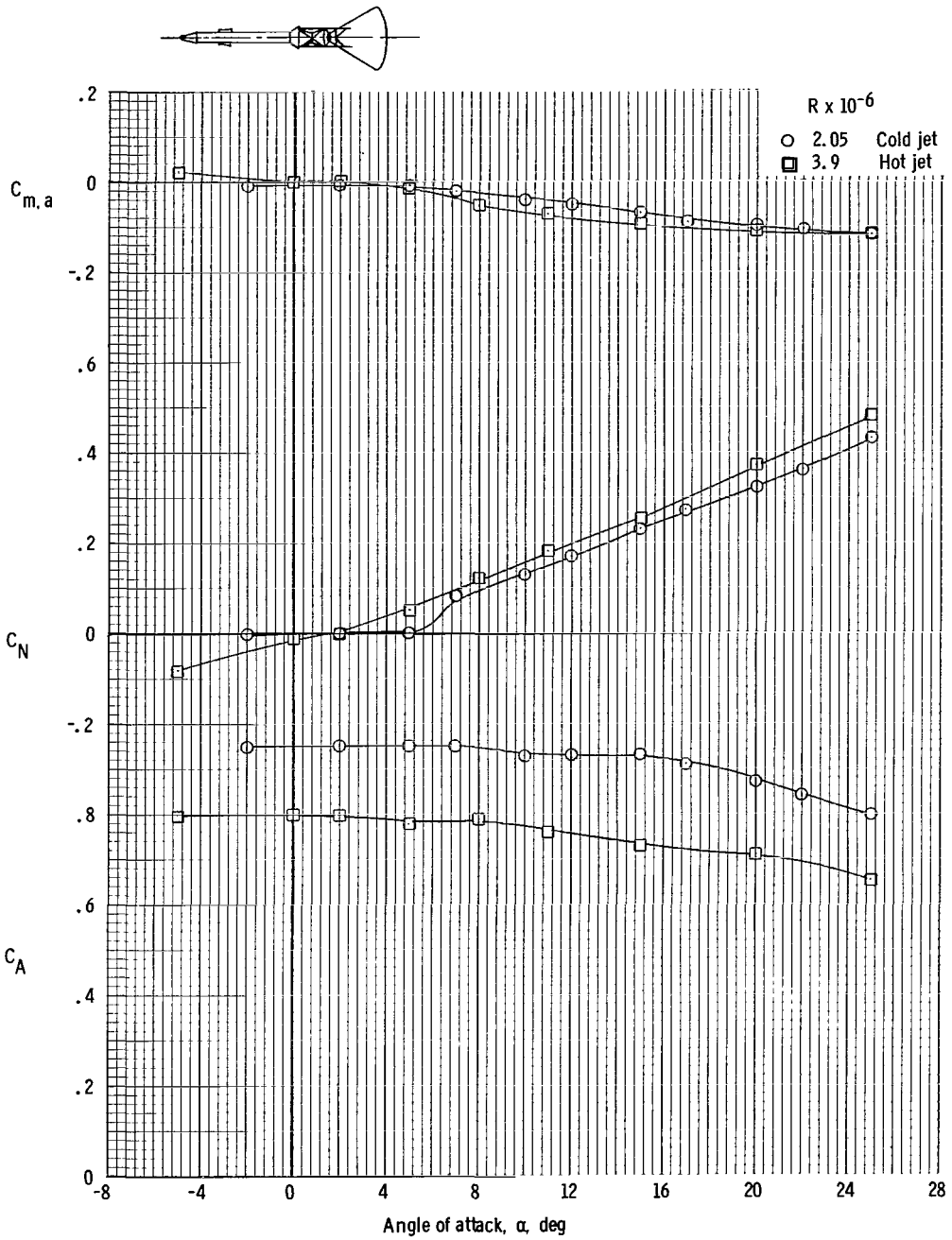

(c) Variation of pitching-moment, normal-force, and axial-force coefficients with angle of attack at $C_T = 2.4$.

Figure 15. - Concluded.

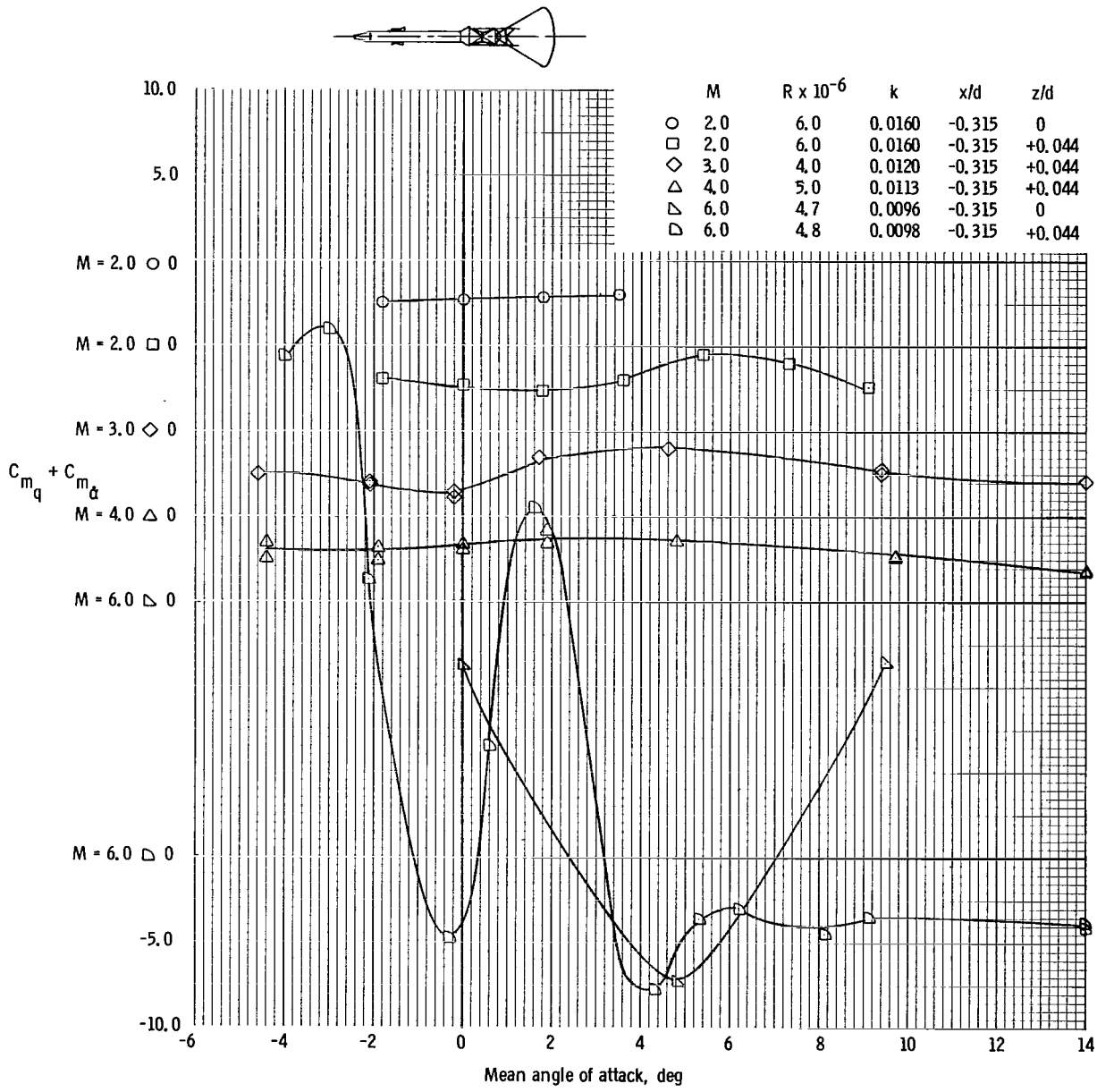

Figure 16. - Longitudinal oscillatory stability derivatives for the Apollo launch escape vehicle obtained in the AEDC-A Tunnel using the forced-oscillation technique at Mach numbers from 2.0 to 6.0.

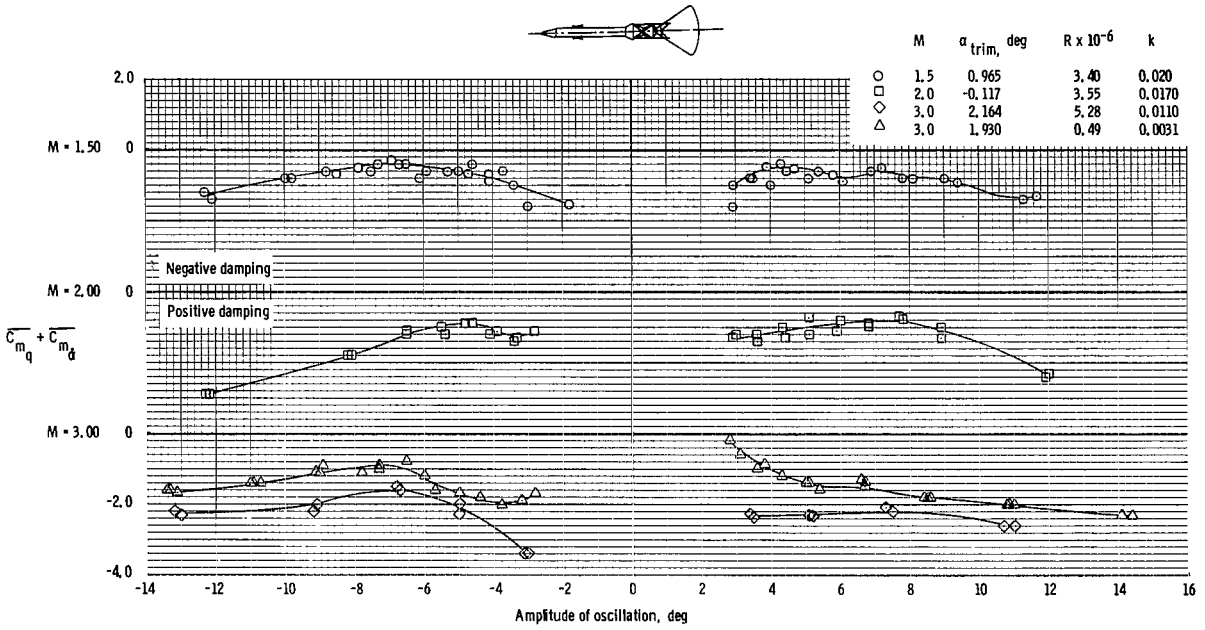

(a) Variation of damping-in-pitch parameter with amplitude of oscillation. (x/d = -0.208, z/d = 0.)

Figure 17. - Longitudinal oscillatory stability derivatives for the Apollo launch escape vehicle as determined in the AEDC-A facility at Mach numbers from 1.5 to 4.00.

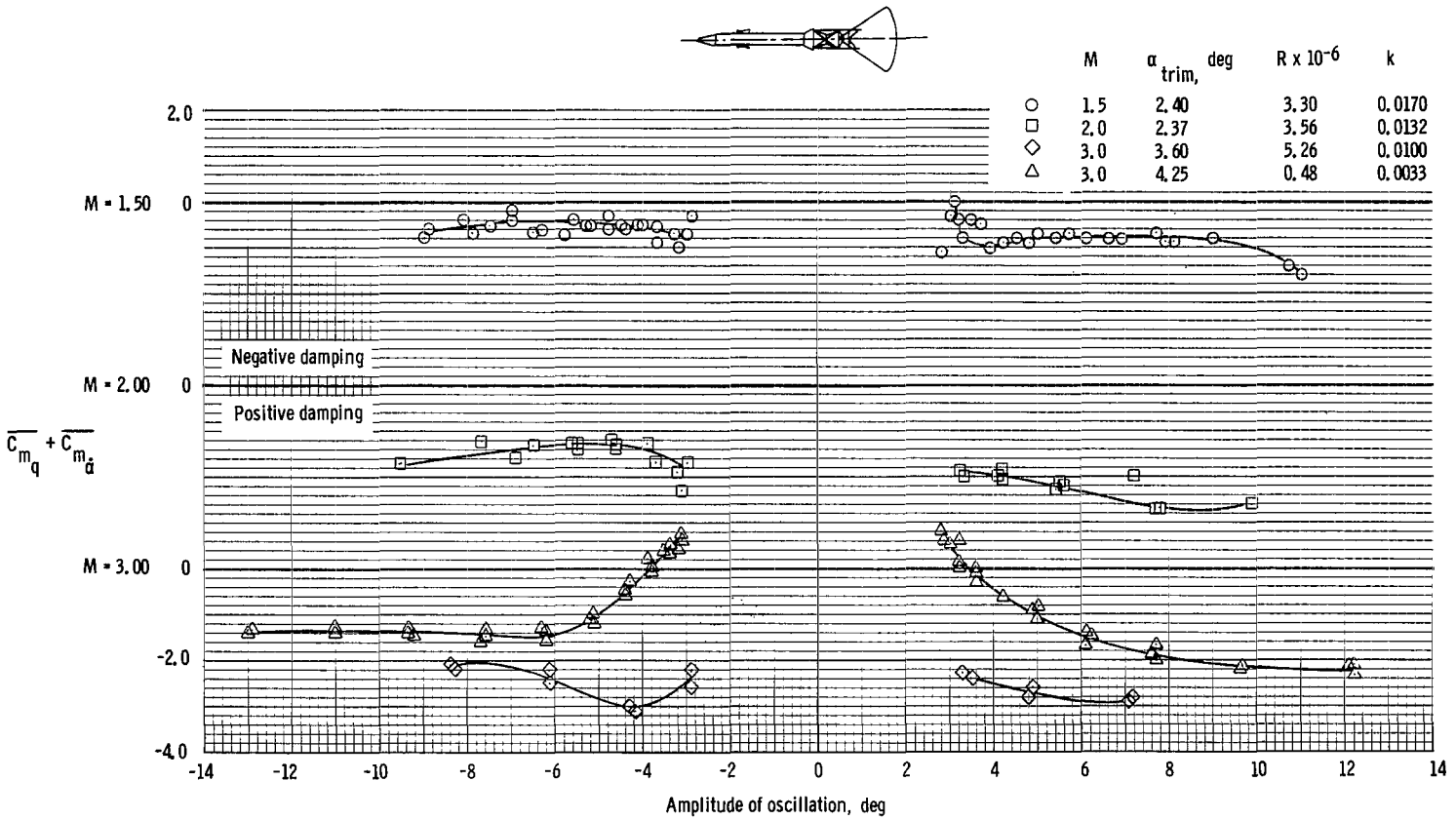

(b) Variation of damping-in-pitch parameter with amplitude of oscillation. (x/d = -0.208, z/d = 0.037.)

Figure 17. - Continued.

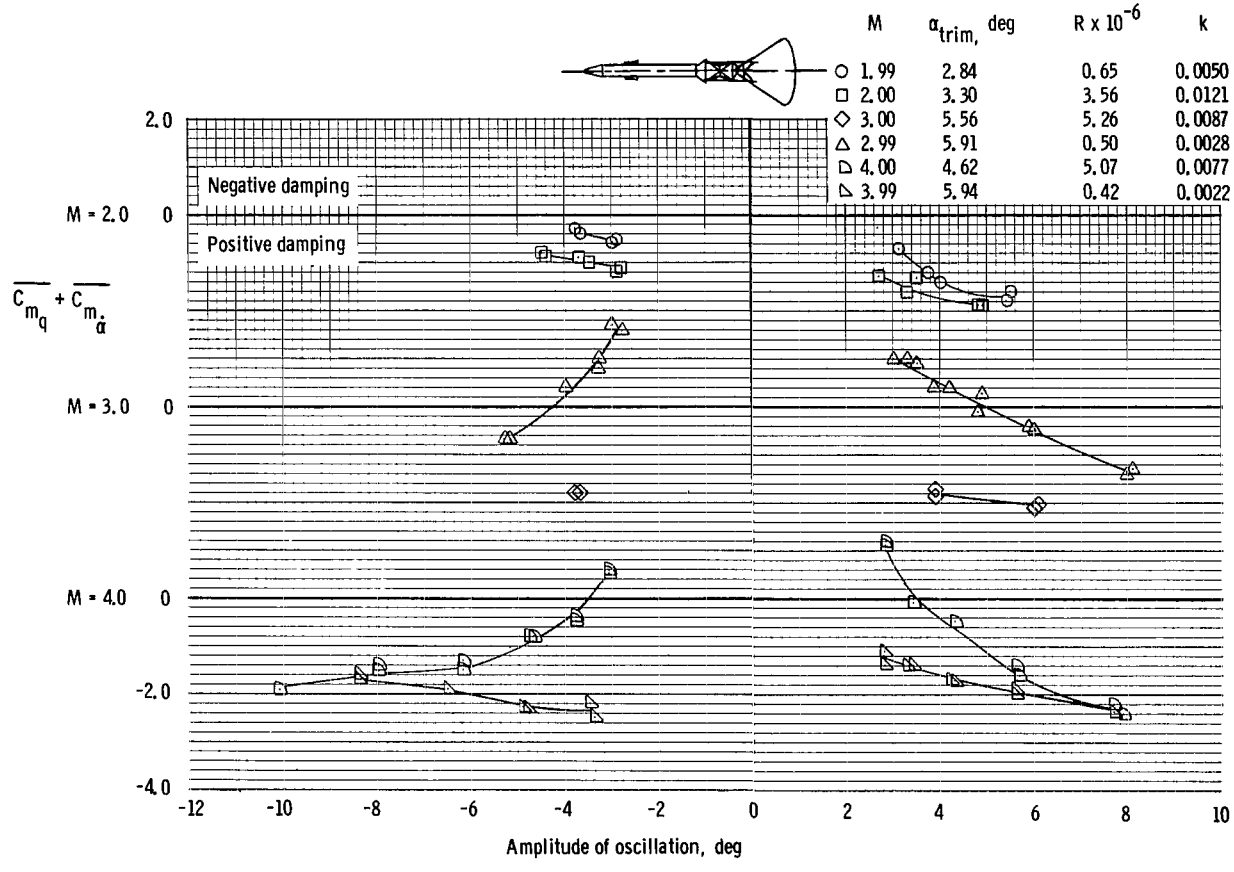

(c) Variation of damping-in-pitch parameter with amplitude of oscillation. ($x/d = -0.316$, $z/d = 0.0442$.)

Figure 17. - Concluded.

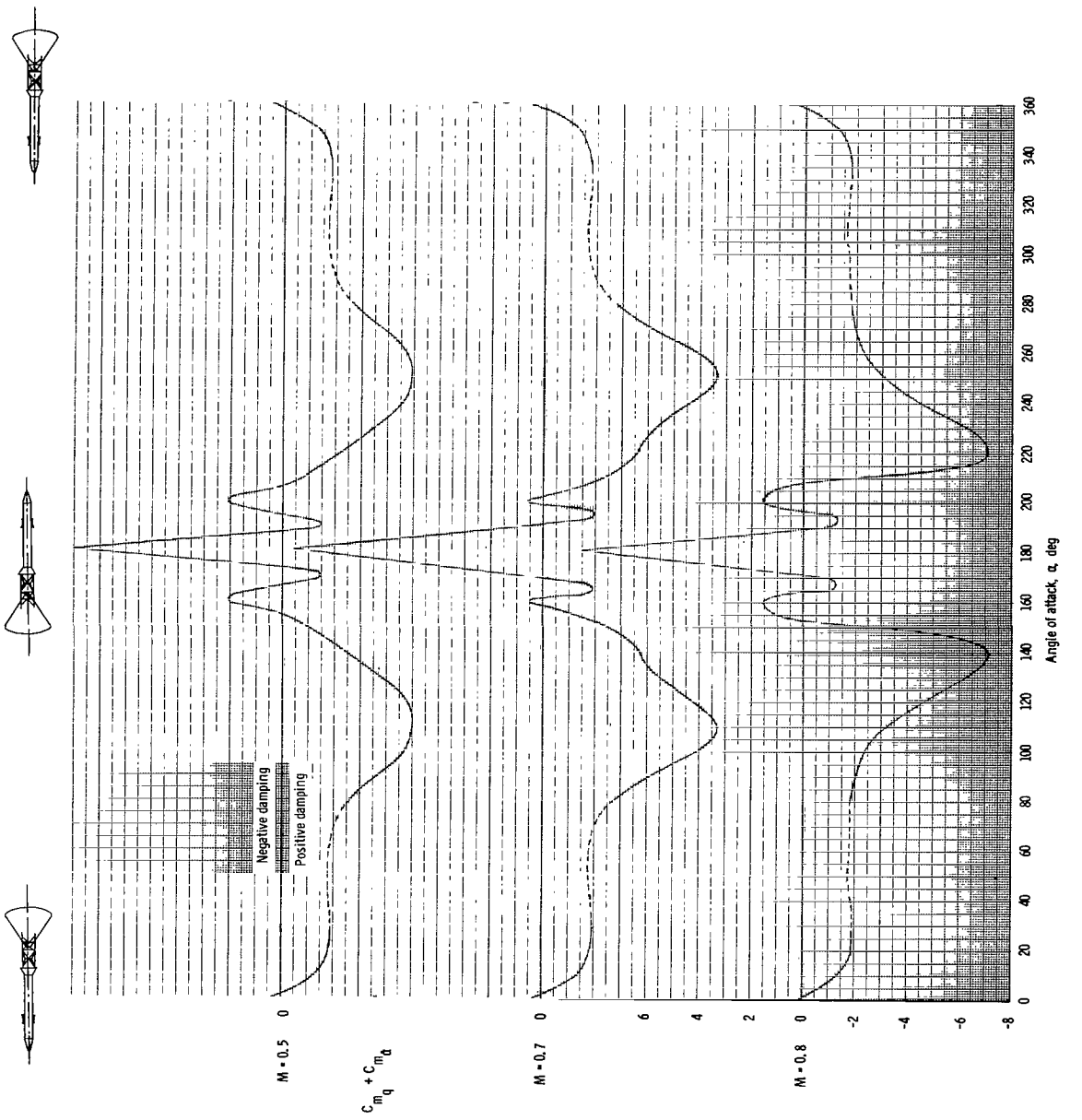

(a) Variation of damping-in-pitch parameter with angle of attack at Mach numbers 0.5, 0.7, and 0.8. $I_m = 0.251$ slug-ft^2.

Figure 18. - Dynamic longitudinal oscillatory stability derivatives for the Apollo launch escape vehicle as determined using the free-to-tumble technique in the NAA-TWT and LeRC facilities at Mach numbers from 0.5 to 1.98.

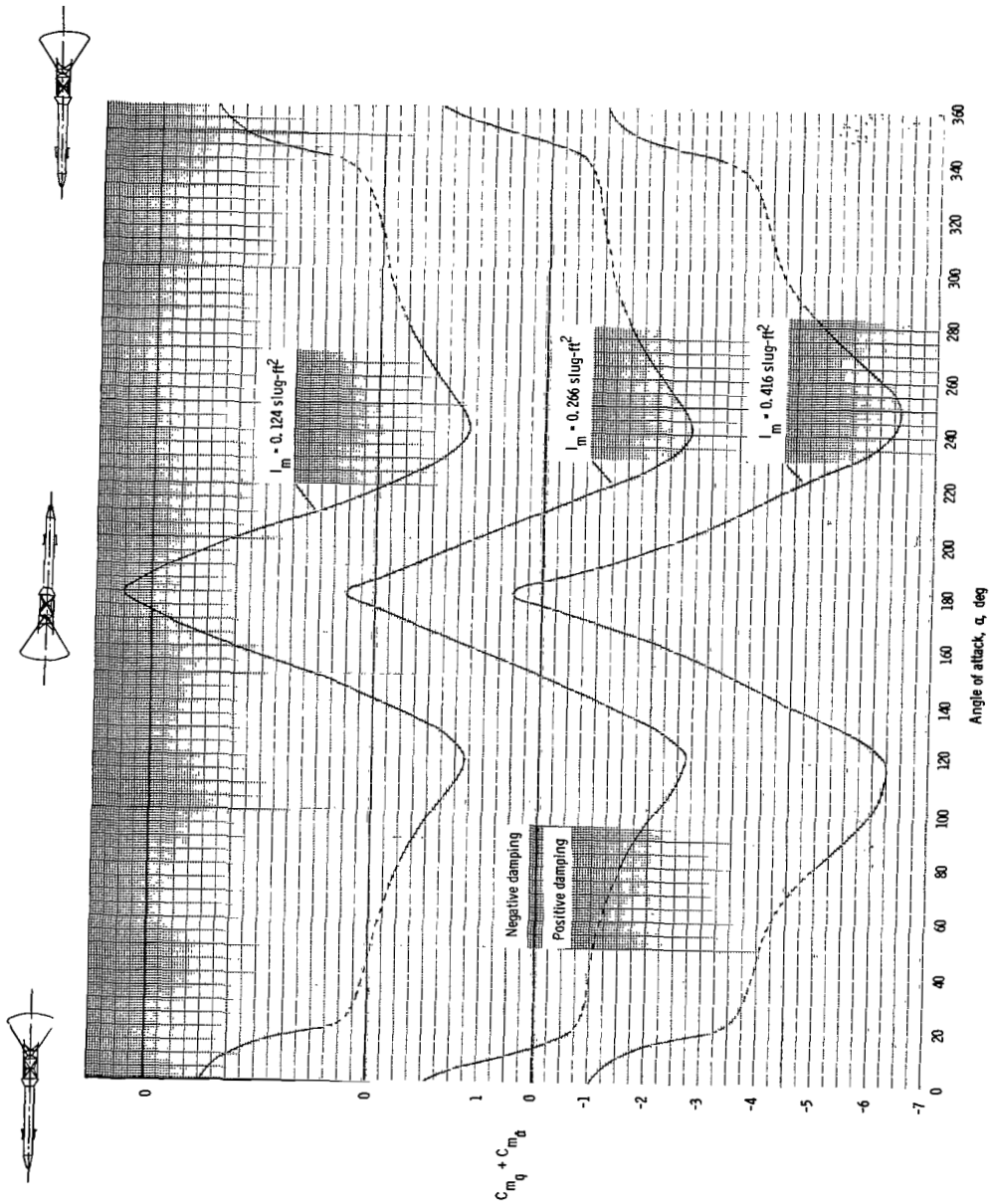

(b) Variation of damping-in-pitch parameter with angle of attack at $M = 1.59$.

Figure 18. - Continued.

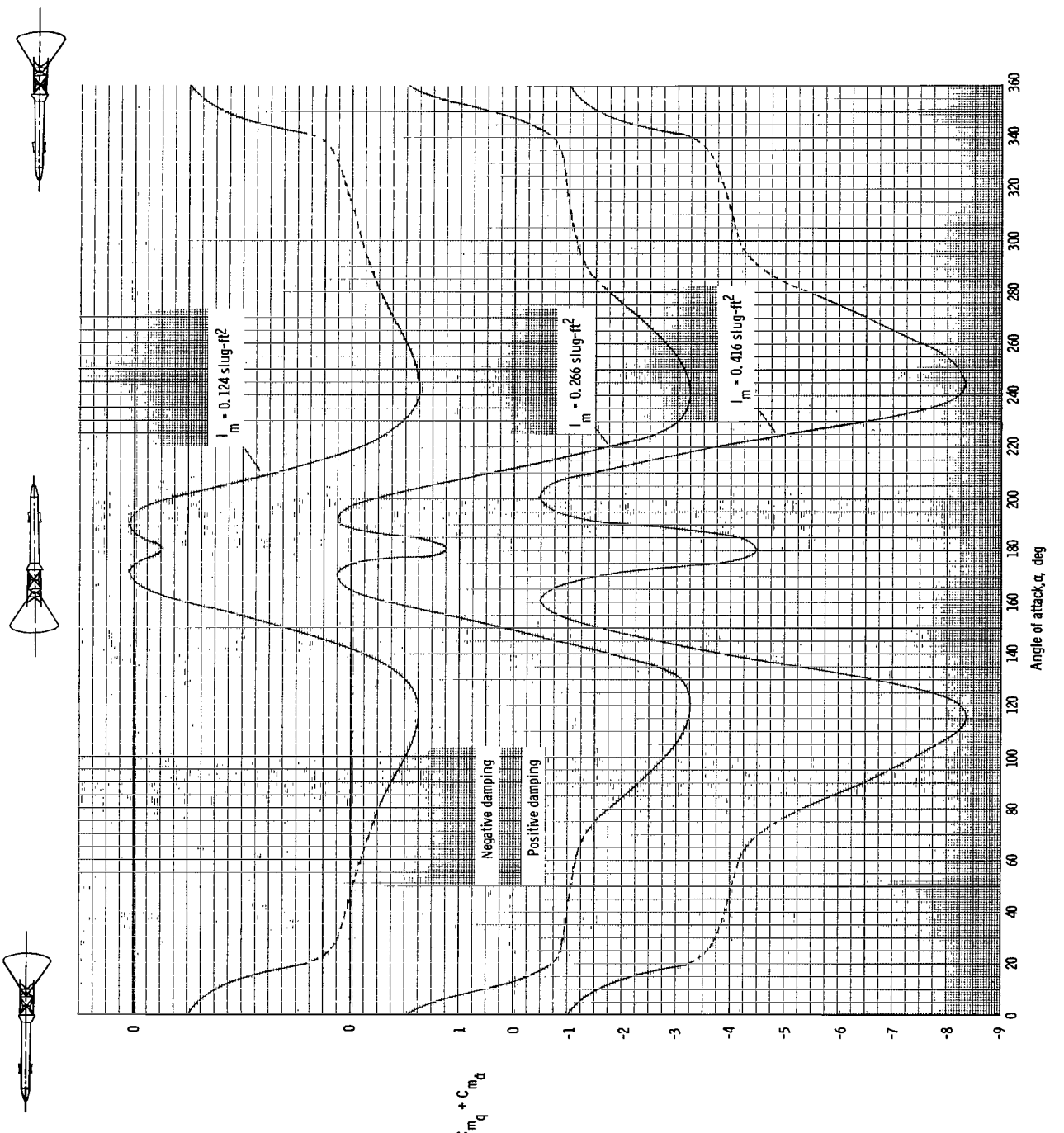

(c) Variation of damping-in-pitch parameter with angle of attack at M = 1.98.

Figure 18. - Concluded.

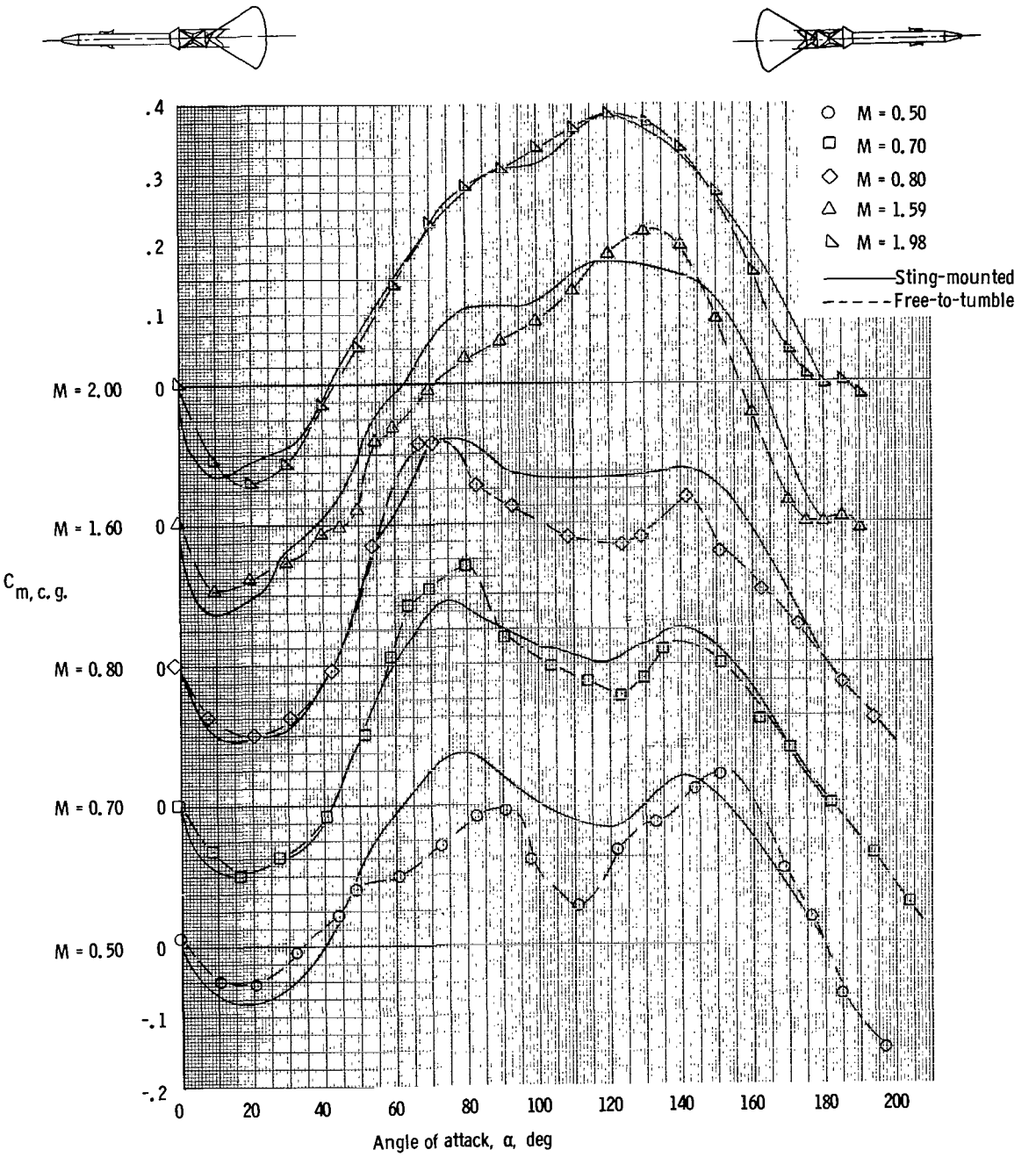

Figure 19. - Comparison of static pitching-moment coefficient data obtained with sting-mounted and transverse rod-mounted models. (x/d = -0. 104, z/d = 0.)

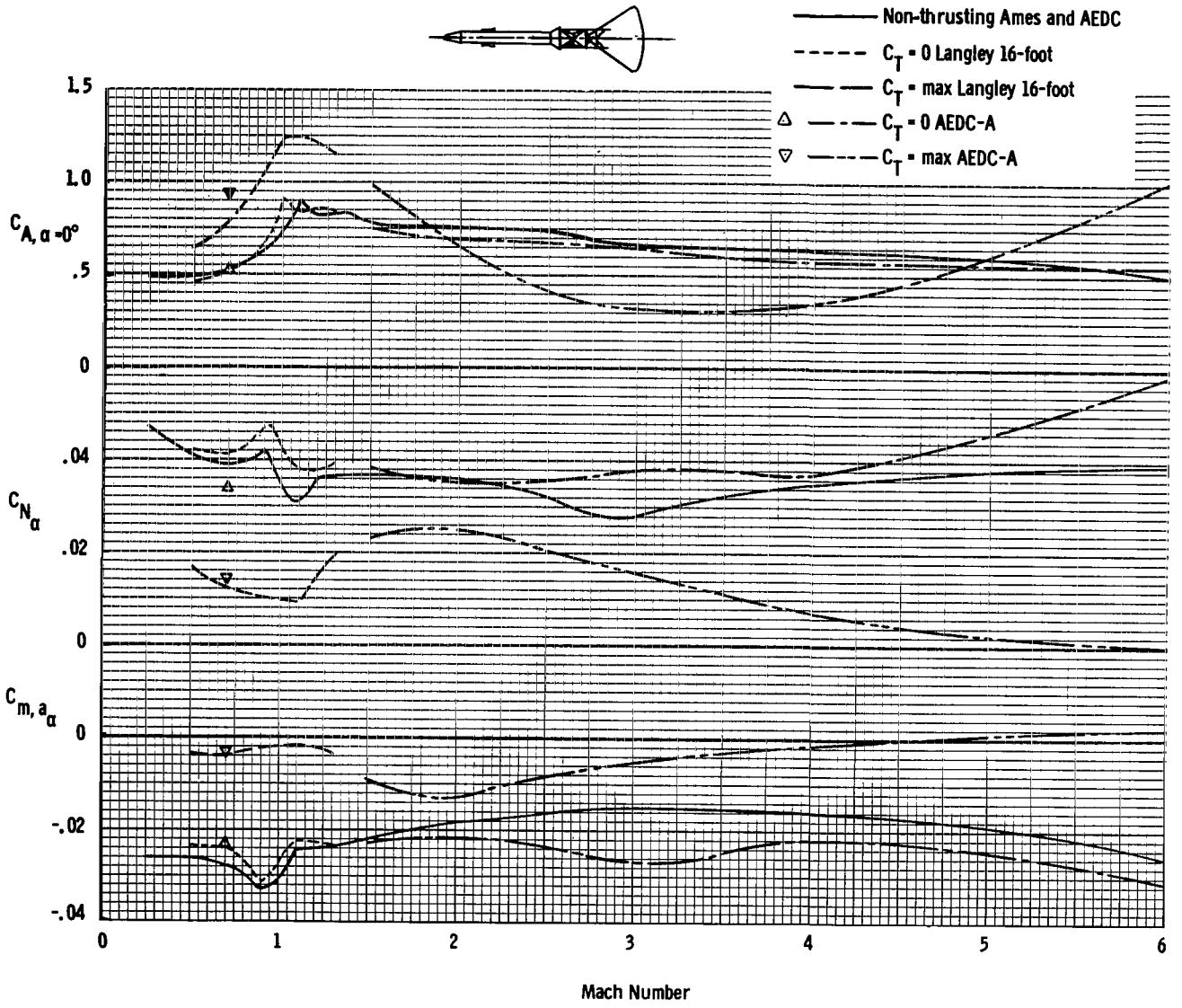

Figure 20. - Variation of summary parameters, $C_{A, \alpha=0°}$, C_{N_α}, and C_{m, a_α} with Mach number.

"The aeronautical and space activities of the United States shall be conducted so as to contribute . . . to the expansion of human knowledge of phenomena in the atmosphere and space. The Administration shall provide for the widest practicable and appropriate dissemination of information concerning its activities and the results thereof."

—NATIONAL AERONAUTICS AND SPACE ACT OF 1958

NASA SCIENTIFIC AND TECHNICAL PUBLICATIONS

TECHNICAL REPORTS: Scientific and technical information considered important, complete, and a lasting contribution to existing knowledge.

TECHNICAL NOTES: Information less broad in scope but nevertheless of importance as a contribution to existing knowledge.

TECHNICAL MEMORANDUMS: Information receiving limited distribution because of preliminary data, security classification, or other reasons.

CONTRACTOR REPORTS: Scientific and technical information generated under a NASA contract or grant and considered an important contribution to existing knowledge.

TECHNICAL TRANSLATIONS: Information published in a foreign language considered to merit NASA distribution in English.

SPECIAL PUBLICATIONS: Information derived from or of value to NASA activities. Publications include conference proceedings, monographs, data compilations, handbooks, sourcebooks, and special bibliographies.

TECHNOLOGY UTILIZATION PUBLICATIONS: Information on technology used by NASA that may be of particular interest in commercial and other non-aerospace applications. Publications include Tech Briefs, Technology Utilization Reports and Notes, and Technology Surveys.

Details on the availability of these publications may be obtained from:

SCIENTIFIC AND TECHNICAL INFORMATION DIVISION

NATIONAL AERONAUTICS AND SPACE ADMINISTRATION

Washington, D.C. 20546